Andrea Friese

Bundesanstalt für Geowissenschaften und Rohstoffe

InSAR, structural analyses and dating of Paka volcanic products, Northern Kenya Rift

Final Report

TECHNICAL COOPERATION
PROJECT NO.: 2009.2222.9

FEDERAL INSTITUTE FOR GEOSCIENCES AND NATURAL RESOURCES (BGR), HANNOVER, GERMANY

GEOTHERMAL DEVELOPMENT COMPANY, NAIROBI, KENYA

TECHNICAL COOPERATION – GEOTHERM Project

Compiled by: Andrea Friese
Federal Institute for Geosciences and Natural Resources (BGR), Hannover

Commissioned by: Federal Ministry for Economic Cooperation and Development, Germany (Bundesministerium für wirtschaftliche Zusammenarbeit und Entwicklung, BMZ)

Projekt: GEOTHERM programme – Promoting the Utilization of Geothermal Energy in Developing Countries
BGR 05-2343
BMZ PN 2009.2222.9

Date: October 2015

Table of Contents

Abbreviations

Al	Aluminum
AOI	Area of Interest
Ar	Argon
ASAR	Advanced Synthetic Aperture Radar (SAR sensor onboard Envisat-Satellite)
BGR	Federal Institute for Geosciences and Natural Resources
BGS	British Geological Survey
BMZ	Federal Ministry for Ministry Economic Cooperation and Development
Ca	Calcium
DEM	Digital Elevation Model
DLR	German Aerospace Center
DTM	Digital Terrain Model
ESA	European Space Agency
GCP	Ground Control Point
GDC	Geothermal Development Company
GPS	Global Positioning System
HCl	Hydrochloric acid
HRS	High-Resolution
HH	Horizontal Transmit – Horizontal Receive Polarisation
InSAR	Interferometric Synthetic Aperture Radar
IMS	Single Image Mode (Envisat satellite)
K	Potassium
LiDAR	Light Detection And Ranging
MS	Multispectral
OSTR	Oregon State TRIGA Reactor
PSI	Persistent Scatter Interferometry
QC	Quality Control
RGB	Red Green Blue
RMSE	Root Mean Square Error
SAR	Synthetic Aperture Radar
SB	Small Baseline
SBAS	Small Baseline Subset
SRTM	Shuttle Radar Topography Mission
SM	StripMap (Standard Image Acquisition Mode for TerraSAR-X)
UCLA	University of California, Los Angeles
VV	Vertical Transmit – Vertical Receive Polarisation

Attachments – Digital and/or analog

Attachment 1: Surface Deformation Map based on Envisat data

Attachment 2: Surface Deformation Map based on TerraSAR-X data

Attachment 3: ESRI-Shapefile of Envisat study (only digital)

Attachment 4: ESRI-Shapefile of TerraSAR-X study (only digital)

Attachment 5: Description of columns of digital ESRI-Shapefiles

Attachment 6: Digital Terrain Model in GeoTIFF format (only digital)

Attachment 7: Digital Terrain Model in ASCII format (only digital)

Attachment 8: Ortho-Images Tiles in GeoTIFF format (only digital)

Attachment 9: Age spectra, normal isochron and inverse isochron plots of $^{40}Ar/^{39}Ar$ analysis

Attachment 10: $^{40}Ar/^{39}Ar$ analytical results of Paka volcanics

Attachment 11: Age dating results superimposed on the geological map of BGS

Attachment 12: Age dating results superimposed on the shaded relief map created from DTM of Pléiades satellite data

Attachment 13: Lecture material of field training 1 (only digital)

Attachment 14: Lecture material of field training 2 (only digital)

Executive Summary

The German Federal Institute for Geosciences and Natural Resources (BGR) and the Geothermal Development Company (GDC) of Kenya collaborate on the project “InSAR, structural analyses and dating of Paka volcanic products, Northern Kenya Rift” since 2013. The project is part of the “GEOTHERM Programme – Promoting the Use of Geothermal Energy” initiated and financed by the German Federal Ministry for Economic Cooperation and Development (BMZ).

Main objective of the project is the detection of surface deformations related to Paka volcano´s activities. The eruptive history of the volcanic sequences is analysed and a structural analysis is carried out. The objectives are realised by performing an InSAR baseline study for the years 2006 to 2010 using Envisat-ASAR data, an InSAR study for the period between March and October 2013 using TerraSAR-X data, the generation of a high-resolution digital terrain model (DTM) using Pléiades data and an age dating of different lava flows using the $^{40}Ar/^{39}Ar$ method. An overview of all satellite sensors used within the project is shown in table 1.

InSAR (Interferometric Synthetic Aperture Radar) is a very powerful method to detect small surface deformations. For the time span between March 2006 and September 2010 Envisat-ASAR data are used for the study. The dataset covers an area of about 100 km x 100 km. 11 scenes are processed using the SBAS method. An uplift on the eastern flank of Paka volcano tends to behave non-linear during the investigation period. An annual movement rate of up to approximately 35 mm/year is visible until 2008 when the uplift seems to end. From 2009 until September 2010, the area shows no deformation.

The InSAR study using TerraSAR-X data for the period between March and October 2013 covers an area of about 30 km x 50 km. 17 TerraSAR-X scenes are acquired and processed using SBAS method. Analysing the TerraSAR-X data a non-linear surface deformation can be stated on the eastern flank of Paka volcano. The existing dataset shows a subsidence of ~20 mm between March and July 2013, followed by a short phase of stability turning into uplift at the end of the investigation period.

In February/March 2014, a field campaign to sample 32 different lava flows and pyroclastic deposits related to Paka volcano took place in collaboration with GDC for $^{40}Ar/^{39}Ar$ age dating. The dating yields ages between ~0.6 and 0.012 Ma for the different samples. Three phases of pronounced volcanic activity are recognised: (1) between 0.428 and 0.372 Ma, (2) between 0.160 and 0.126 Ma, and (3) between 0.039 and 0.012 Ma.

Furthermore, a high-resolution DTM for an area of ~420 km² covering all Paka related lava flows was generated using Pleiades satellite data. The DTM has a horizontal resolution of 4 m and is an ideal base for a structural analysis. Such a high-resolution DTM can also be used for infrastructural planning of roads, water pipelines or supporting buildings. The DTM was furthermore used for the two field trainings conducted in the framework of this project.

Table 1: Sensors used for the different tasks within the project.

Task	Satellite
InSAR study for period between 2006 and 2010	Envisat
InSAR study for 6 month period in 2013	TerraSAR-X
DTM	Pléiades

1 Introduction and Objectives of Project

In 2013, the German Federal Institute for Geosciences and Natural Resources (BGR) and the Kenyan Geothermal Development Company (GDC) started a new project in Kenya. The project is part of the “GEOTHERM programme – Promoting the Utilization of Geothermal Energy in Developing Countries”, initiated and financed by the German Federal Ministry for Economic Cooperation and Development (BMZ). The goals of this project are based on the Implementation Agreement “InSAR, structural analyses and dating of Paka volcanic products, Northern Kenya Rift” signed in June 2013. It supports the state-owned Kenyan Geothermal Development Company in the exploration of geothermal energy resources in the northern part of Kenya´s Rift Valley.

According to the Implementation Agreement, the following indicators of achievement should be complied:

- Geological knowledge of Paka volcanic area is improved
- Results of InSAR studies, structural analysis and age dating are summarised in a final report
- Two persons from GDC are trained in fundamentals of geological structural analyses
- GDC is enabled to interpret InSAR-data and to carry out structural analyses on its own

GDC and BGR agreed upon joint contributions to implement this project successfully.

BGR´s contributions to the project are:

- Training in Kenya and Germany depending on needs and resources
- Processed and interpreted InSAR data as mentioned in the proposal
- Structural analyses and relative ages of Paka volcanic rocks based on mid-resolution satellite images (e.g. Landsat, DTM, etc.)
- DEM processing costs will be covered by BGR if the total project allows it
- BGR staff for ground truth and field work, costs for international travels, training in Kenya and/or in Germany
- Sampling, geochemical analyses and dating of Paka volcanic rocks
- Experts in remote sensing geology
- Training in structural geology

GDC´s contributions to the project are:

- Topographic/geological maps to support survey planning and field work as well as available reports and preliminary results of geoscientific work available for the region
- Workspace for the BGR-Team for the times of missions to Kenya
- GDC will offer logistical support, provision of required transportation of GDC and BGR staff and equipment in Kenya including field surveys and customs clearance of samples (Hire of Helicopter for two days and field vehicle for 30 days at approximate costs of Ksh. 3,500,000.00)

2 Evolution of Paka volcano

Paka volcano is located within the northern Kenya Rift (Figure 1), a part of the East African Rift System that extends from southern Mozambique through Tanzania, Kenya and Ethiopia towards the Afar triple junction where it joins the Red Sea and Gulf of Aden rifts. A detailed geological overview about the evolution of Paka volcano is described by Dunkley et al. (1993) and is briefly summarised in the following. As the age dating does not confirm the here described evolution of Paka volcano the eruption history will be discussed together with the results of the age dating in chapter 5.

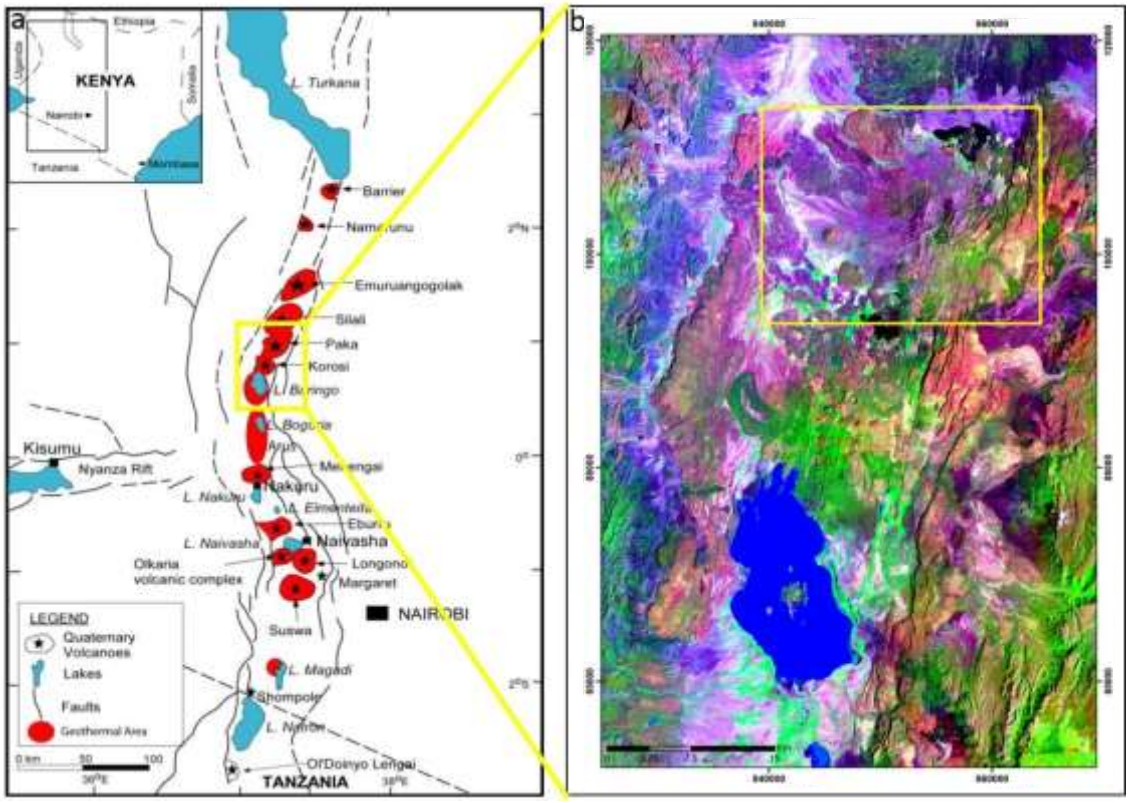

Figure 1: a) Map displaying the Kenyan Rift Valley; highlighted in yellow is the area of Paka volcano and Lake Baringo (Omenda, 2010); b) Paka volcano (highlighted in yellow) on a Landsat TM image, acquired on 30/01/2010 (bands 7,4,1 RGB).

The inner trough of the northern Kenyan Rift between Lake Baringo and Lake Turkana subsided at the end of the Pliocene. A further phase of subsidence occurred around 0.5 Ma ago in the southern area of the northern Rift were subsequently Ol Kokwe, Korosi, Paka and Silali volcanoes were formed.

Paka is a small shield volcano situated ~25 km north of Lake Baringo. It reaches a maximum altitude of ~1700 m above sea level and raises about 600 to 700 m above the rift floor. Paka volcano is dominated by a caldera with a diameter of 1.5 km. Its volcanic rocks cover an area of ~280 km² and are composed of trachytic and basaltic lava flows and pyroclastic deposits (Figure 2).

The *Mugearites* and the *Lower Trachytes* (including the *Secumius Trachyte* as part of the Lower Trachyte) are the oldest exposed rocks at Paka volcano that formed an early volcanic shield. The following NNE-trending fracturing of this early shield was accompanied by the eruption of the *Lower Basalts* that erupted from fissures mainly on the eastern flank of Paka volcano. Subsequent the *Upper Trachytes* erupted from domes and cones along N- and NNE-

trending fissures in the upper part of the volcano and formed discoid shaped lava flows around the flanks of Paka volcano. An axial rift zone, defined by the Eastern and Western Boundary faults, developed due to further faulting and fracturing across the volcano shield. This development was most likely contemporaneous with the eruption of the *Upper Basalt* on the lower northern and southern flanks of Paka volcano.

At ~10.000 years ago, trachytic *pyroclastic flows* were deposited on the upper northern flanks and the summit area. Here they formed a NW-trending ridge across the summit area. Topographically constrained by the Northern Kenya rift zone, pyroclastic flows and mudflows from the summit area flowed down the northern flanks. Locally, they also flowed through breaches in the Western Boundary fault scarp to cover the western flanks. Pumice deposits and tuffs finally resulted in the collapse of the summit area and formed a series of craters and calderas that are aligned on a north-west trend.

The final stage after the caldera formation at Paka volcano was the eruption of trachyte lava within the caldera and the following eruption of mugearitic scoria and lava. Furthermore, *Young Basalts* and hawaiite lavas have been erupted from fissures on the northern and southern flanks.

Paka volcanoes structure is dominated by a 7.5 km wide zone of normal faulting that shows a right stepping en échelon arrangement across the volcano. This correlates with the regional fault pattern that is also recognizable at Korosi and Chepchuk in the south and Silali volcano in the north. The faults on the southern flanks of Paka trend N-S. However, the direction changes into a NNE to NE trend as they converge the summit area. This direction change across Paka and the general absence of faulting in the summit area suggests that probably a magma body existed at a shallower depth within the volcanic centre.

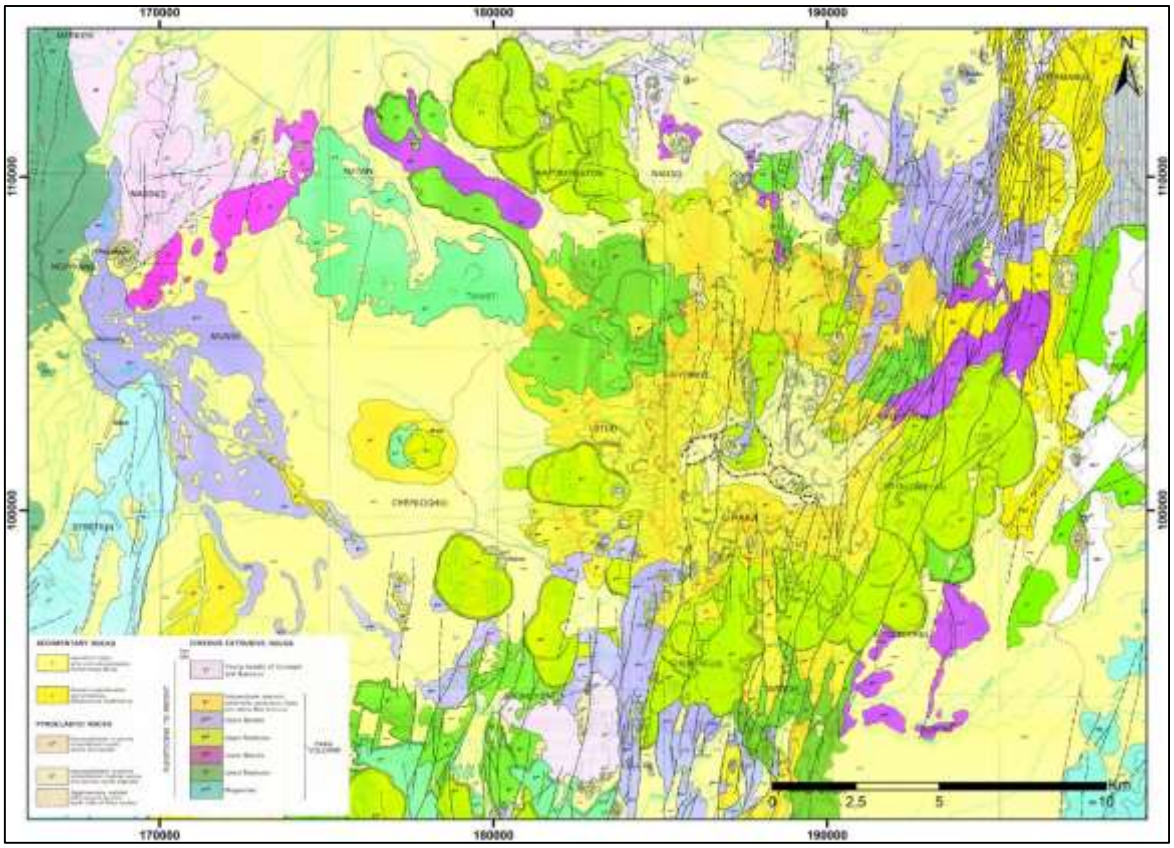

Figure 2: Geological map of Paka volcano (modified after Dunkley et al. 1993); grid: UTM zone 37 N, WGS-84.

3 InSAR - Interferometric Synthetic Aperture Radar

Modern Remote Sensing radar systems are generally termed as SAR-systems (SAR: Synthetic Aperture Radar). Radar systems are active systems and therefore independent of the given illumination. These systems send electromagnetic radiation and receive the reflected radiation from the surface (intensity). Radar systems are independent of the daytime of the acquisition and to the greatest possible extend of weather conditions (rain, clouds) due to the used wavelength. A brief overview about different frequency bands and wavelengths used by satellite radar sensors is given in table 2 (Ferretti, 2014).

Table 2: Different frequency bands and wavelengths used by satellite radar sensors (Ferretti, 2014).

Band	Frequencies	Wavelengths	Sensors
L	1 – 2 GHz	30 – 15 cm	SEASAT, JERS-1, ALOS-PALSAR
S	2 – 4 GHz	15 – 7.5 cm	HJ-1
C	4 – 8 GHz	7.5 – 3.75 cm	ERS-1, ERS-2, RADARSAT-1, RADARSAT-2, ENVISAT, Sentinel-1
X	8 – 12 GHz	3.75 – 2.5 cm	COSMO-SkyMed, TerraSAR-X, Tandem-X

To generate radar images with a high spatial resolution normally a huge antenna is required. For a spatial resolution of 2.4 m in the direction of azimuth (flight direction), an antenna with a length of 6.4 km would be necessary. As this is not practicable, a synthetic antenna is used for space borne radar systems (SAR). The resolution in azimuth and the length of the synthetic antenna can be calculated with the following equations (Equation 1). Figure 3 shows the difference of the resolution in azimuth and range direction.

$$\partial_{a\_synth} = \frac{D_{real}}{2} \qquad 2{,}4\ \text{m} = \frac{4{,}8\ \text{m}}{2}$$

Equation 1: Resolution in azimuth of SAR with an exemplarily calculation (Sörgel, 2008).

∂_{a_real} = *azimuth resolution of real antenna*
D_{real} = *real length of antenna*
∂_{a_synth} = *azimuth resolution of SAR*

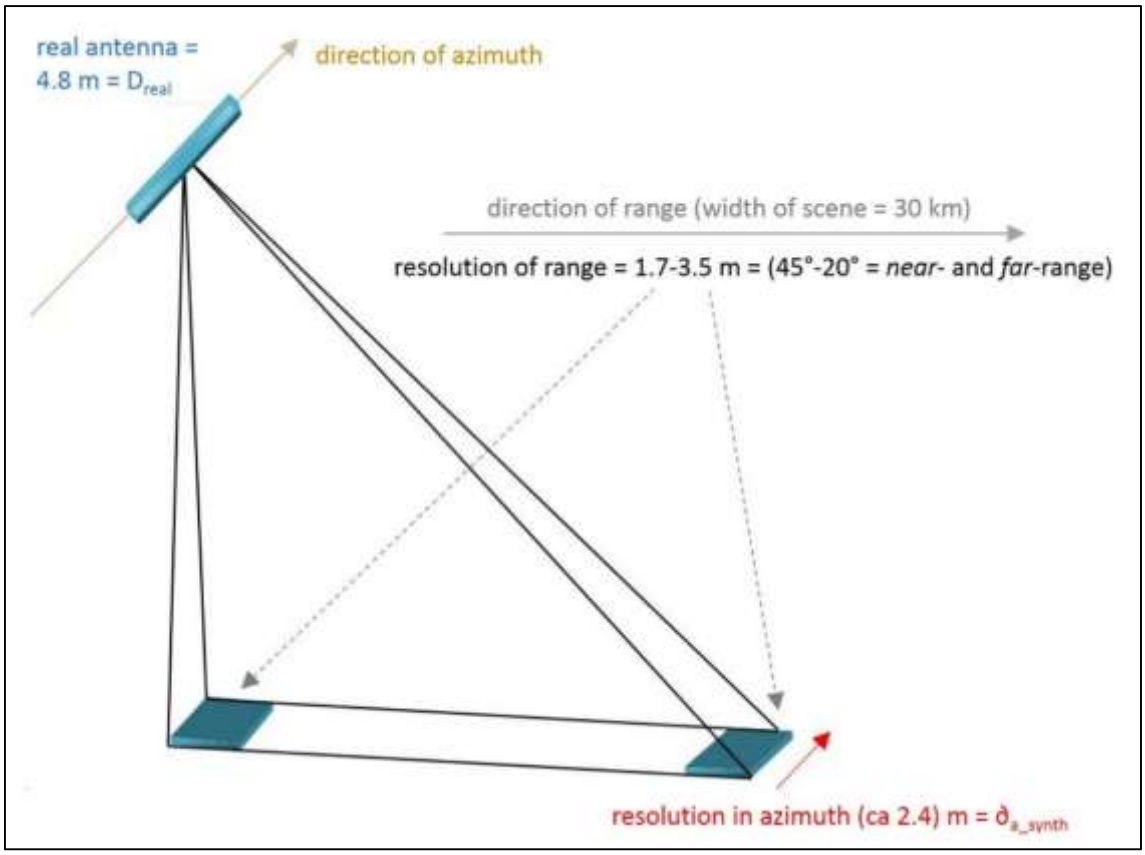

Figure 3: Demonstration of SAR resolution in azimuth and range direction.

An increasing wavelength leads to an increasing penetration depth into the surface. The approximate value for the penetration depth is half of the used wavelength for dry surface conditions. Due to the oblique recording technique of the radar system, geometric deformations may arise. These deformations are (a) layover, (b) foreshortening, (c) elongation, and (d) shadow.

a) Layover

Layover may arise at slopes facing towards the sensor within a topographic strongly moving terrain e.g. mountains with an intensive relief (Figure 4).

Radar images measure the runtime difference between sensor and object. If the reflected radiation from slope toe back to the sensor has a longer runtime than the area between peak and sensor, the peak will be displayed ahead of the slope toe (layover). Layover areas do not have usable information. Layover occurs if the incident angle θ_i of the sensor is smaller than the gradient of the slope facing the sensor.

Rectification based on a DEM (digital elevation model) will not lead to increase the information in that area.

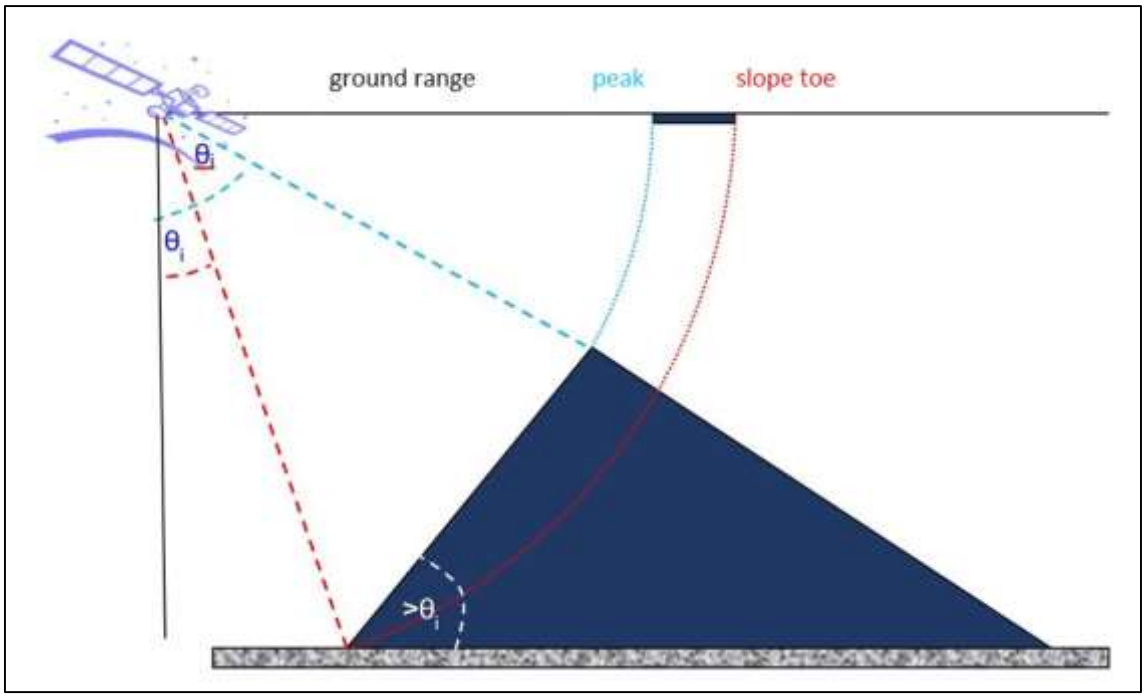

Figure 4: Development of a layover.

b) Foreshortening

Foreshortening also occurs on slopes that are facing towards the sensor and results in displaying a shortened slope in the image (Figure 5).

The real slope length is bigger than the projected ground range in the image. However, in this case there is the possibility of geometrical rectification based on a DEM. The more detailed the DEM, the better the reduction of the foreshortening. Foreshortening occurs if the incident angle θ_i of the sensor is bigger than the gradient of the slope facing the sensor.

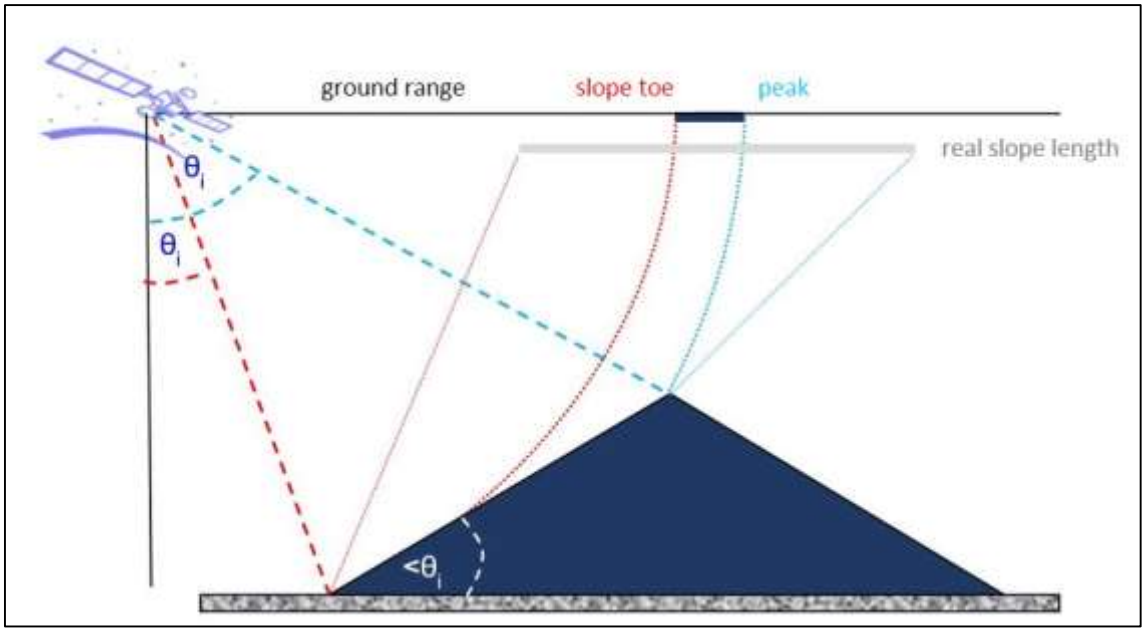

Figure 5: Development of foreshortening.

c) Elongation

Elongation occurs on slopes averted to the sensor and results in displaying an extended slope length in the image (Figure 6).

The projected slope length in the image is longer than the real length of the slope. By using a DEM for geometrical rectification of the image this effect can be minimized. The reduction of the elongation depends on the accuracy of the DEM. Elongation occurs if the depression angle θ_d of the sensor is bigger than the slope angle of the slope averted to the sensor.

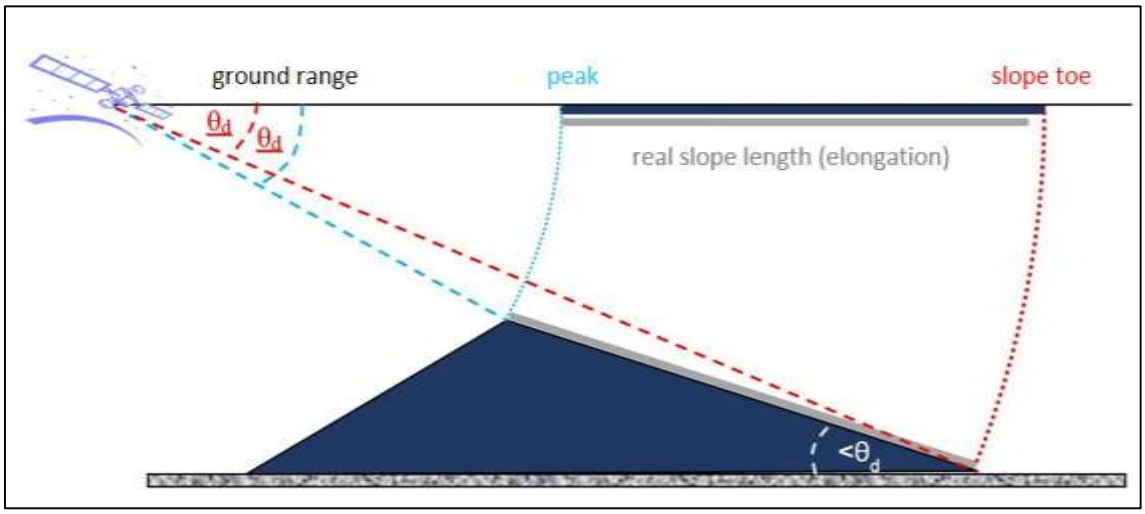

Figure 6: Development of elongation.

d) Shadow

Shadow appears only on slopes that are averted to the sensor. This areas are black in the image and do not have any information (Figure 7). Shadow occurs if the depression angle θ_d of the sensor is smaller than the slope angle of the slope averted to the sensor.

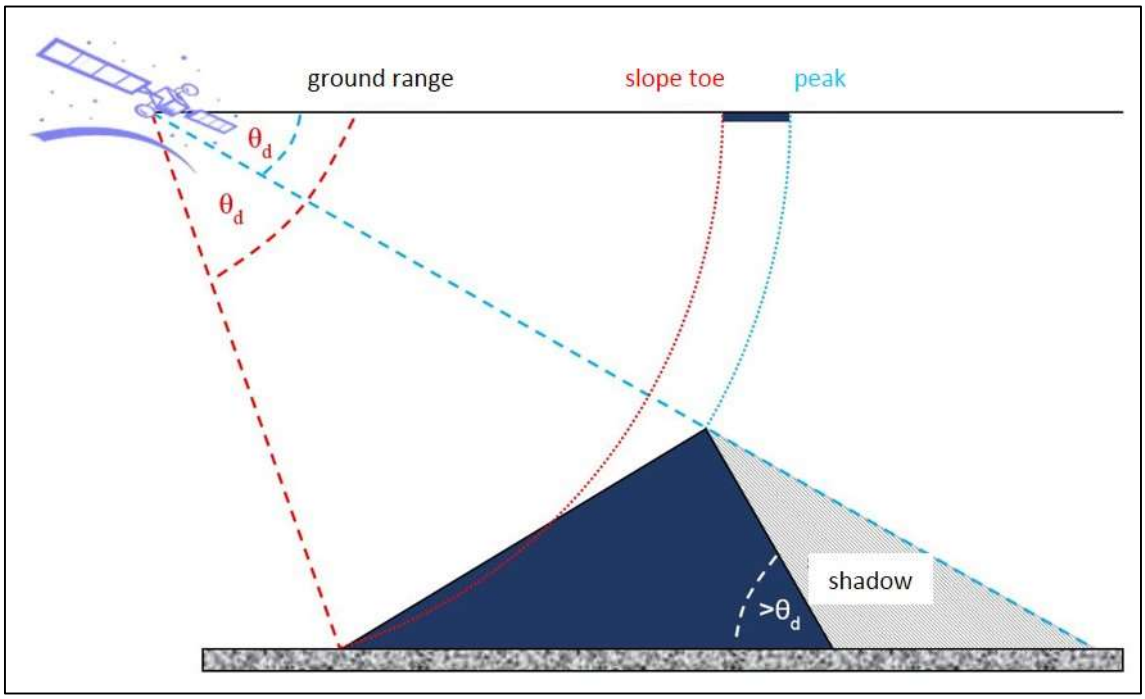

Figure 7: Development of shadow.

InSAR (Interferometric Synthetic Aperture Radar) exploits the phase difference of at least two SAR images (interferometric pair) acquired form different orbit positions and/or at different times (Bamler & Hartl, 1998). Figure 8 shows a simplified sketch of this method that can detect small surface displacements at a high resolution. A huge benefit of this method is the area-wide coverage. A ground-based measuring of such a large area would be very expensive and challenging. Biggs et al. (2014) claim that InSAR "can provide high-resolution maps of deformations, allowing the detection of unrest" at volcanoes. It is therefore an excellent method to measure ground deformations.

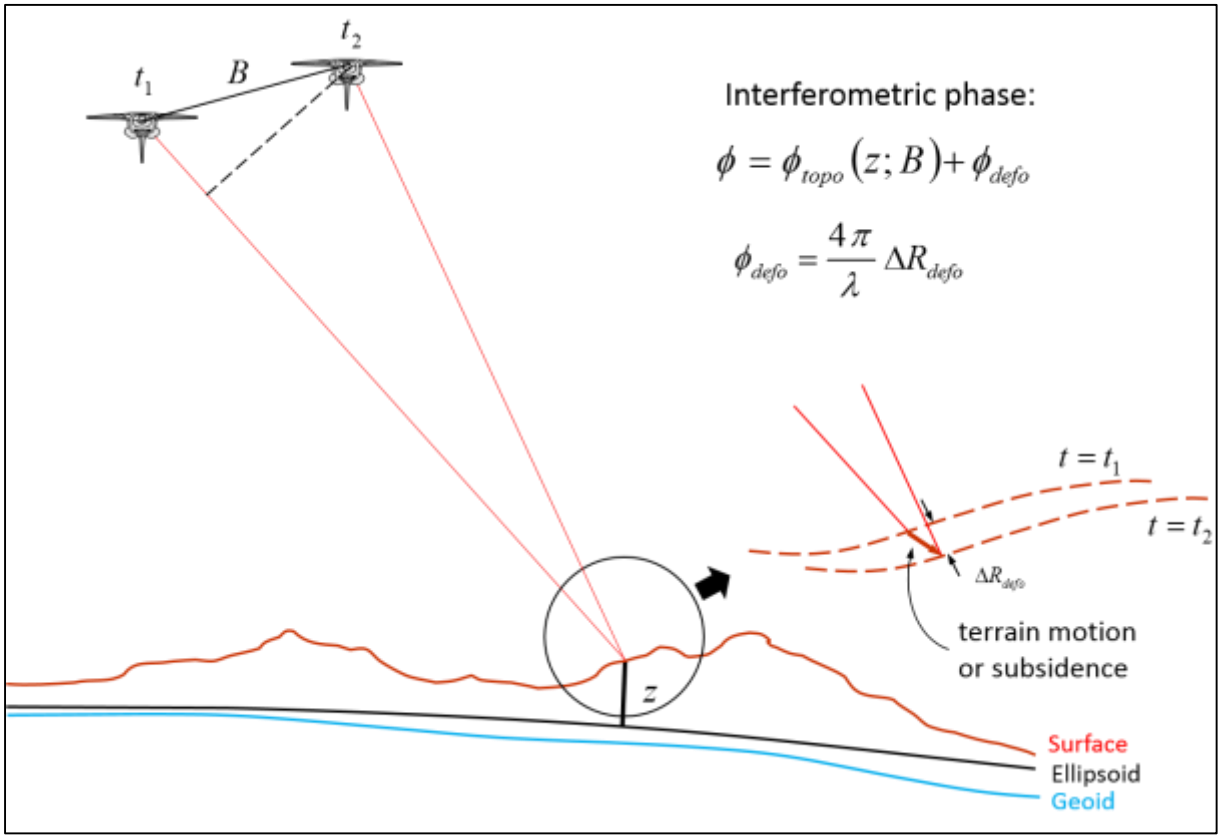

Figure 8: Sketch displaying how InSAR exploits the phase difference of at least two SAR images to detect vertical ground movement (modified after DLR, 2015).

ϕ = *interferometric phase*
ϕ_{topo} = *topographic phase*
ϕ_{defo} = *deformation phase*
z = *height with respect to ellipsoid*
B = *special baseline*
λ = *wavelength*
ΔR_{defo} = *range difference distance*

If there are more than two acquisitions with a time offset available for an area, a time series of the deformation can be evaluated. Such time series analyses are especially revealing for areas where there is a non-linear surface deformation expected. In a time series analysis, the phase difference of all interferograms is calculated and the deformation is estimated for each interferometric pair. For locations that are traceable on every interferogram over the complete recording period the deformation can be displayed as a time series plot (Figure 9).

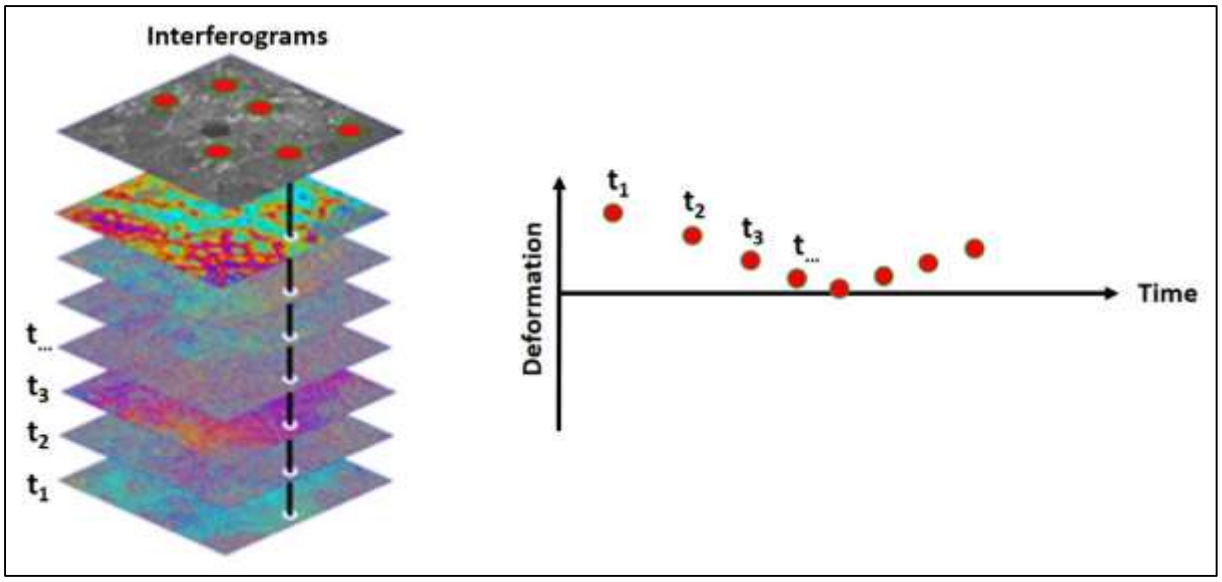

Figure 9: Evolution of deformation of a single location within a stack of interferograms.

3.1 InSAR studies of the project

Within this project, two InSAR studies were performed to evaluate deformations in the region of Paka volcano for different periods.

The first study using Envisat-ASAR data investigates surface deformations for the period between March 2006 and September 2010. The study covers an area of ~10,250 km² including Lake Baringo, Paka volcano, and Silali volcano from south to north. The footprint of the covered study area based on Envisat-ASAR data is displayed in figure 10.

The second study using TerraSAR-X data examines surface deformations for the period from March to October 2013. The study area includes Lake Baringo and Paka volcano and covers an area of ~1,900 km². The datasets of the TerraSAR-X satellite were recorded on specific acquisition for this project. The TerraSAR-X satellite is able to fly in different orbits, and to get an optimal footprint of the desired study area, the best fitting coverage was chosen for the recording of the SAR images. The coverage is displayed in figure 10.

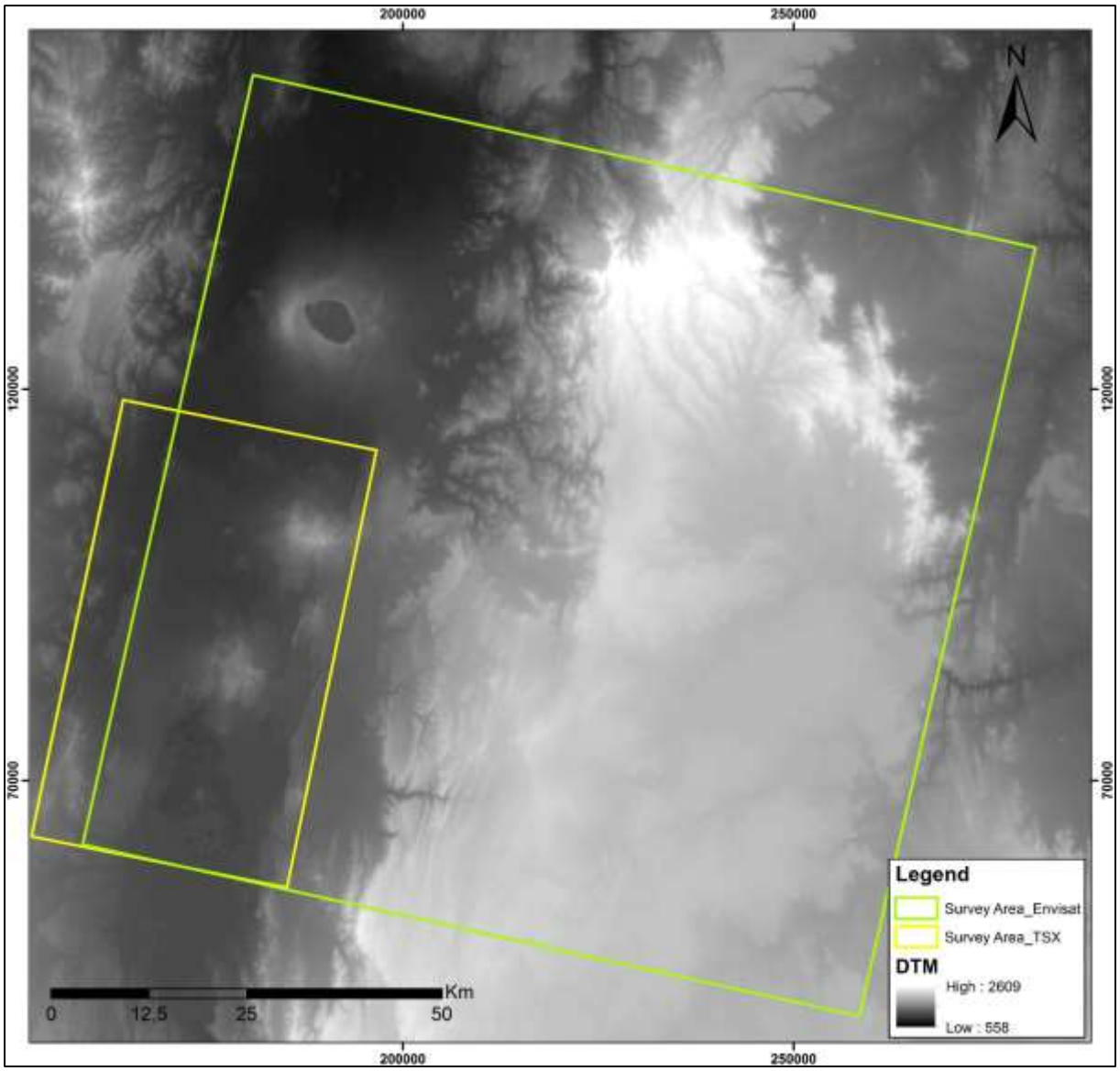

Figure 10: Survey areas of InSAR studies superimposed on the SRTM DEM (Shuttle Radar Topography Mission); green rectangle: InSAR study area based on Envisat-ASAR data; yellow rectangle: InSAR study area based on TerraSAR-X data. Grid: UTM zone 37 N, WGS-84.

3.2 Technical Background

The InSAR processing was performed by Airbus Defence & Space as a subcontractor of BGR. The TerraSAR-X data acquisition was part of the order.

3.2.1 Data acquisition of Envisat and TerraSAR-X studies

The survey area of the study based on Envisat data is covered by a single image mode (IMS) footprint of the satellite in descending orbit. The Envisat satellite carries the ASAR (Advanced SAR) sensor on board that operates in C-band with a wavelength centre at 5.6 cm corresponding to a frequency of 5.3 GHz (Cigna et al. 2012). Between 20/03/2006 and 20/09/2010, 13 scenes in VV polarization were acquired. Figure 11 shows the time plot of all available Envisat-ASAR scenes; table 3 shows the corresponding acquisition parameters.

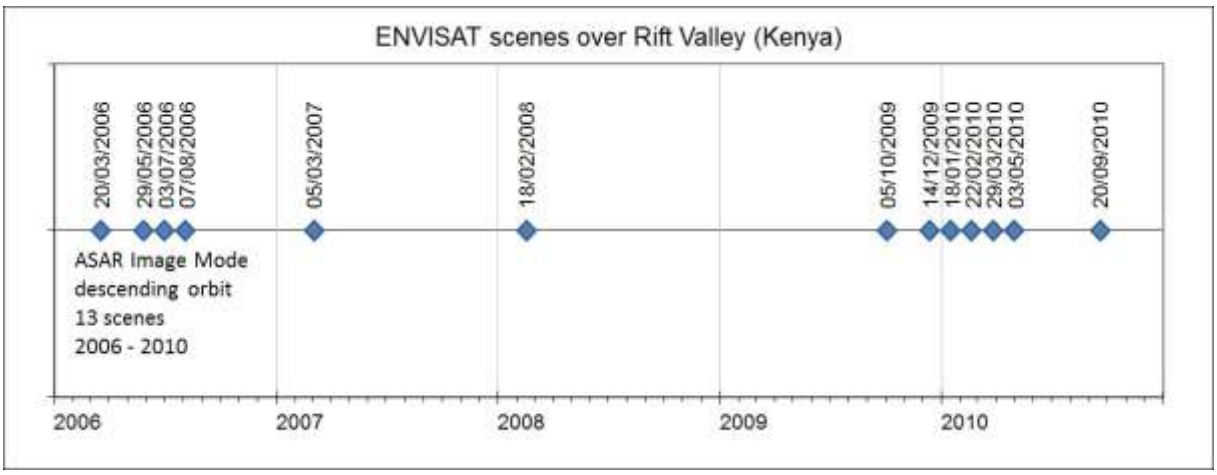

Figure 11: Time plot of the Envisat-ASAR scenes acquired between March 2006 and September 2010.

Table 3: Envisat-ASAR acquisition parameters.

Orbit	Beam	Incidence angle	Polarization	Mode
D	IS2	~23°	VV	IMS

The survey area of the study using the TerraSAR-X data is covered by one StripMap (SM) footprint of the satellite in descending orbit. The sensor on board of the TerraSAR-X satellite operates in X-band with a wavelength centre of 3 cm and a corresponding frequency of 9.65 GHz (www.dlr.de). During the period between 18/03/2013 and 24/10/2013, 17 scenes were acquired in HH polarization. Figure 12 shows the time plot of the acquisition dates of the TerraSAR-X scenes; table 4 shows the corresponding acquisition parameters.

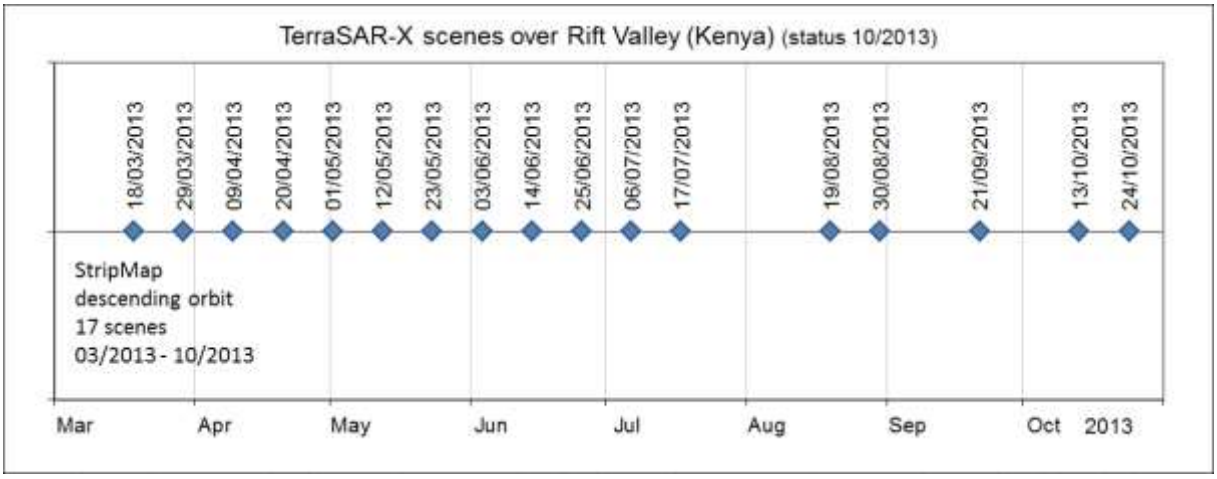

Figure 12: Time plot of the TerraSAR-X scenes acquired between March and October 2013.

Table 4: TerraSAR-X acquisition parameters.

Orbit	Beam	Incidence angle	Polarization	Mode
D	Strip_003	~21°	HH	SM

Satellites record data in ascending and descending direction. For circumpolar orbits of SAR satellites, half of their trajectory the satellites are travelling from north pole to south pole (descending orbit) and half of their trajectory the satellites are travelling from south pole to north pole (ascending orbit). Figure 13 shows a sketch illustrating both orbit directions.

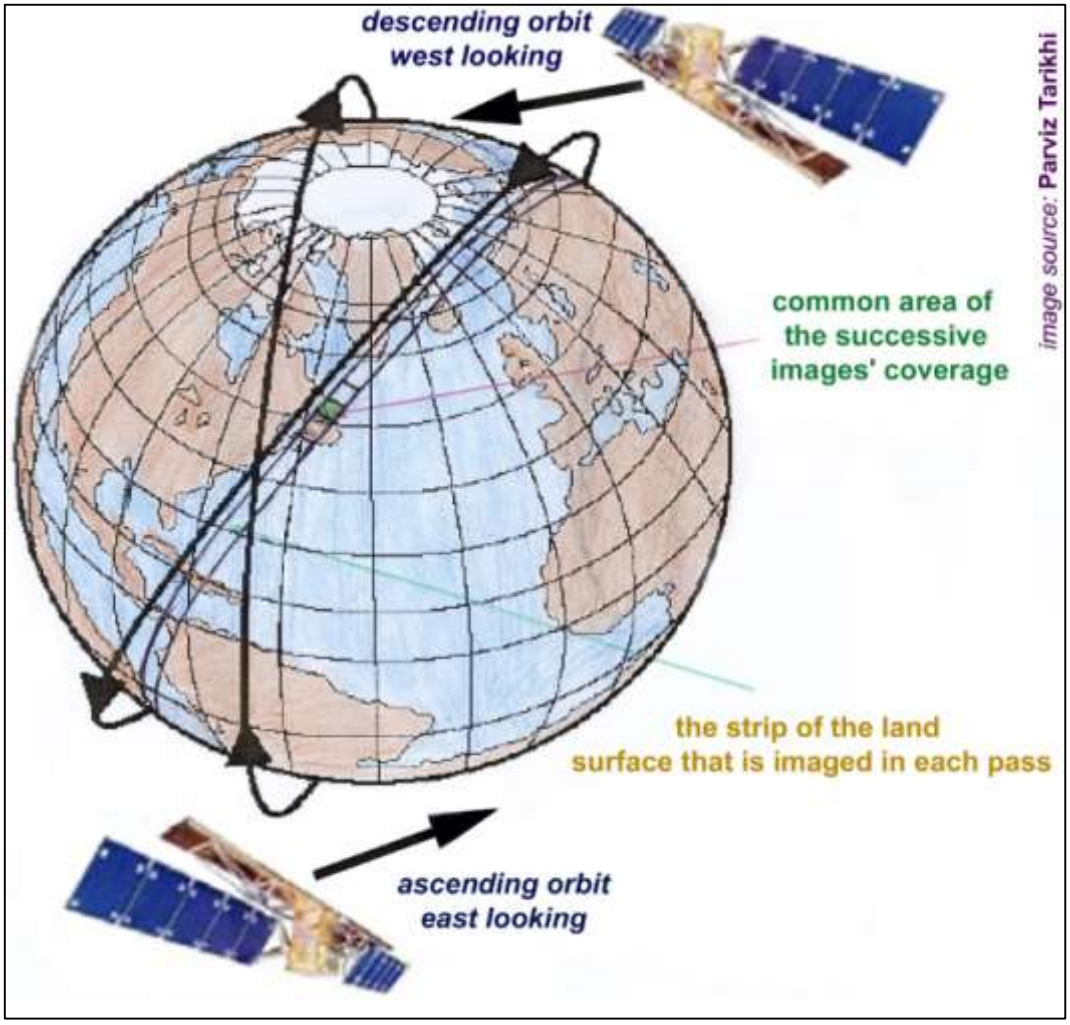

Figure 13: Sketch illustrating ascending and descending direction of satellites (Tarikhi, 2012).

For the ascending orbit, the line-of-sight of the satellite is towards the east, for the descending orbit the line-of-sight is towards the west. Due to the eastwards rotation of the earth, the footprints of the images acquired in the ascending orbit are not congruent with the footprint of the images acquired in the descending orbit of the satellite.

The angle between the true N - S and the satellite orbit varies slightly. Depending on the satellite, the angle lies in the range of ~10°. Figure 14 illustrates exemplarily the angle of the TerraSAR-X satellite.

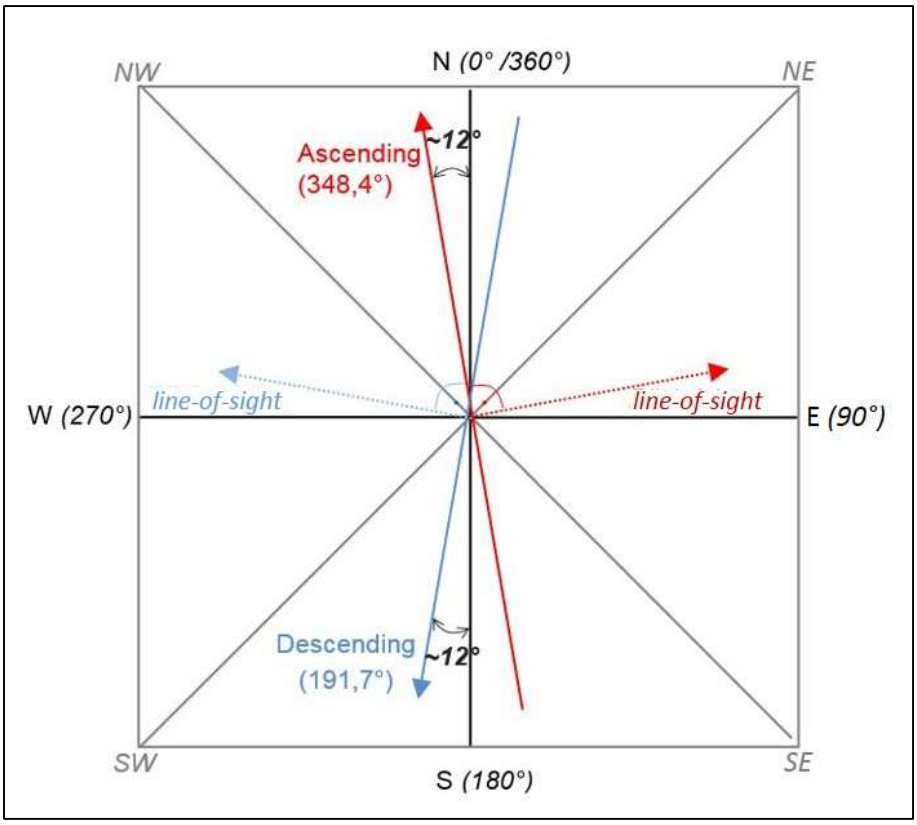

Figure 14: Comparison of ascending and descending orbit with the corresponding line-of-sight of the TerraSAR-X satellite.

3.2.2 Processing method

For both here presented studies, the Small Baseline Subset (SBAS) method was applied. The processing was performed using the sarmap S.A.´s SARscape software (Version No. 5). The SBAS method is an approach for the evaluation of the earth´s deformation evolution (Berardino et al. 2002) and extends a processing technique described by Lundgren et al. (2001) and Usai (2001).

The SBAS approach uses a large number of SAR acquisitions distributed in small baseline subsets. Small baseline (SB) refers to both, a small perpendicular baseline (spatial separation between orbits) and small temporal baseline (time separation between acquisitions). The method allows the easy combination of differential interferograms computed via standard processing techniques and computation of a time sequence of the deformation (Berardino et al. 2002). Berardino et al. (2002) furthermore state that a key feature of this method is the large number of SAR data acquisitions that allows an increase of the temporal sampling rate of the monitoring and the high degree of spatial coverage over the area of interest, related to the use of small baseline interferograms.

By the use of multiple small baseline interferograms, the SBAS method allows a time series analysis to detect non-linear surface deformations. For the area of Paka volcano, the SBAS method is suited best as in volcanic areas a non-linear deformation behaviour is expected.

3.2.3 Processing workflow

The processing workflow consists of different sections and steps. A simplified sketch illustrating the SBAS workflow is displayed in figure 15.

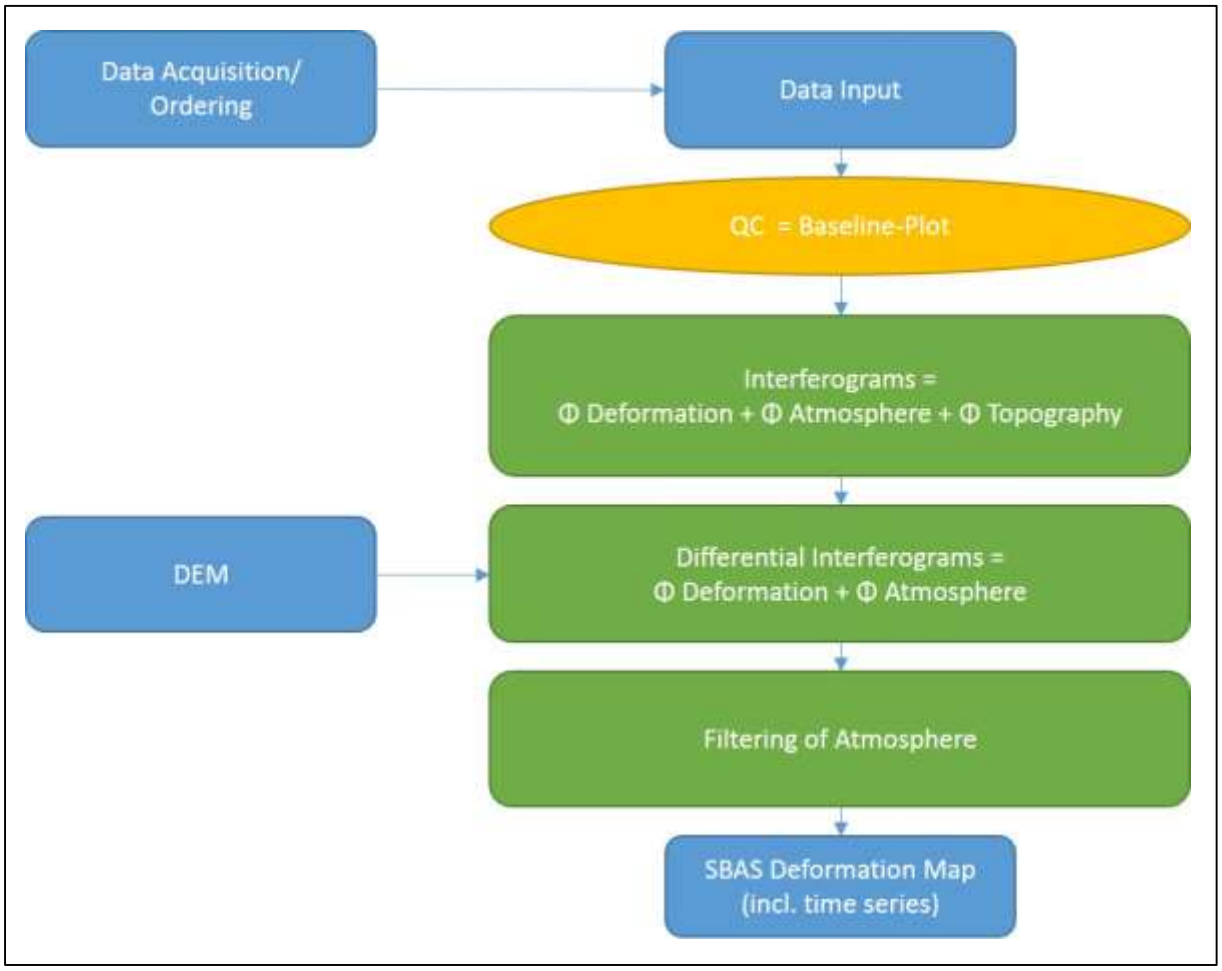

Figure 15: Workflow of SBAS processing.

The first step is the ordering of existing data or ordering the acquisition of data if no data is available for the area of interest yet from the data provider e.g. German Aerospace Center (DLR) for TerraSAR-X, European Space Agency (ESA) for Envisat, etc.

After data import into the software programme (e.g. sarmap SA), a quality control of all acquisitions is performed. This includes the examination of the perpendicular baseline (spatial separation between orbits) and the temporal baseline (time separation between acquisitions). If the perpendicular baseline increases beyond a limit known as the critical baseline, no phase information is preserved, the coherence is lost, and interferometry is not possible (Gatelli, 1994). These acquisitions are excluded from processing. The critical baseline can be calculated for every sensor using the following equation 2. Figure 16 shows a diagram of the critical baseline for the Envisat and TerraSAR-X satellites. For the TerraSAR-X data, the critical baseline is ~3,000 m, for Envisat-ASAR data the critical baseline is ~1,100 m.

$$B_{\perp,crit} = \left| \frac{W R \lambda \tan(\theta - \alpha)}{c} \right|$$

Equation 2: Calculation of critical baseline (Bamler, 2006).

$B_{\perp,crit}$	*= critical baseline*		
W	*= range signal bandwidth of sensor*	*Envisat: 16 MHz*	*TerraSAR-X: 100MHz*
R	*= slant range (line-of-sight);*	*Envisat: 869 km*	*TerraSAR-X: 550 km*
λ	*= wavelength*	*Envisat: 5.6 cm*	*TerraSAR-X: 3 cm*
θ	*= incidence angle*	*Envisat: 23°*	*TerraSAR-X: 21°*
c	*= speed of light*		
α	*= slope*		

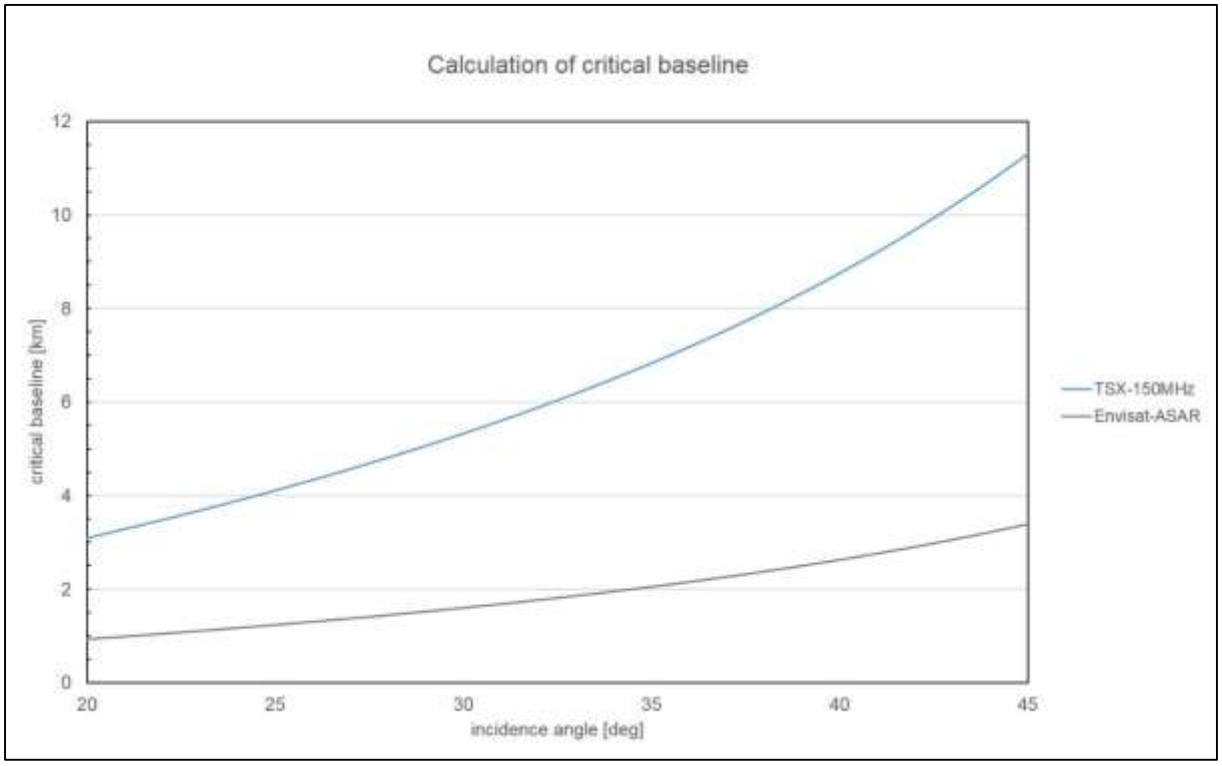

Figure 16: Plot of critical baseline of Envisat and TerraSAR-X satellites.

After this quality check, all different interferometry approaches can be applied in order to derive ground deformation estimations. In the presented study, the SBAS approach was applied as a non-linear deformation is assumed.

The first step of the actual SBAS processing is the generation of interferograms between all SAR acquisitions. The interferogram includes the phase information of topography, deformation, and atmosphere. The next step is the generation of differential interferograms, where the topography is corrected using a DEM. The selection of the DEM used for processing depends on the resolution of the SAR images. Generally, the DEM of the Shuttle Radar Topography Mission (SRTM) is used for InSAR processing. If the spatial resolution of the

SRTM is not sufficient, a DEM with a higher spatial resolution e.g. a DEM generated from TanDEM-X data needs to be used.

The third step of the processing chain is a custom atmospheric filtering on these preliminary results in order to recover the final and cleaned displacement time series. From the phase information of the differential interferograms, the atmospheric influence is subtracted using statistics to obtain the pure deformation values.

The post-processing includes a plausibility control via the “time series analyser” tool to check the deformation of points with subsidence or uplift behaviour in different areas over the complete investigation period. If there are too many points with extraordinary deformation values, the SBAS method has to be applied with different parameters e.g. with a different model (cubic, linear, quadratic), or the removal of “bad interferograms”. For both InSAR studies in the framework of this project, the cubic model was used for processing.

During processing, “refinement GCP´s” (Ground Control Points) are set in areas with no deformation during the investigation period. If reliable ground information with high accuracy is available, this information will be used. GCP´s are important, as uplift and subsidence values correspond to these stable points.

After processing, the ground deformation results are exported into the specific formats e.g. ESRI shapefile to be displayed as a deformation map.

3.2.4 Processing requirements of Envisat-ASAR data

For the interferometric time series analysis based on Envisat-ASAR data 13 scenes are achieved for the period between 2006 and 2010 (see figure 11). The quality check at the beginning of the processing workflow showed that two images (03/07/2006 and 07/08/2006) excess the critical baseline of 1,100 m (see figure 16) for Envisat-ASAR data (Holzner, 2003). These images are excluded from processing.

Figure 17 shows two amplitude images from 20/03/2006 and 20/09/2010 that display the intensity of the reflected radar signal. The amplitude images allow a first investigation on local conditions during the data acquisition period e.g. strong rainfall, heavy clouds, layover, and shadow. In areas where the change of the intensity is too strong, no information for that specific area is yielded.

In the available Envisat-ASAR data set, only slight discrepancies of the intensity are visible between the first and the last SAR acquisition. On the amplitude image (Figure 17), brighter colours imply a higher intensity of the reflected radar signal; darker colours imply a lower intensity. Flat smooth surfaces reflect the signal away from the sensor while flat rough surfaces reflect the signal back towards the sensor. Therefore, a smooth surface appears darker while a rough surface appears brighter. Differences of the intensity or rather discrepancies between SAR images are detected by the comparison of the images of the time series during processing (control of baseline or interferogram generation).

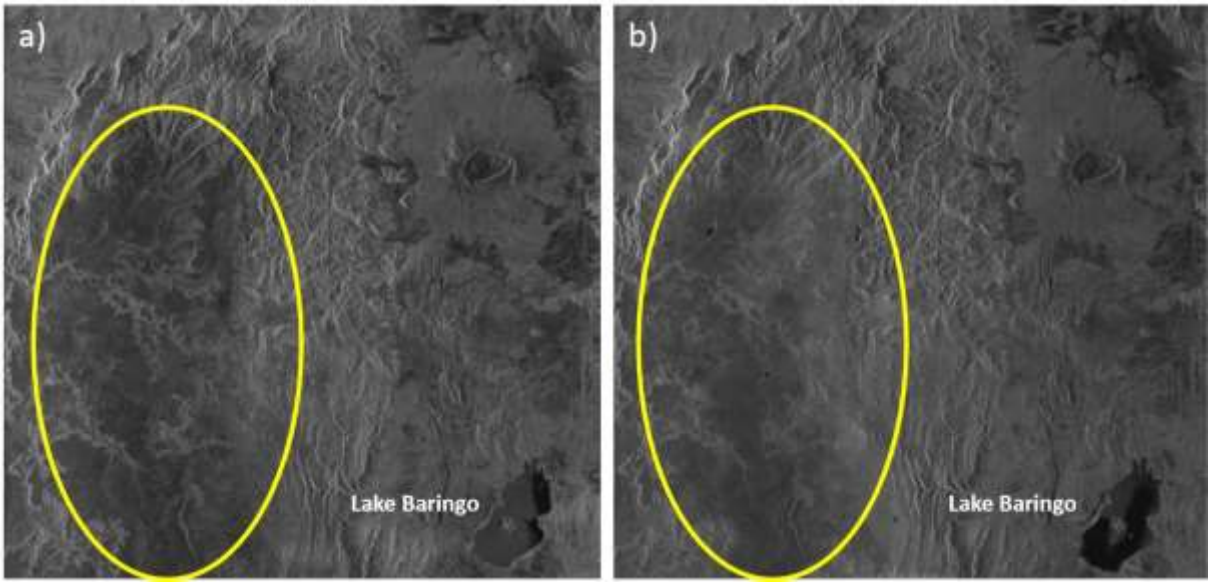

Figure 17: Amplitude images from a) 20/03/2006 and b) 20/09/2010 displaying the radar intensity reflections. Brighter colours imply higher intensity; darker colours imply lower intensity. Highlighted in yellow is an area with a slightly lower intensity of the image from 20/03/2006 compared to the amplitude image from 20/09/2010.

Due the acquisition mode of the satellite, the amplitude images are tilted in their E-W direction (see extent of Lake Baringo in figure 17). In descending mode, the flight direction (azimuth) of the satellite is from N to S, the direction of range is from E to W (Figure 18; see also figure 3). In the amplitude image, the pixels are displayed in the order of the acquisition: The first pixel acquired is displayed in the upper left corner etc. (Figure 18). During processing, the images remain in this E-W tilted form. The coherence map (Figure 19) of the next processing step is also tilted in its E-W direction. At the end of the processing, the images are georeferenced and appear in their correct geographical E-W extent.

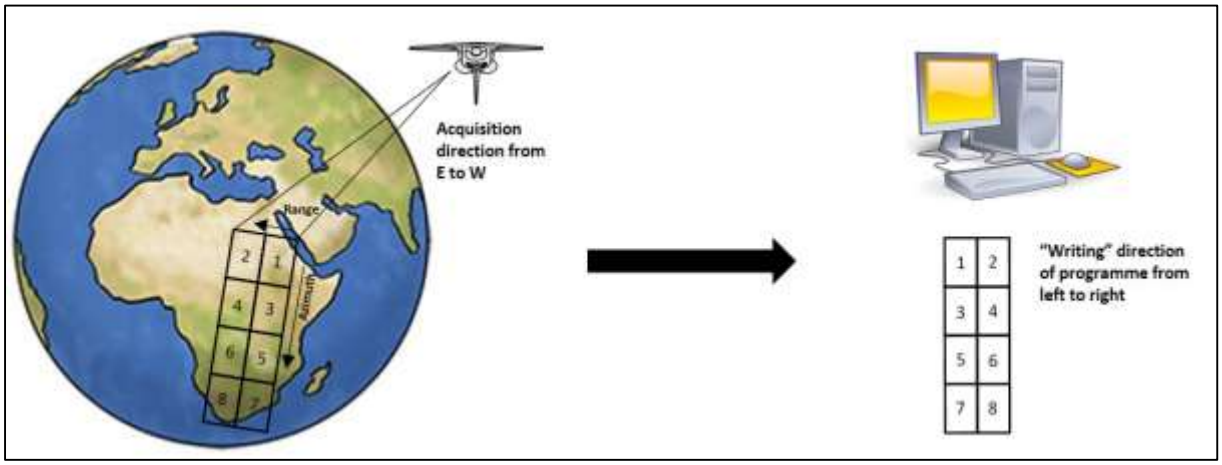

Figure 18: Sketch illustrating flight direction (azimuth) and range direction of the data acquisition. Amplitude and coherence maps are tilted in their E-W extent due to the “writing” direction of the programme.

The coherence is a key parameter of the interferometric processing and is used to detect long-term stable backscattering objects. This means, if a backscattering object on the surface does not change its physical behaviour over time, the backscatter is stable and the coherence is high. If the backscatter properties changes, the coherence of this backscatter decreases. Temporal decorrelation effects caused by e.g. vegetation growth, changes the backscatter properties and reduces therefore the coherence. Coherence maps can be generated by computing the cross-correlation coefficient of a SAR image pair (Equation 3). A SAR image pair always consist of a master scene (1st acquisition) and a slave scene (2nd acquisition).

$$\gamma = \frac{E\left[Z_M Z_S^*\right]}{\sqrt{E\left[\left|Z_M\right|^2\right] E\left[\left|Z_S\right|^2\right]}}$$

Equation 3: Cross-correlation coefficient to generate coherence maps (Prati et al. 1994).

γ = *cross-correlation coefficient*
E = *expectation operator*
Z_M = *master scene*
Z_S = *slave scene*

Figure 19 shows the coherence maps of a 35-day (14/12/2009 – 18/01/2010) interferogram and a 1470-day (20/03/2006 – 29/03/2010) interferogram, respectively. In the available Envisat-ASAR data set, the coherence decreases with an increase of the time separation between the SAR acquisitions (temporal decorrelation). The coherence loss is displayed as dark-grey to black colour pixels in the coherence maps (Figure 19). A strong vegetation growth affects the coherence negatively, whereas bare earth, rocks, or sparse vegetation keeps sufficient coherence values over time. If the coherence loss is too strong, no interferometric time series analysis can be derived anymore for that area.

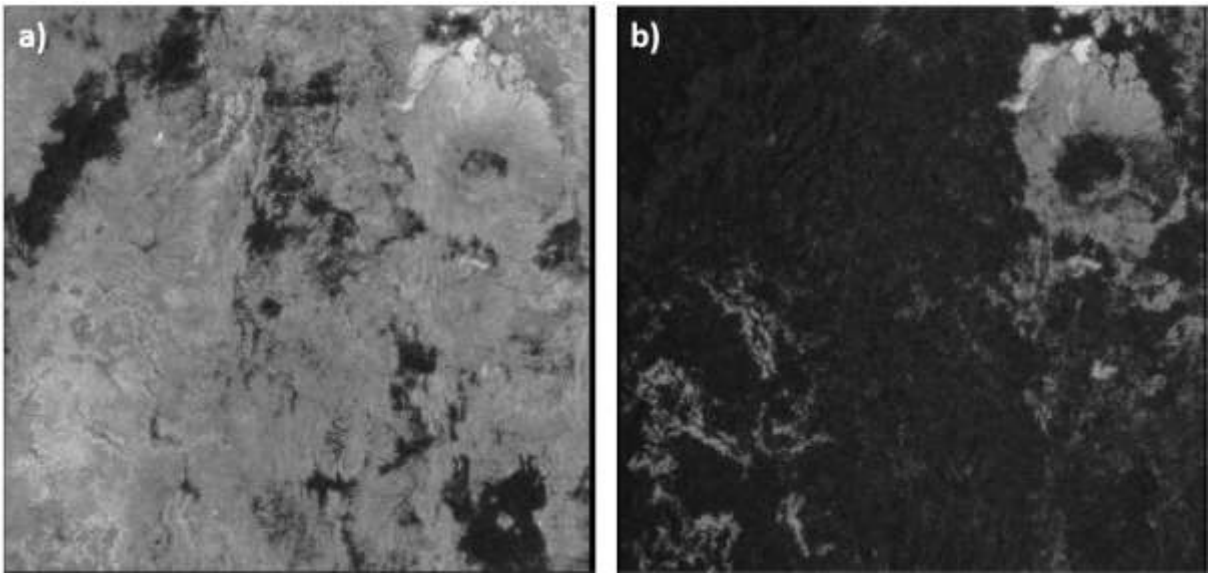

Figure 19: a) Coherence map for a 35-day interferogram (minimum temporal baseline); b) Coherence map for a 1470-day interferogram (maximum temporal baseline). Dark pixels indicate a loss of coherence. It is clearly visible that an increasing time separation produces a decreasing coherence.

The SBAS processing parameters for the study based on Envisat-ASAR data are compiled in table 5. Figure 20 shows the graphical representation of the geometrical baseline yielding a meaningful SBAS network. Displayed in red are the two SAR images from 20/03/2006 and 20/09/2010 that are excluded from processing as they exceed the critical baseline.

Table 5: Processing parameters regarding the data stack of figure 11.

Number of SAR images	Number of Interferograms	Maximum absolute baseline (m)	Minimum absolute baseline (m)	Maximum temporal baseline (d)	Minimum temporal baseline (d)
11	44	627	25	1470	35

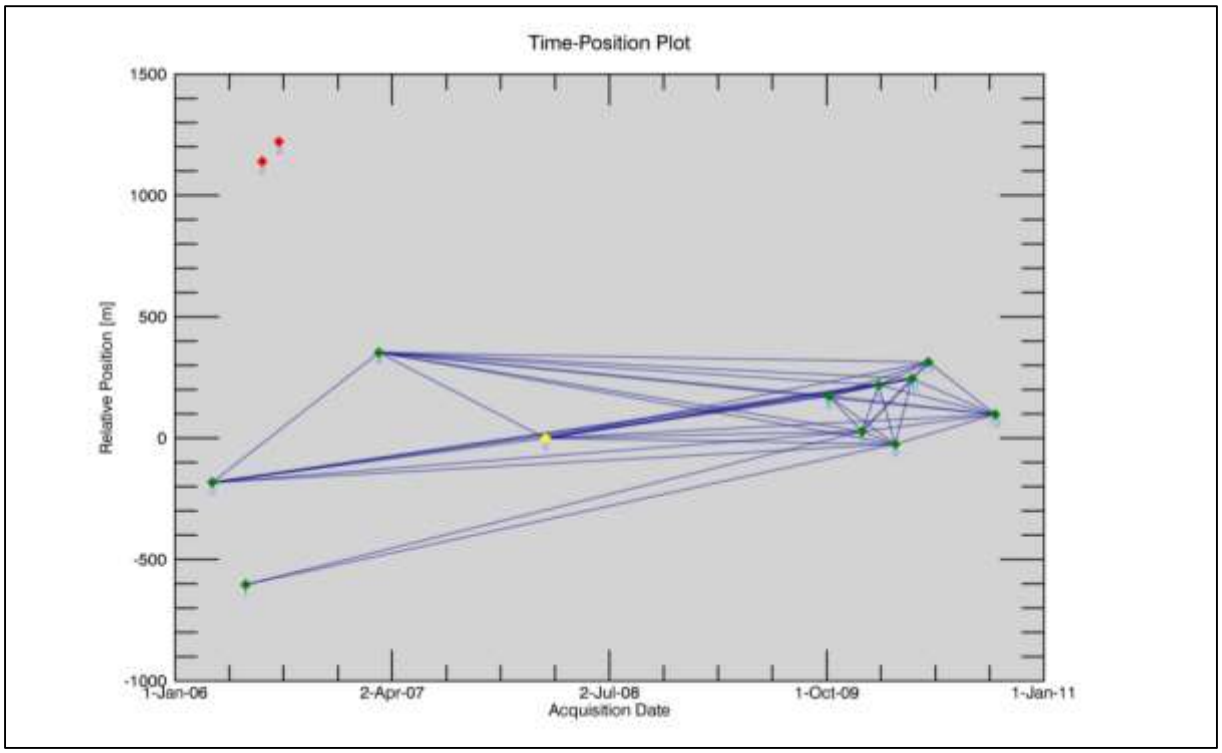

Figure 20: Time-Position-Plot of SBAS connection graph.

3.2.5 Processing requirements of TerraSAR-X data

The processing conditions for the interferometric time series analyses based on TerraSAR-X data are different from the parameters of the study based on Envisat-ASAR data. TerraSAR-X data acquisition was carried out especially for this project. Seventeen SAR images were acquired for the period between March and October 2013 (Figure 12).

Figure 21 shows the amplitude image of the first acquisition from 18/03/2013 and the last acquisition from 24/10/2013 displaying the intensity of the reflected radar signal. The amplitude images allow a first investigation of the local conditions during the data acquisition period e.g. strong rainfall, heavy clouds, layover, shadow etc. For areas with highly different intensities of the reflected radar signal, the coherence is lost and interferometric phase de-correlates.

For the TerraSAR-X data stack, almost no significant changes and discrepancies (different levels of brightness in the amplitude images) between the first and the last SAR data acquisition are recognised. Only Lake Baringo shows a strongly different reflection intensity. This change of intensity is most likely caused by wind that roughens the surface of Lake Baringo and increases therefore the intensity of the reflected signal. On the amplitude image, brighter colours imply a higher intensity, darker colours a lower intensity. Please note that the amplitude images are tilted in their E-W direction (explanation see chapter 3.2.4).

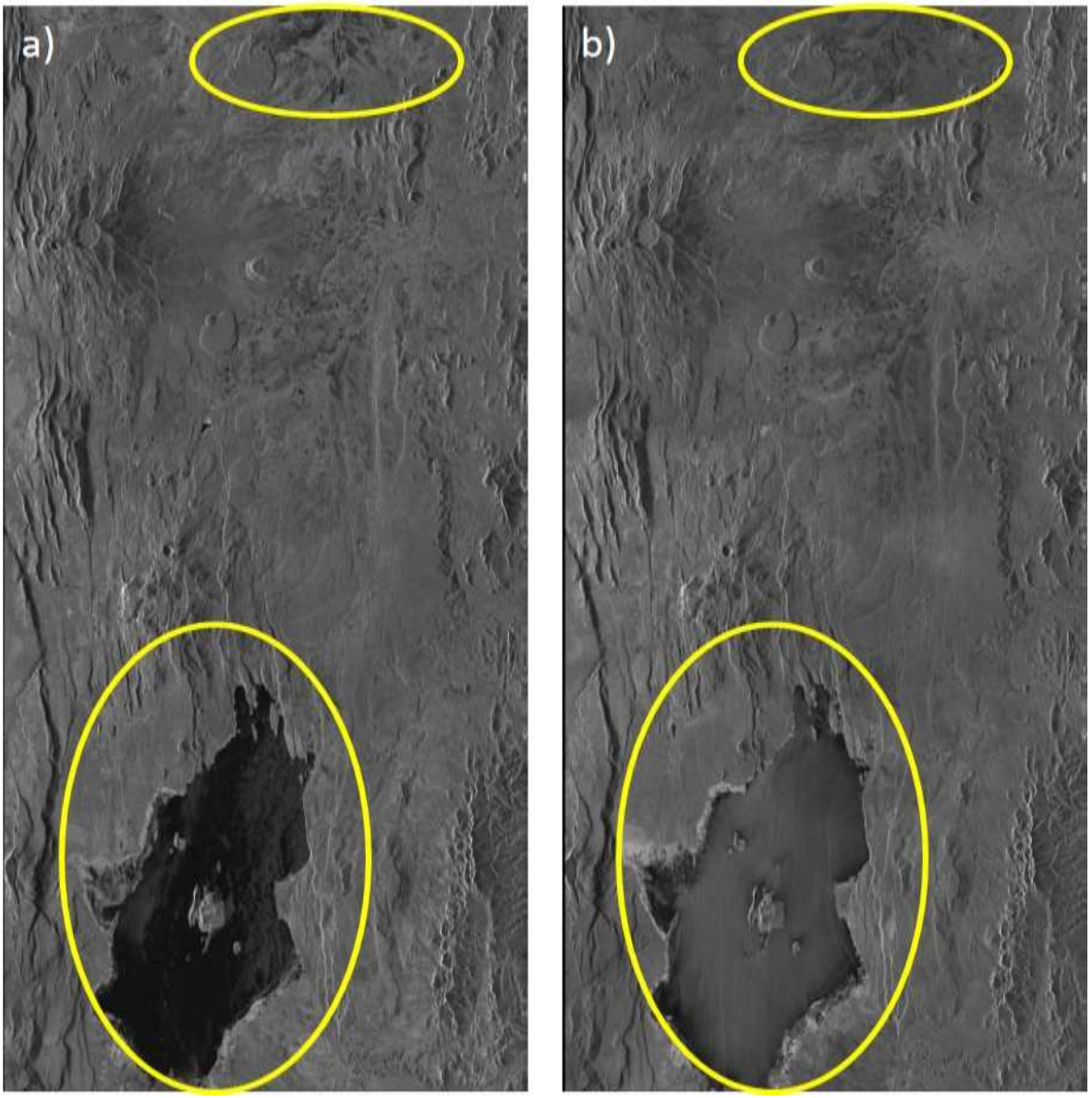

Figure 21: Amplitude images from a) first acquisition of 18/03/2013 and b) last acquisition of 24/10/2013, displaying mainly comparable radar intensity reflections. Brighter colours imply higher intensity; darker colours imply a lower intensity. Yellow ellipses: Visible is a strong difference in the reflection intensity of the water of Lake Baringo and a less intense difference in the northern part of the area.

Two coherence maps of TerraSAR-X data are shown in figure 22. Figure 22 a) displays the coherence maps of an 11-day interferogram (18/03/2013 – 24/03/2013) and a 220-day interferogram (18/03/2013 – 24/10/2013), respectively (Figure 22 b). Temporal and spatial decorrelation effects reduce the coherence and subsequently reduce the quality of the results. Brighter colours imply a higher coherence, darker colours a lower coherence. By the time the coherence is too low, no time series analysis can be derived for that area. The coherence decreases with an increase of the time span between the acquisitions (temporal decorrelation). In the case of the TerraSAR-X data based study, a strong coherence loss e.g. occurs in the area west of the Paka caldera were mainly alluvium is deposited (Figure 22; highlighted in yellow). This decrease of coherence could be caused by winds that change the physical appearance of the surface. In the resulting deformation map, no information about surface deformation will be yielded for these areas due to the loss of coherence.

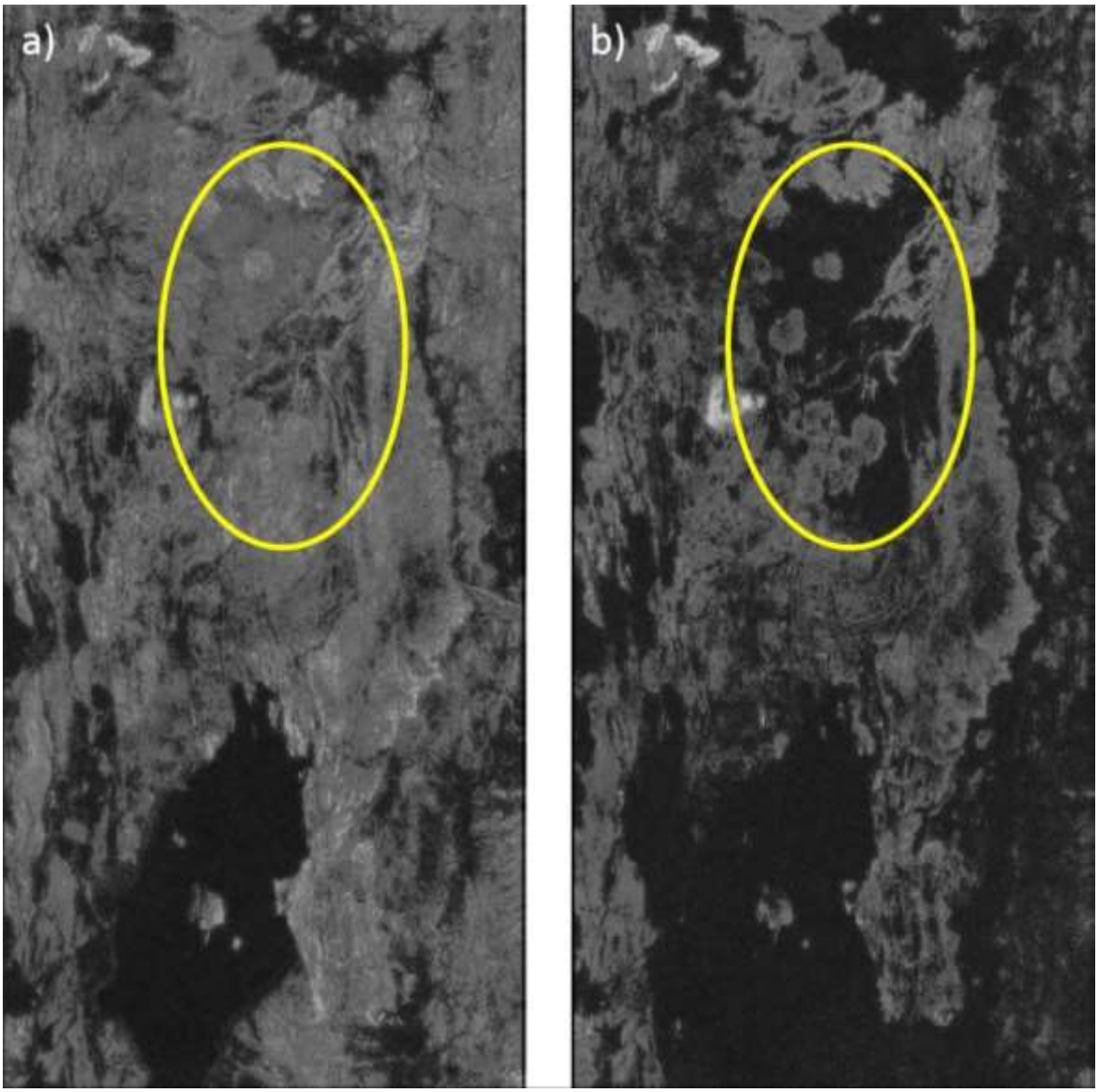

Figure 22: a) Coherence maps for an 11-day interferogram (minimum temporal baseline); b) Coherence map for a 220-day interferogram (maximum temporal baseline); recognisable is the loss of coherence with an increase of time separation between the acquisitions e.g. for the area with alluvial sediments (highlighted in yellow).

The SBAS processing parameters of the TerraSAR-X data based study are compiled in table 6. Figure 23 shows the graphical representation of the geometrical baseline yielding a meaningful SBAS network. All 17 SAR images could be used for processing as no image exceeds the critical baseline.

Table 6: Processing parameters regarding the data stack in figure 12.

Number of Input images	Number of interferograms	Maximum absolute baseline (m)	Minimum absolute baseline (m)	Maximum temporal separation (d)	Minimum temporal separation (d)
17	136	456	3	220	11

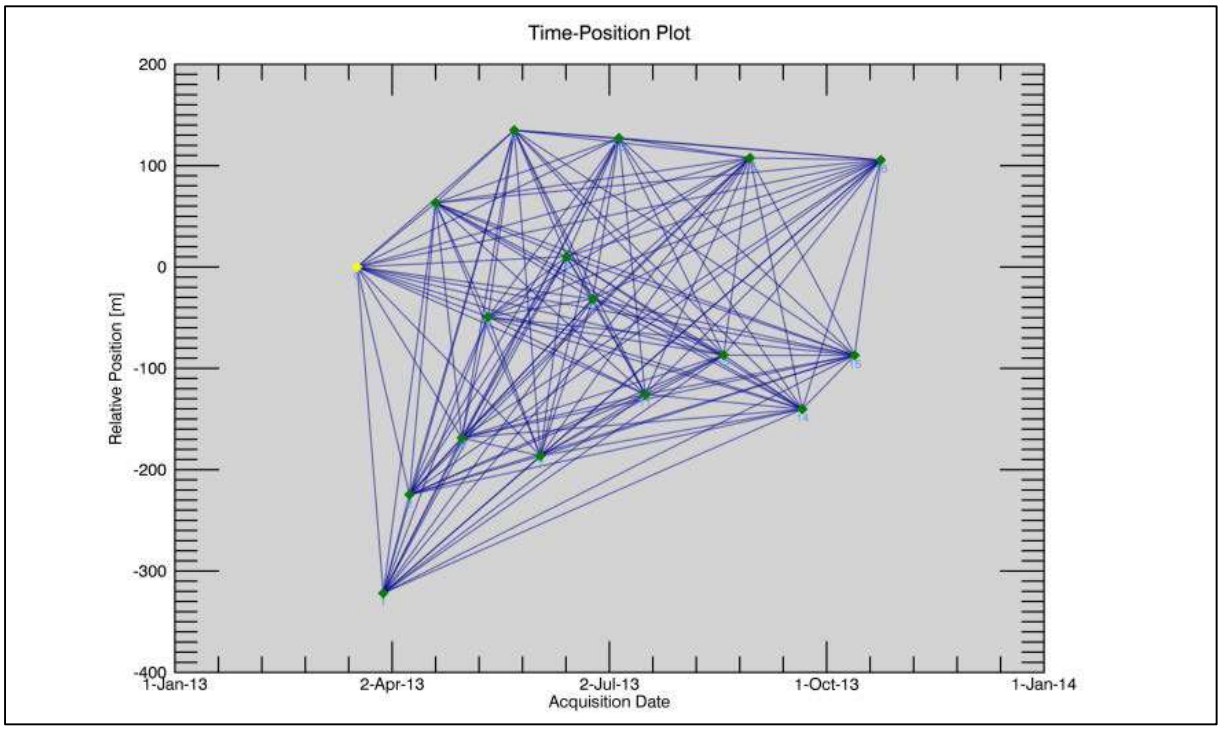

Figure 23: Time-Position-Plot of SBAS connection graph showing that all 17 SAR images are connected and therefore used for processing.

3.2.6 Digital elevation model

For the precise topographic phase correction during the processing of the InSAR data, a DEM is needed. By default, the SRTM DEM (Shuttle Radar Topographic Mission) is used for topographic phase correction (see chapter 3.2.3 above).

Figure 24 shows a differential interferogram of the TerraSAR-X acquisitions of 18/03/2013 and 29/03/2013 encompassing an 11-day time separation. One fringe (blue-to-red cycle) represents a distance change corresponding to half of the radar wavelength. In Figure 24, one fringe represents ~1.5 cm of displacement. The fringes displayed in the interferogram in figure 24 are not plausible to be caused by surface deformation only, due to short time separation of the acquisitions. That implies that the topographic phase correction was not sufficient due to the low resolution of the SRTM DEM.

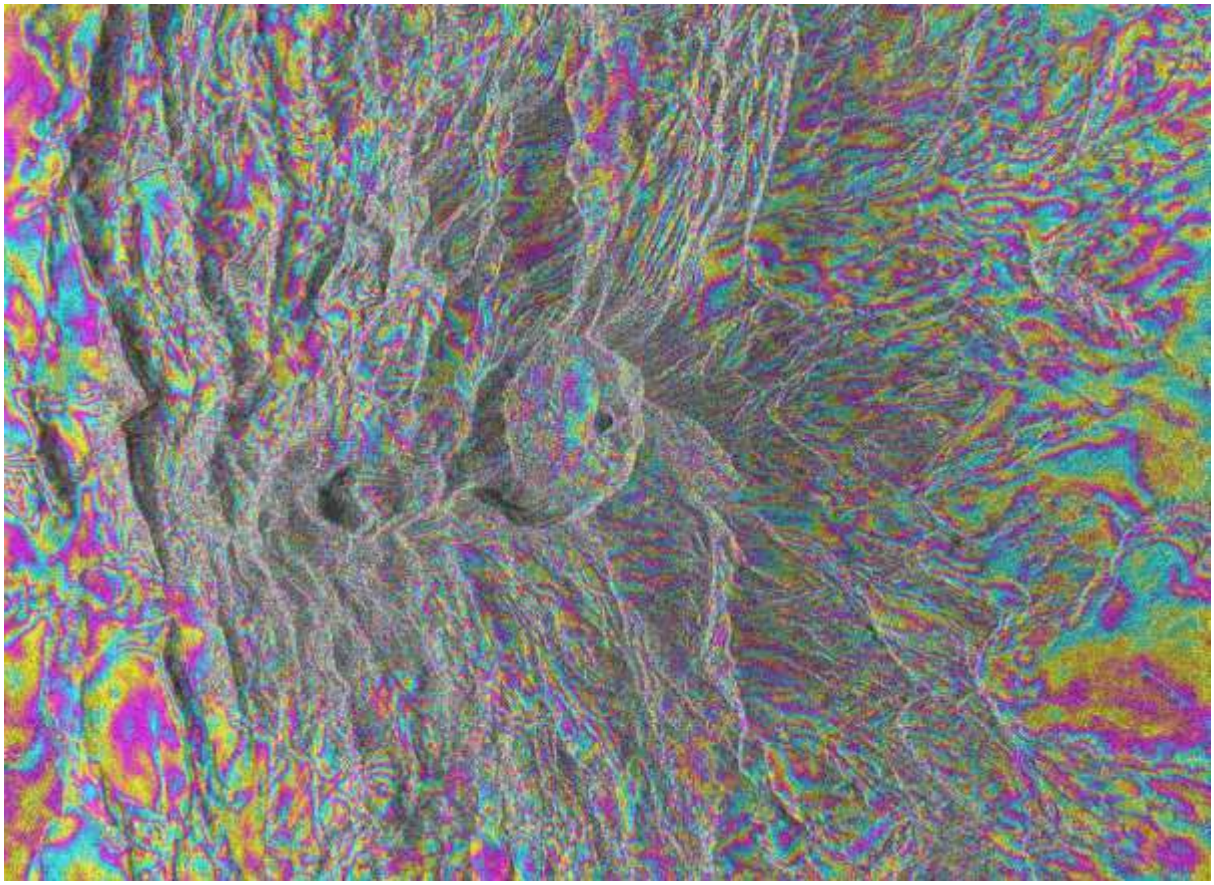

Figure 24: Interferogram (not geocoded) showing strong topographic phase contribution displayed as fringes in the area of interest. One fringe represents ~1.5 cm of displacement.

Therefore, a DEM with a higher resolution was needed for the processing of the TerraSAR-X data. This new DEM was generated from four TanDEM-X datasets that were compiled during different missions performed in 2011 and 2012 (Figure 26). After mosaicking these four single DEMs, the resulting DEM was embedded into the larger SRTM DEM frame. The TanDEM-X DEM covers almost the complete AOI of the study based on TerraSAR-X data. Only for a small area in the southeast, no TanDEM-X data was available. In that specific area, the less accurate SRTM DEM was used for processing. Due to the low topography of that specific area, the SRTM DEM was sufficient.

After the topographic phase correction using the TanDEM-X based DEM the misleading fringes that are visible in figure 24 disappear completely, and a differential interferogram (Figure 25), displaying only small phase changes (fringes) caused by deformation is generated.

As the processing of the Envisat-ASAR data was performed after the TanDEM-X DEM was generated the high resolution DEM was also used of the Envisat data processing even though the SRTM would have been sufficient for Envisat data.

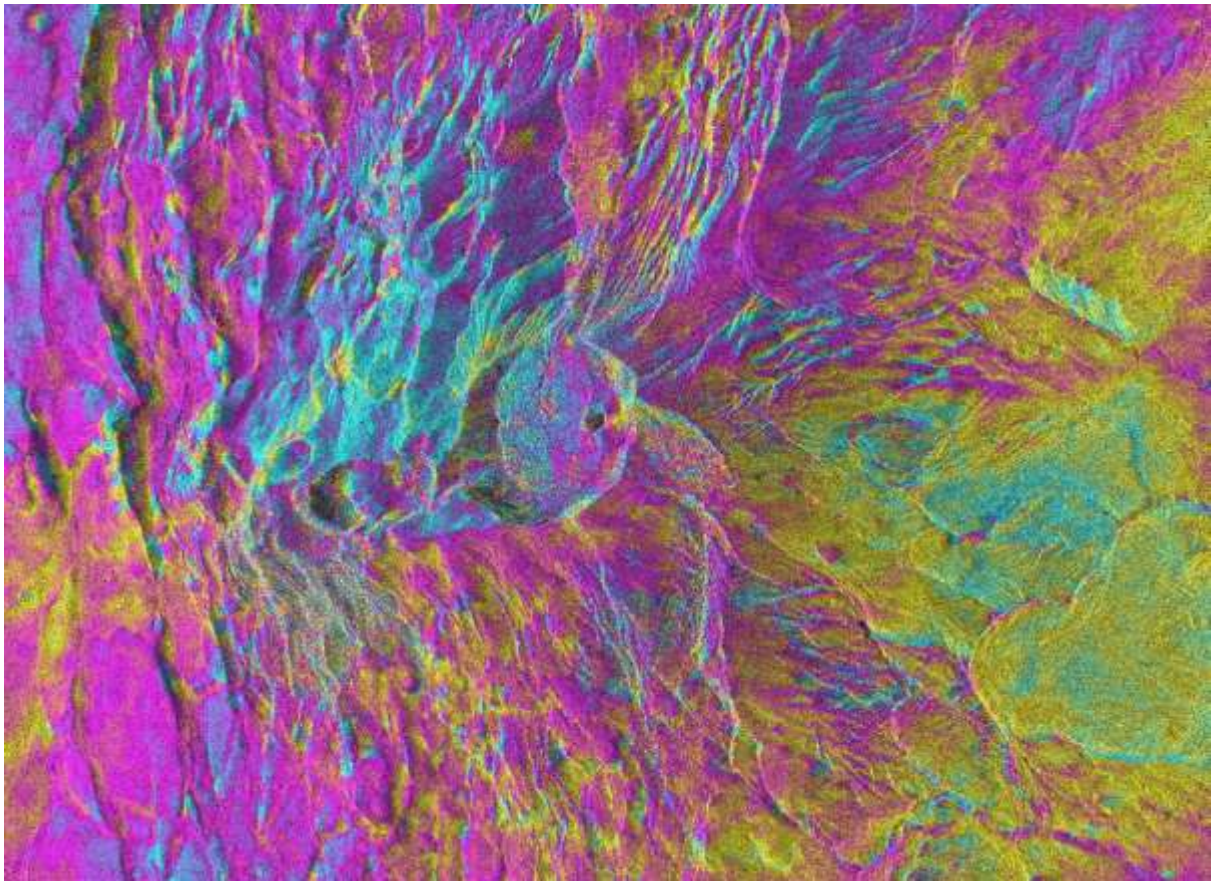

Figure 25: Interferogram of the same area as in figure 24 using high resolution TanDEM-X DEM for topographic correction.

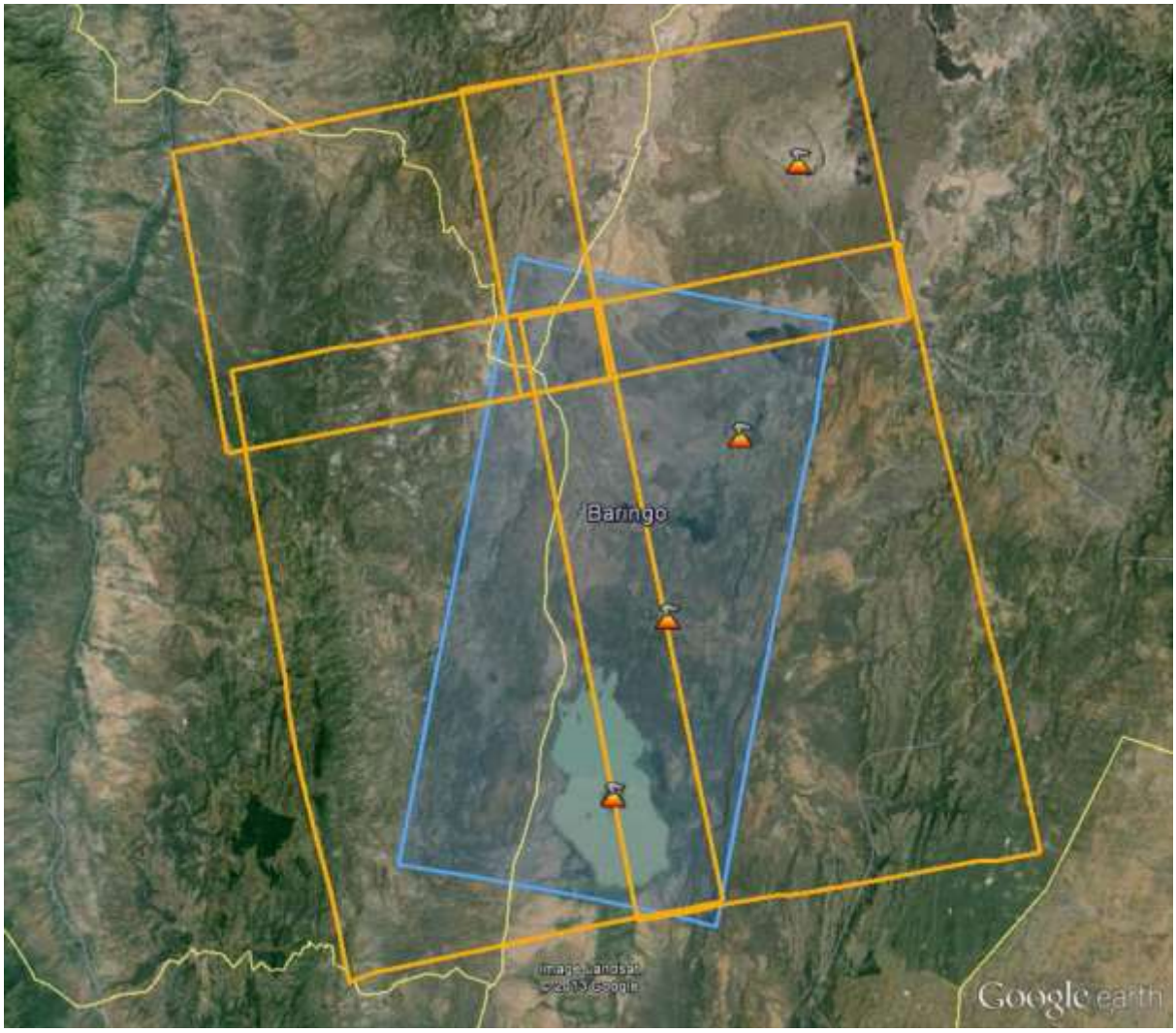

Figure 26: TanDEM-X data footprint (yellow) for the area of interest (blue). Background image Google Earth.

3.3 Precision and accuracy

As mentioned before, the SBAS method was used for the processing of the SAR data in both studies. The interferometric surface deformation monitoring indicates the **velocity** of the single time series points as average annual deformation rate in mm/year.

For the Envisat-ASAR data, the **precision,** e.g. the repeatability of measurements, can be given as several millimetres per year. For the TerraSAR-X data, the precision of the velocity can be given as 1 – 2 mm per year. The scale unit for the theoretical precision is always given in mm per year, no matter how long the recording period is. The precision values are calculated from goodness of fit values between the deformation model and phase values. **The precision of the velocity** for every pixel is given in column “V_Precisio” in the attached shapefiles for both studies (Attachments 3 and 4).

The accuracy estimates how close the mean velocity of the measurement points are to the truth of an independent measurement e.g. resulting from a terrestrial levelling campaign. It depends on several measurement parameters, such as data availability, surface signal reflection properties, temporal and spatial deformation characteristics, processing method and

the assumed stable reference pixel. Under ideal conditions, e.g. in urban areas, an accuracy in the range of the precision can be achieved. For areas with no precise terrestrial levelling data, as for the area of Paka volcano, the accuracy cannot be given.

Therefore, in both presented studies only the precision is given for each pixels velocity in *velocity±precision* (e.g. 7.27 mm/year ± 2.09 mm/year for point E 188860/ N 101372 of TerraSAR-X data).

Generally, single pixels with extraordinary high deformation rates (subsidence or uplift) that vary strongly from their spatial neighbourhood should be treated with care during the interpretation. For example, a feature (rock etc.) which is moving downhill, can be still captured by the radar signal but it is not a surface deformation.

The results of the interferometric time series have been made available as ESRI Shapefile (Attachments 3 and 4) and as Surface Deformation Map (Attachments 1 and 2). A description of the columns of the attribute table of the shapefile is given in attachment 5.

3.4 Analyses and interpretation

The analyses and interpretation of both InSAR studies were conducted separate due to the time gap between both data sets. They are therefore described separately in the following two chapters 3.4.1 and 3.4.2

3.4.1 Analysis of Envisat data

The results of the InSAR study based on Envisat-ASAR data are presented as a velocity map, an accompanying ESRI shapefile, and a time series plot of five points within the deformation area. The Surface Deformation Map shows the annual surface deformation values (Figure 27; attachment 1).

The deformation values are measured in the line-of-sight of the sensor. They have been projected into the height (Z-vertical) direction under the assumption that the total deformation occurs in the vertical direction (representing uplift or subsidence) and that the horizontal motion component is negligible.

The displacement values are calculated relatively to a GCP (Figure 27) and can be assumed to represent absolute deformation values under the assumption that the reference pixel is stable. That means the GCP is not subjected to any uplift or subsidence during the time of the observation.

The velocity values of the surface deformation map represent the average deformation per year. To determine whether the deformation has a linear or non-linear character, the investigation of the specific values of the time series is necessary (Figure 29).

The surface deformation map (Figure 27) shows that the whole area remains mainly stable during the entire investigation period. Table 7 presents the deformation characteristics within the survey area. An average velocity of the majority of the pixels of about - 3mm/year is measured. This value is within the theoretical precision of the method of a few mm/year (see chapter 3.3). Only one feature on the eastern flank of Paka volcano represents a prominent surface deformation (highlighted in blue in figure 27).

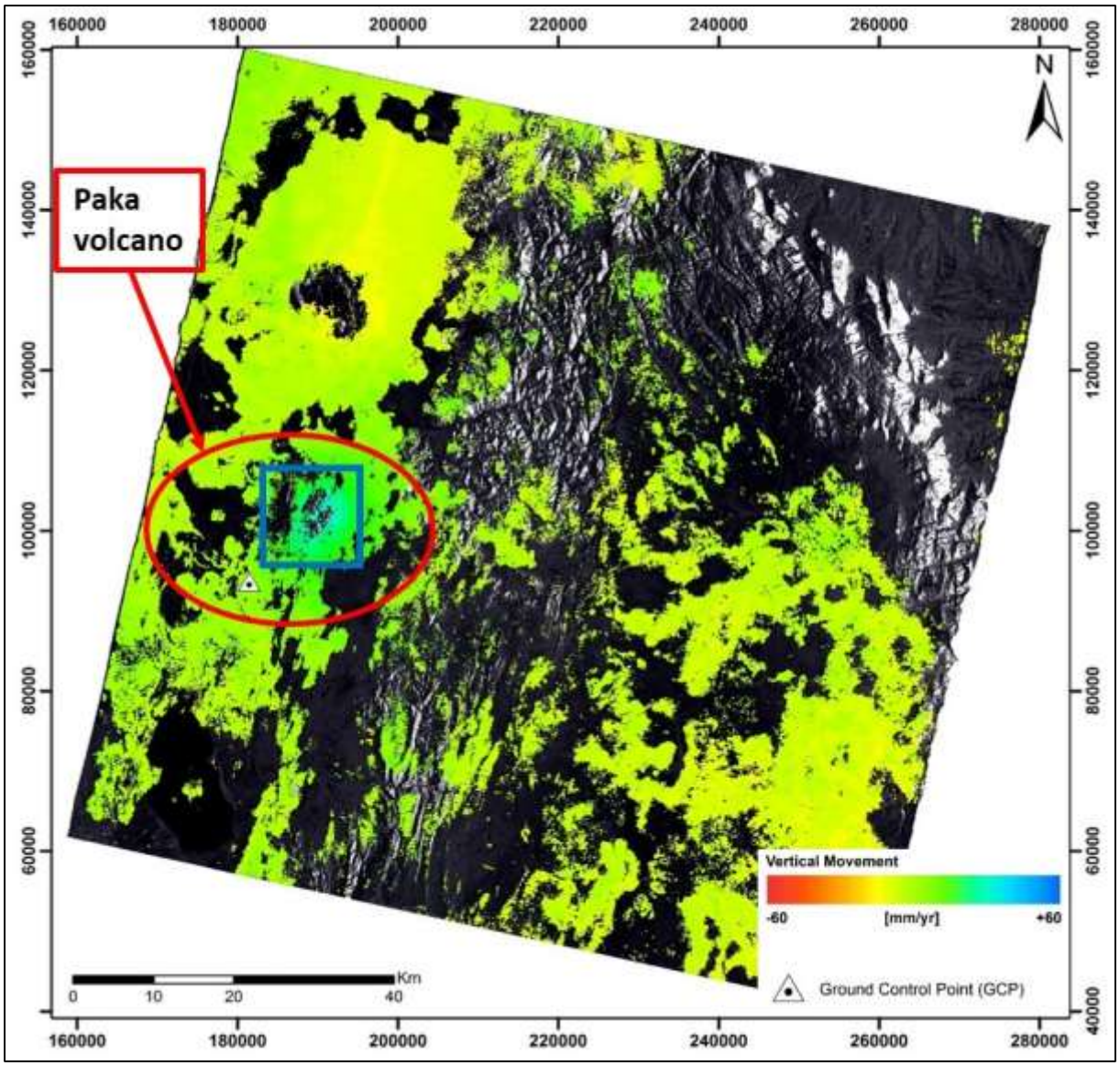

Figure 27: Annual surface deformation map generated form of the Envisat-ASAR data (20/03/2006 – 20/09/2010) superimposed on a geocoded Envisat amplitude image. The white triangle represents the selected GCP (Grid: UTM zone 37 N, WGS-84; E 181488/ N 93683); Highlighted in red is the area of Paka volcano; highlighted in blue is the area of uplift, compare figure 28.

Table 7: Measurement characteristics of the survey area of the Envisat-ASAR data.

Monitoring period	20/03/2006 – 20/09/2010
Ground Control Point (UTM)	N 93683 m / E 181488 m
Average annual velocity	-3 mm/year
Maximum subsidence (annual velocity)	-60 mm/year
Maximum uplift (annual velocity)	60 mm/year
Measurement pixel density	365 pixel/km²

The prominent deformation feature of the area covered by Envisat-ASAR data is an area of uplift on the eastern part of Paka volcano (Figure 28). The area has an extent of ~40 km² and covers Paka`s eastern flank and the eastern part of Paka´s caldera. The average annual deformation rates for the investigation period of 5 years are up to ~30 mm/year. By analysing five single points (Figure 29) within the area of deformation, it can be observed that there was a strong uplift of up to ~20 cm between March 2006 and February 2008, whereas during the following period until September 2010 the area turns to be nearly stable. By selecting points for a time series plot, the points should show comparable values to the measurement points within their spatial neighbourhood. Spatially isolated points or points with extremely high or low velocity values should be treated with care during the interpretation as they could be artefacts, collapse structures, or single features moving downhill captured by the radar signal. Figure 30 shows three measurement points with a subsidence deformation rate of up to -55mm/year (E 189 196/ N 99522) within an area of uplift. Ground truthing of such areas is recommended to check the reason for the extraordinary deformation values.

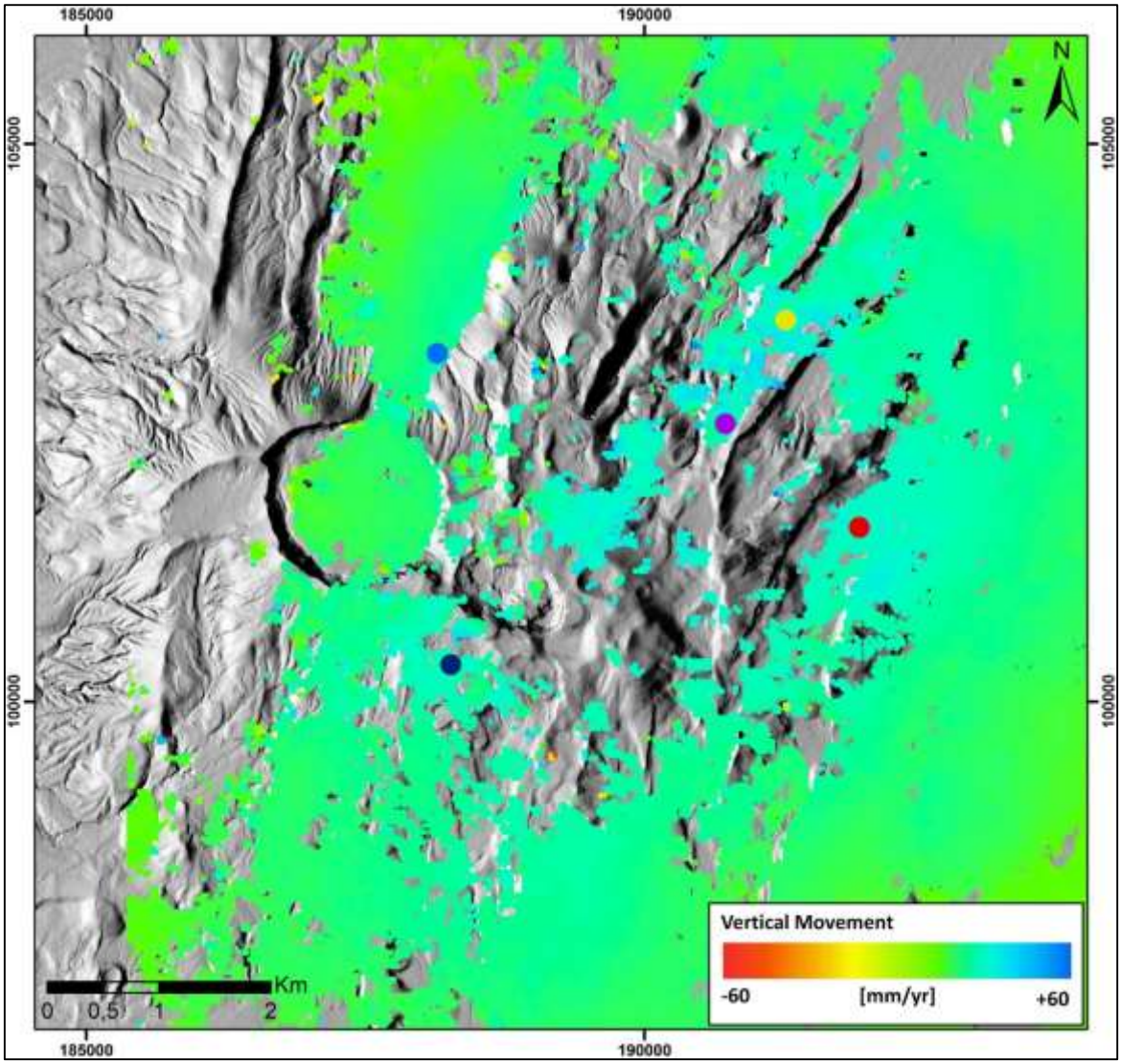

Figure 28: Subset of the surface deformation map (Figure 27; blue rectangle) showing the uplift area at Paka volcano superimposed on a shaded relief map created from the DTM based on Pléiades data that was generated in the framework of this project (Chapter 4). Coloured dots are locations of points displayed in the time series plot (see figure 29). Grid: UTM zone 37 N, WGS-84.

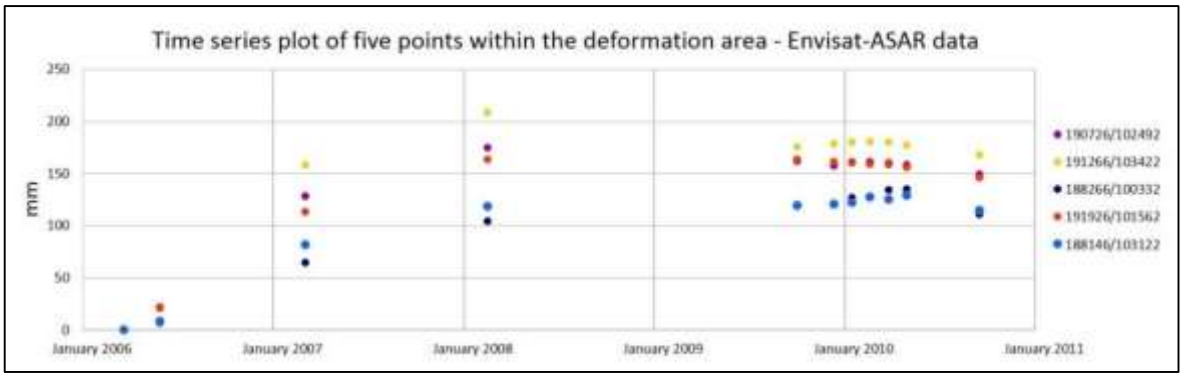

Figure 29: Time series plot of five points within the deformation area on the eastern flank of Paka volcano showing an uplift of ~20 cm that ends between February 2008 and October 2009. During the period of October 2009 and October 2010, the area remains stable.

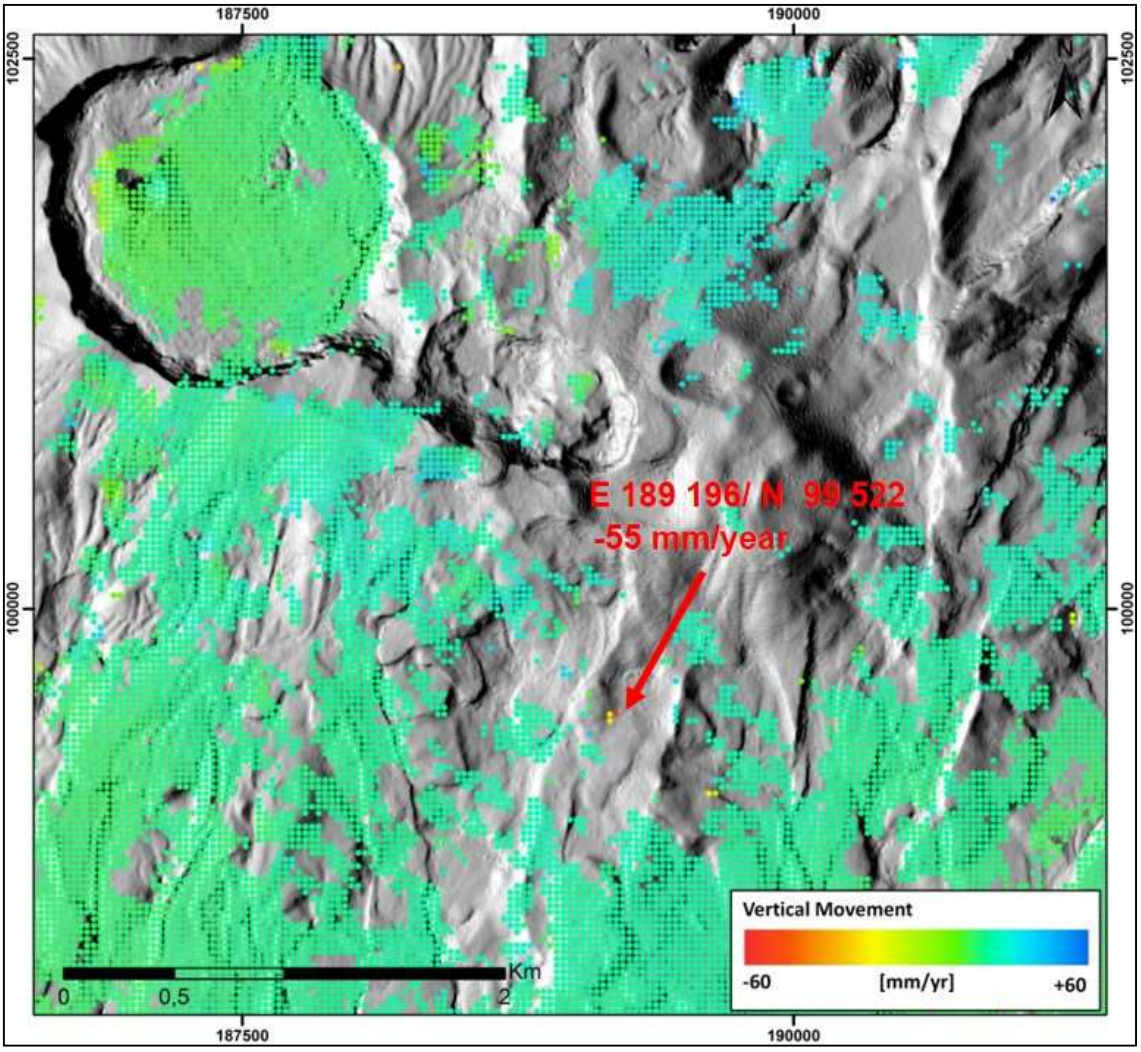

Figure 30: Three isolated points with extremely high subsidence rates (up to -55 mm/year for E 189 196/ N 99 522) within the area of uplift. These points could be e.g. artefacts or collapse structures and are treated with care during the interpretation. Grid: UTM zone 37 N, WGS-84.

The result of the recent analysis shows an uplift on the eastern flank of Paka volcano between 2006 and 2008 and the following phase of stability (Figure 31b) correlates with the results of two previous studies performed by Biggs et al. (2009 and 2013). For the first study, Biggs et al. (2009) used the same Envisat-ASAR dataset to process differential interferograms, but no Deformation Maps. Figure 31a shows a stack of three interferograms covering the inflation period between 2006 and 2007. The interferogram displays an uplift of 21 cm during that period. Each fringe (blue-to-red cycle) represents 2.8 cm of displacement in the satellite line-of-sight (Biggs et al. 2009) of the Envisat-ASAR sensor.

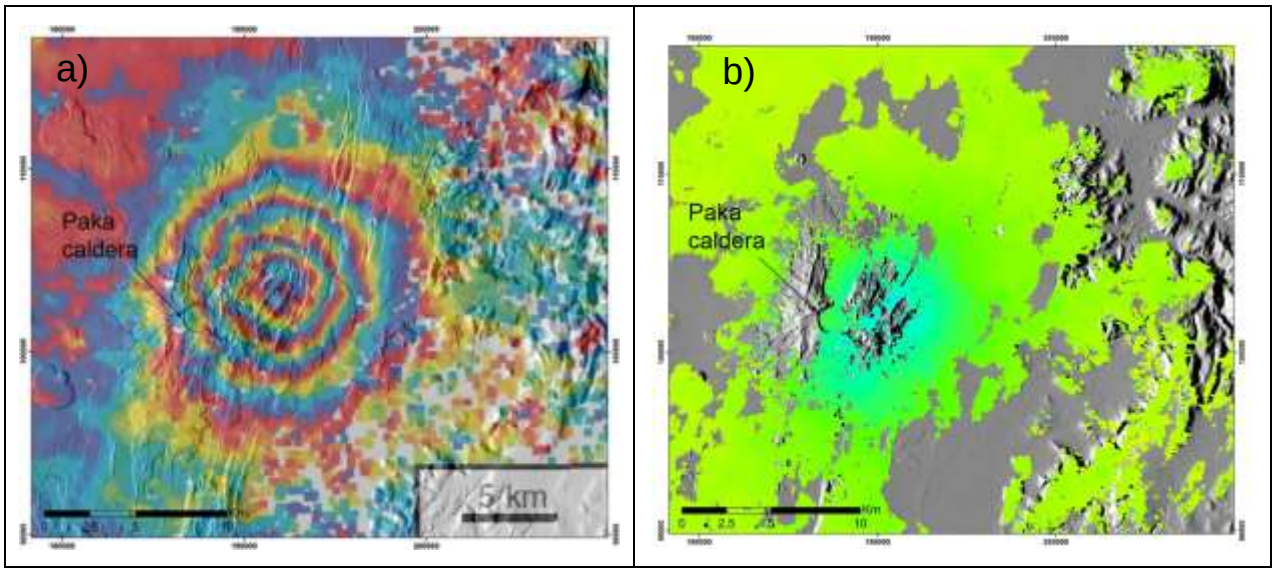

Figure 31: Comparison of two InSAR analysis using Envisat-ASAR data. a) Stack of three interferograms covering period between 2006 and 2007 showing an uplift of 21 cm (Biggs et al. 2009). b) Subset of the surface deformation map of the recent time series analysis for the years 2006 to 2010 showing uplift in the same area. (BGR; Grid: UTM zone 37 N, WGS-84).

The second study performed by Biggs et al. (2013) captures the end of the inflation episode in 2008 using a dataset of the ALOS satellite. Figure 32a shows a stack of four interferograms from January 2007 to July 2008 with ~3 cm of uplift. Figure 32b shows a stack of six interferograms for the period between July 2008 and 2010 where the majority of the area shows no deformation or rather deformation in the range of the accuracy of the measurement and only very little areas of uplift (red colours). This correlates with the analysis of the Envisat-ASAR data performed using the SBAS method in the recent project, where the deformation ends between February 2008 and October 2009 (Figure 29) and no further deformation is recognizable afterwards until the end of the investigation period in October 2010.

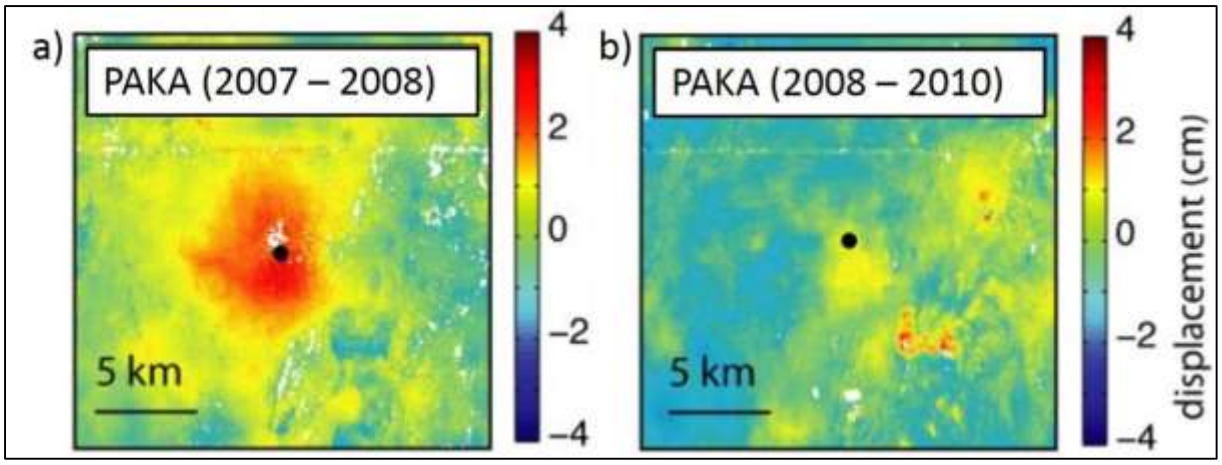

Figure 32: a) The uplift of Paka volcano is consistent with the end of the previously detected inflation episode lasting until July 2008; b) The period following July 2008 shows no deformation for the majority of the area and only very little areas with uplift (modified after Biggs et al., 2013).

Some areas do not show any surface points in the SBAS results of the Envisat-ASAR data. That means no information is available for that specific area. Possible reasons are e.g. the loss of coherence between the acquisition dates due to either a newly grown vegetation cover, an alluvial erosion, or a too strong deformation. At Paka volcano, the parts with no interferometric information occur mostly in areas with an alluvial cover and in the area of the western boundary fault, whereas in areas with solid lava flows the datasets maintain a sufficient coherence over the entire investigation period. A loss of coherence along the faults within the Paka area is not consistent. At some faults, the coherence was lost, at other faults coherence and therefore time series remains consistent. A calculation of areas affected by shadow (as described in chapter 3) showed, that shadow is not the reason for the loss of coherence at the faults. A loss of coherence can also be caused by a strong vertical displacement at a fault in areas with an extremely strong tectonic activity. However, such a displacement would be visible in the field and would have been detected by seismic stations. A search in the International Seismological Centre On-Line Bulletin (www.isc.ac.uk) and the Global CMT Catalog (www.globalcmt.org) for seismic events that could cause a displacement big enough for the loss of coherence yielded no results in the area of Paka volcano for the years 2006 to 2010. Neither did a field survey give sufficient results for strong displacements along faults. In the area of Paka, the loss of coherence is therefore most likely caused by vegetation and alluvial sediments.

3.4.2 Analyses of TerraSAR-X data

The results of the InSAR study based on TerraSAR-X data are shown as a velocity map, an accompanying ESRI shapefile, and a time series plot of five points within the two deformation areas. The Surface Deformation Map shows average annual surface deformation values (Figure 33; attachment 2).

The deformation values are measured in line-of-sight of the satellite sensor. They have been projected into height (vertical) direction under the assumption that the total deformation occurs in a vertical direction (representing uplift or subsidence) and that the horizontal motion component is negligible.

The displacement values are measured relatively to a GCP (Figure 33). The given values can then be assumed to represent absolute deformation values under the assumption that the

reference pixel is stable and not subject to any uplift or subsidence during the time of observation.

It must be taken into account that the average annual velocity values are extrapolated from half a year of acquisition time to 1 year in the graphical display of the surface deformation map. Furthermore, the velocity map gives annual deformation rates. As the surface deformation tends to behave non-linear, the development over time has been investigated considering single points within the deformation areas (Figures 35 and 37).

The overall survey area turns up to remain relatively stable with an average velocity for the majority of pixel of about ~0.4 mm/year. This value is within the theoretical precision of 1-2 mm/year of the method (see chapter 3.3). The measurement characteristics of the survey area are shown in table 8. Nevertheless, two areas show significant surface deformations. Clearly visible is a prominent subsidence bowl on the eastern flank of the Paka volcano (Figure 33; red rectangle) and an area of uplift in the northwestern part of the survey area (Figure 33; blue rectangle).

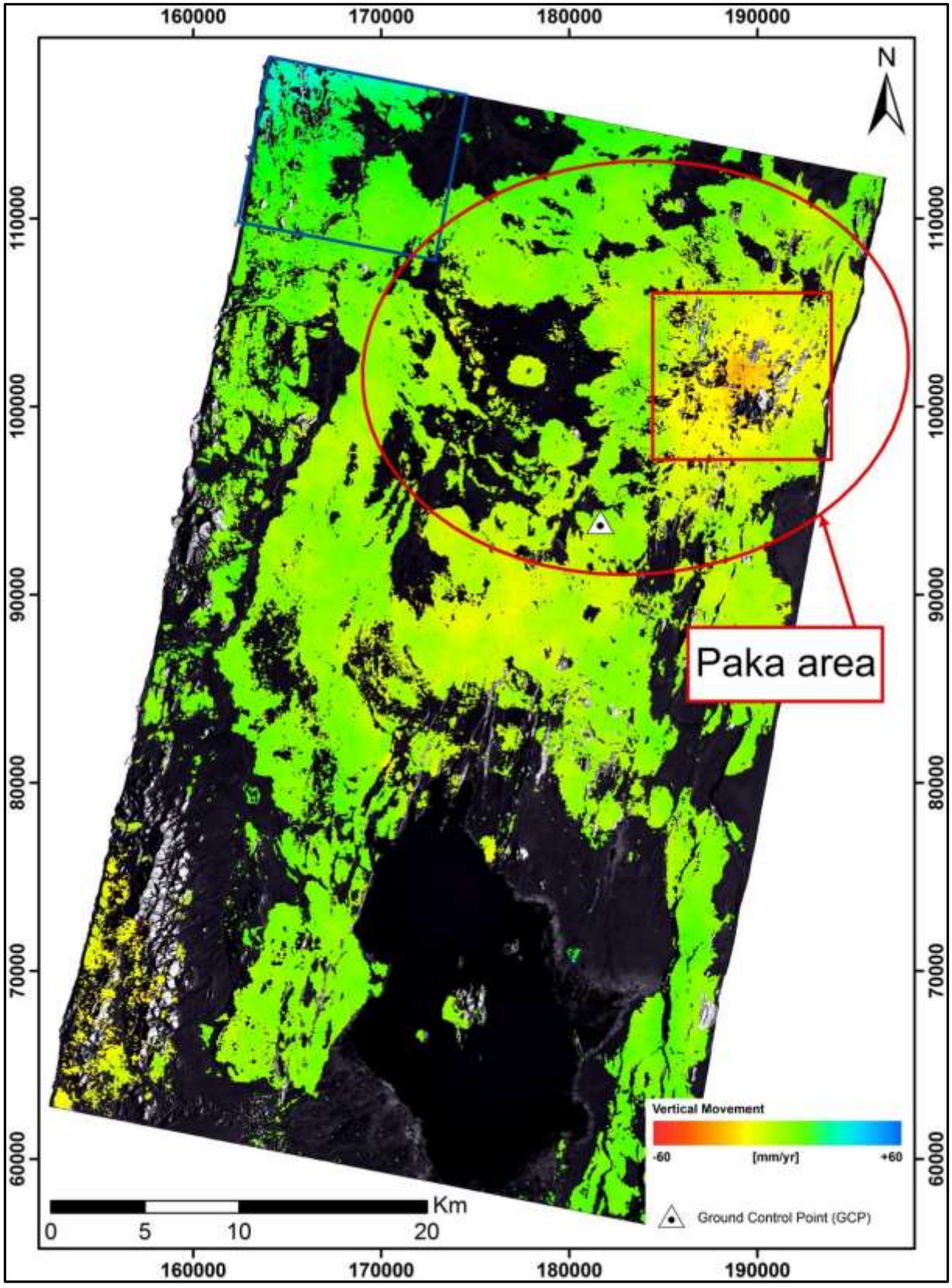

Figure 33: The annual surface deformation map generated form TerraSAR-X data (18/03/2013 – 24/10/2013) superimposed on a geocoded TerraSAR-X amplitude image. The white triangle represents the selected GCP location (UTM zone 37 N, WGS-84; E 181544/ N 93914); the red rectangle shows the area of subsidence, the blue rectangle shows the area of uplift (see figures 34 and 36).

Table 8: Measurement characteristics of the study based on TerraSAR-X data.

Monitoring period	18/03/2013 – 24/10/2013
Ground Control Point (UTM)	N 181543 m / E 93913
Average annual velocity	-0,4 mm/year
Maximum subsidence (annual velocity)	-50 mm/year
Maximum uplift (annual velocity)	40 mm/year
Measurement pixel density	1050 pixel/km²

The subsidence bowl on the eastern flank of the Paka volcano shows a non-linear surface deformation. Five points within the deformation area were selected and plotted in a time series to display the evolution of the deformation over the investigation period (Figures 34 and 35). All five points show almost identical deformation rates. From March to July 2013, the points show a linear subsidence of ~20 mm. From July to August, the points remain nearly stable until uplift starts at the end of August 2013. From the end of August until the end of the investigation period in October 2013, an uplift of ~5 mm is recorded. The chosen points are representative for the area as the velocity values of the points are comparable to the values of the measurement points in their spatial neighbourhood and do not show outstanding deformation values. It is furthermore noticeable, that the centre of deformation does not coincide with the centre of the Paka caldera.

The change of deformation behaviour from subsidence to stability and uplift can be seen as volcanic “breathing”. This kind of volcanic “breathing” is known from other volcanoes as well and has been measured using InSAR before. Biggs et al. (2009) report that four out of ten Kenyan central rift volcanoes showed signs for an alternating inflation and deflation between 1997 and 2008.

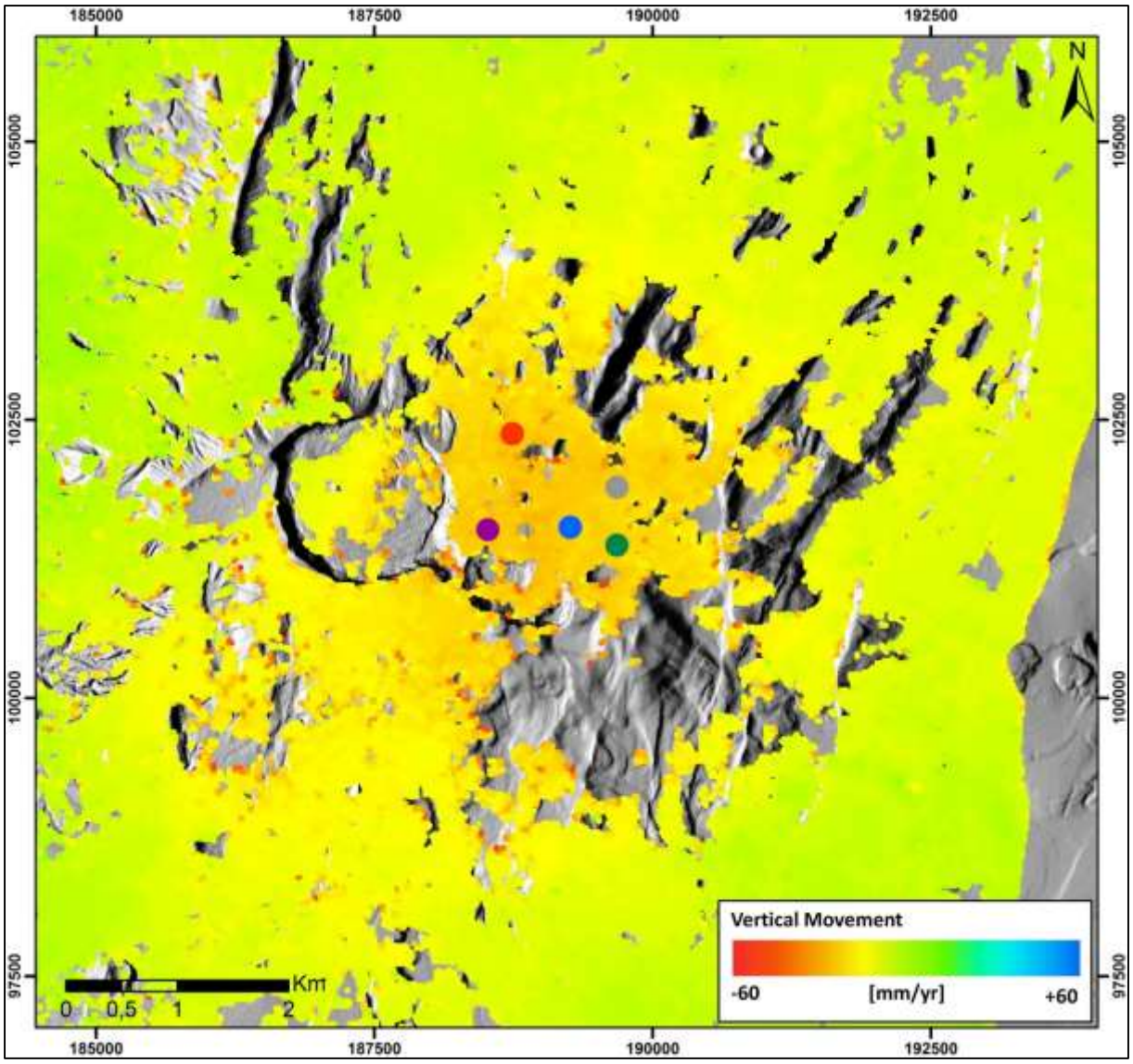

Figure 34: Subset of the surface deformation map (Figure 33; red rectangle) shows a subsidence bowl on the eastern flank of Paka volcano superimposed on the shaded relief map created from the Pléiades satellite data DTM. Coloured dots indicate the locations of the time series plot (see figure 35). Grid: UTM zone 37 N, WGS-84.

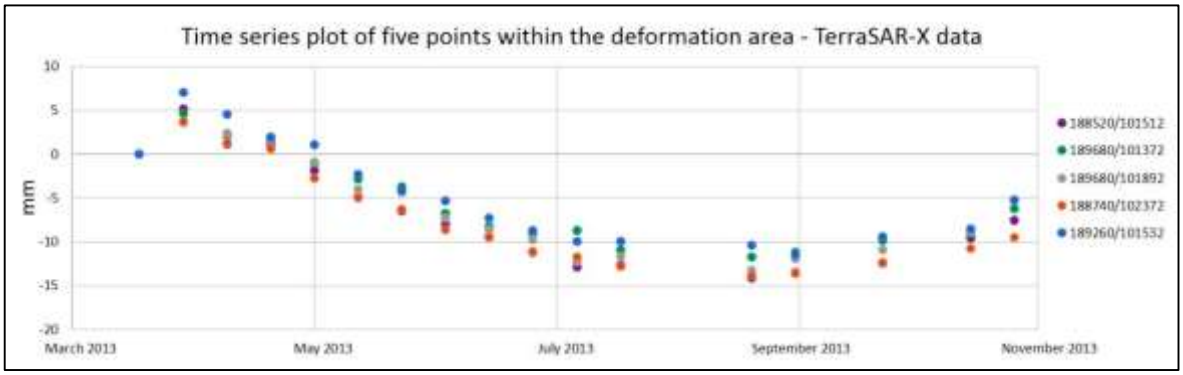

Figure 35: Time series plot of five points within the deformation area on the eastern flank of the Paka caldera. Between March and July 2013, a subsidence of ~20 mm was detected, followed by a short period of stability and uplift of ~5 mm between August and October 2013.

Another area showing deformation is located in the north-west corner of the TerraSAR-X survey area. Again, five points within the deformation area were selected and plotted as a time series to investigate the evolution over time (Figures 36 and 37). The five points show identical deformation characteristics. From March to August 2013, the area is relatively stable whereas from August until the end of the investigation period a distinct uplift of ~20 mm is measurable for all five points. Unfortunately, the entire extent of the uplift area is not recorded due to the boundaries of the TerraSAR-X data footprint. The source of the deformation is unclear as there are no distinct geological feature in this area that could explain the deformation.

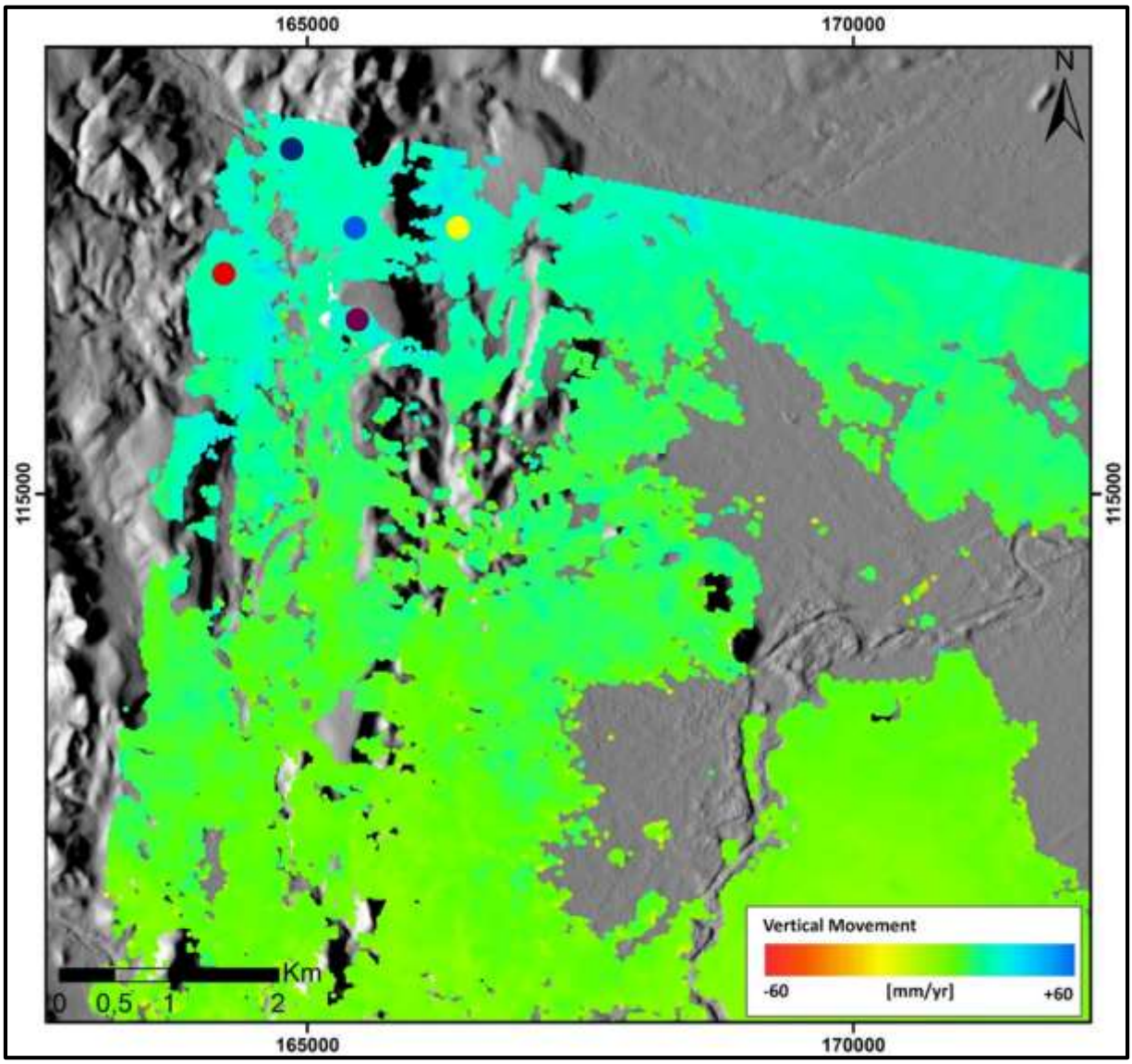

Figure 36: Subset of the surface deformation map (Figure 33; blue rectangle) shows the area of uplift in the northwestern part of the surveyed area superimposed on the shaded relief map created from the TanDEM-X DTM (Pléiades data covers only Paka volcano, not the whole TerraSAR-X survey area). Coloured dots are the locations of the time series plot (Figure 37). Grid: UTM zone 37 N, WGS-84.

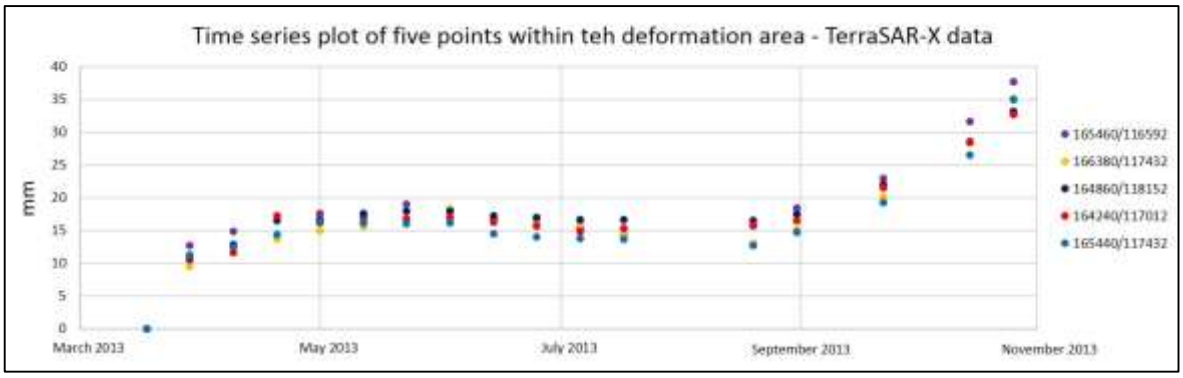

Figure 37: Time series plot of five points within the deformation area in the northwestern part of the study based on TerraSAR-X data. An uplift of ~20 mm between March and June and of ~20 mm between September and October 2013 is recorded.

3.5 Summary and conclusion

Figure 38 displays the different ground coverages of the Envisat-ASAR data study and the TerraSAR-X data study. The Envisat study overlaps the smaller TerraSAR-X study area almost completely. A temporal overlap between both acquisitions does not exist, due to a lack of data availability. The temporal evolution of Paka volcano was therefore analysed and discussed for two separate periods: Envisat for 2006 to 2010 and TerraSAR-X for a six-month period in 2013.

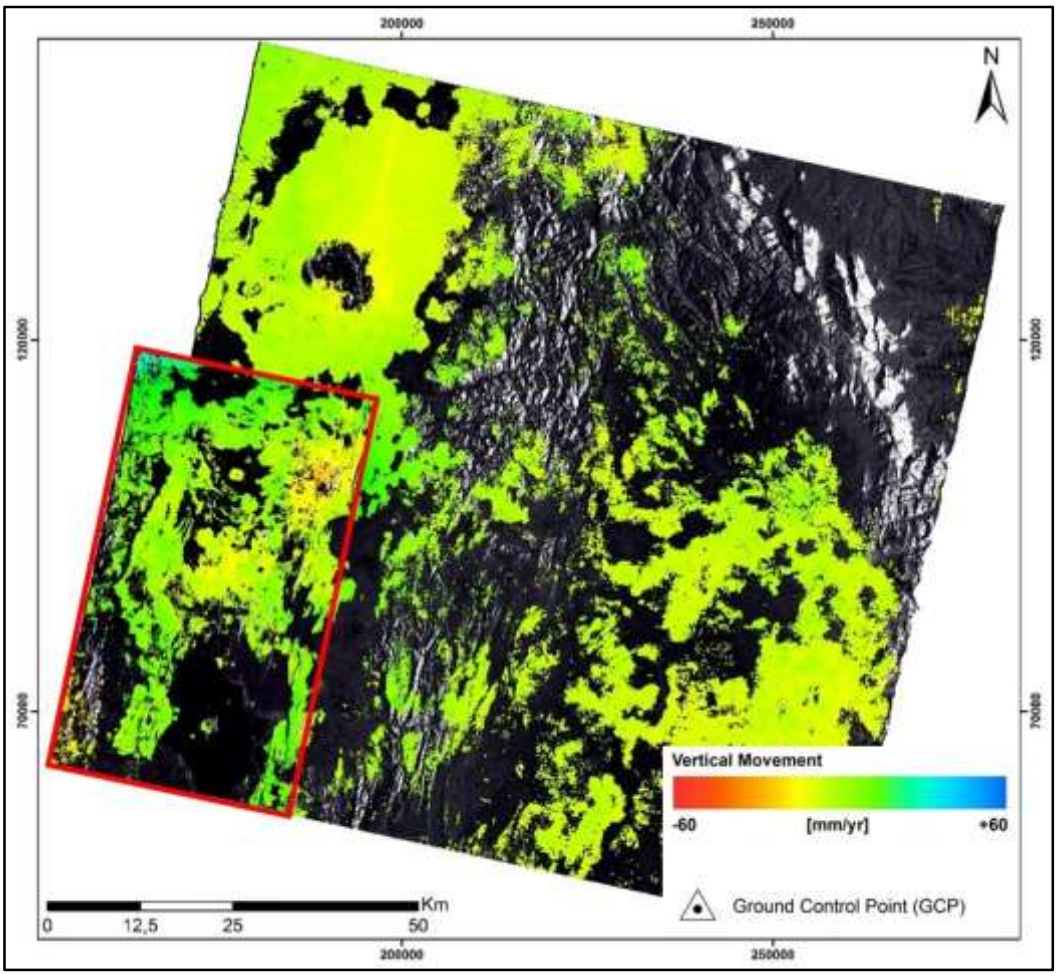

Figure 38: Surface deformation map of Envisat-ASAR data and TerraSAR-X data (red rectangle); Grid: UTM zone 37 N, WGS-84.

The pixel density of the SBAS result from the Envisat-ASAR data varies from the pixel density of the study based on TerraSAR-X data due to the difference of the spatial resolution of the C-band used on-board of the Envisat satellite and the X-band used on-board of the TerraSAR-X satellite. The spatial resolution of the SBAS results for the Envisat-ASAR data and the TerraSAR-X data are 30 m and 20 m, respectively.

Figure 39 shows the subsets of the eastern flank of Paka volcano comparing the surface deformation maps of both studies. Figure 39a shows the uplift recorded using the Envisat-ASAR data, figure 39b shows the subsidence recorded using the TerraSAR-X data. The white dot in the centre of both images indicates the location of two points used for time series plots (Figures 40 and 41) of Envisat and TerraSAR-X data. Highlighted in red are active fumaroles of the Paka area that are known and analysed geochemically by GDC.

Analysing the time series of deformation for a chosen location within both studies the evolution of deformation can be analysed. The slight difference of the coordinates of the location is a result of the different spatial ground resolutions of the two studies. Figure 40 clearly shows that an uplift occurred between 2006 and 2008, whereas the point seems relatively stable between 2008 and 2010. During the period of TerraSAR-X data availability in 2013, subsidence turned into uplift at the end of the analyses (Figure 41). Uplift, stability, subsidence and the start of an uplift deformation in September 2013 represent a high temporal variable deformation signal for the eastern flank of the Paka volcano and shows that the deformation at Paka volcano is episodic. Such a change in the deformation behaviour that can be interpreted as inflation and deflation and is known from other volcanos (Biggs et al. 2009).

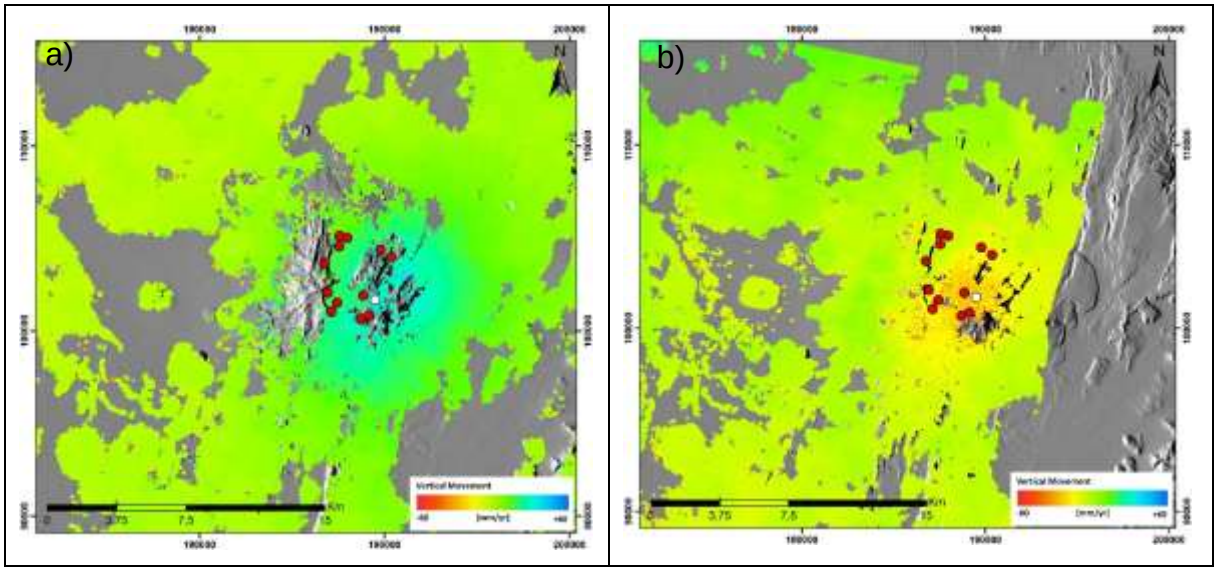

Figure 39: a) The subset of the surface deformation map based on Envisat-ASAR data (2006-2010) shows an uplift of the eastern flank; b) the subset of the surface deformation map based on TerraSAR-X data (2013) shows subsidence on the eastern flank of the Paka volcano. White points indicate the location of two time series analyses (see figures 40 and 41). Red points display locations of active fumaroles within the area of Paka volcano. Grid: UTM zone 37 N, WGS-84.

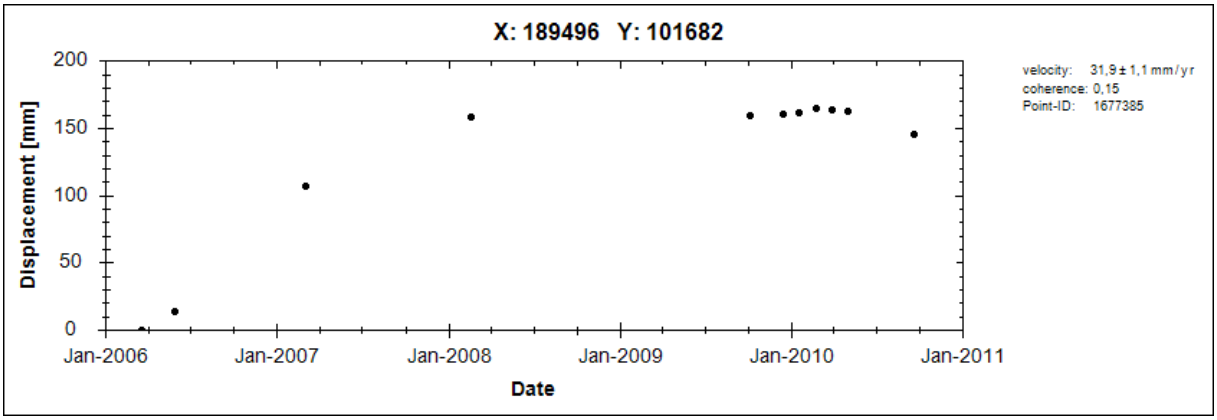

Figure 40: Time series of the deformation for coordinate 186496/ 101682 (Envisat-ASAR data) see figure 39.

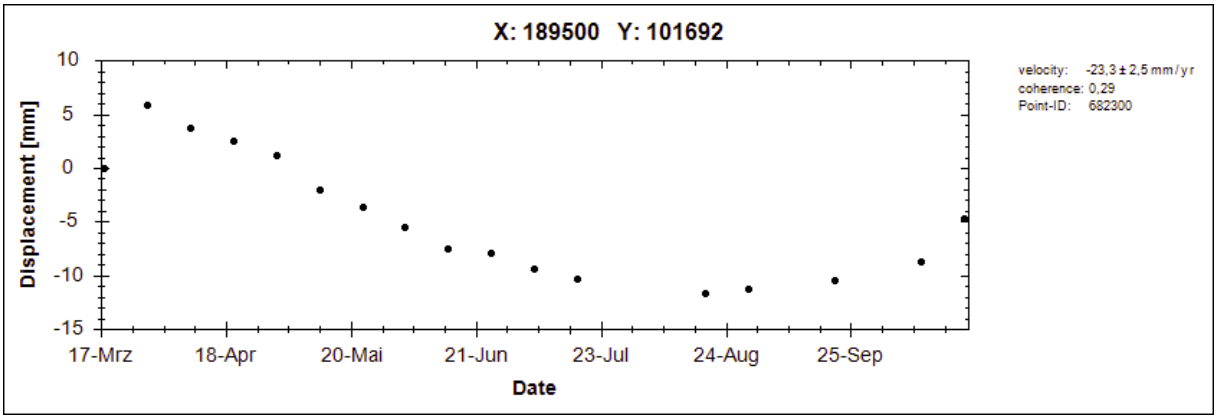

Figure 41: Time series of the deformation (2013) for coordinate 189500/ 101692 (TerraSAR-X data) see figure 39.

Biggs et al. (2009) report that in many settings, a volcanic uplift is unambiguous connected with a magma intrusion in the shallow crust. Other authors suggest that surface displacements may be the result of a migration of hydrothermal fluids (Hutnak et al., 2009). According to Biggs et al. (2009) the geothermal water-flow patterns in the Paka area are fault-controlled and rely strongly on rift basin structures rather than on the proximity to individual volcanoes, although the geothermal heat source is volcanic. The inflation of deeper magmatic sources are recorded to cause dilatation of overlying rocks, opening fractures, increasing permeability, and decreasing pore pressure (Wicks et al. 1998).

At Paka volcano, the areas of deformation are concentrated on the eastern flank for both investigation periods. This area coincides well with the area of fumarolic activity that is reported and surveyed by GDC (Lagat et al. 2013; personal communication with GDC). Twelve fumaroles were sampled and analysed by GDC within the area of deformation (Figure 39). The area of fumarolic activity also coincides with the area with a distinct fault system that can give a pathway for the fumaroles to reach the surface. The existence of the fumarolic activity evidences therefore a recent activity at Paka volcano.

4 Structural analysis

For a structural analyses and a future infrastructural planning of the Paka area a digital terrain model (DTM) with a spatial resolution of 4 m was calculated. The DTM covers an area of ~421 km² and includes all lava flows related to Paka volcano. The area covered by the DTM was chosen in agreement with GDC. The DTM was ordered from Airbus Defence & Space.

4.1 Technical details of DTM generation

For the generation of the DTM two stereo pairs with a spatial resolution of 0.5 m were acquired with the Pléiades sensor in the multispectral (MS) mode on 11/01/2014 and 16/01/2014. Figure 42 shows the two images used for processing. For a first geographical fitting of the stereo pairs, the SRTM DEM was used. The final spatial fixing of the Pléiades stereo images was performed using the Reference3D image product, a global database of ortho-rectified images that provides ground control points as a reference for the Pléiades images.

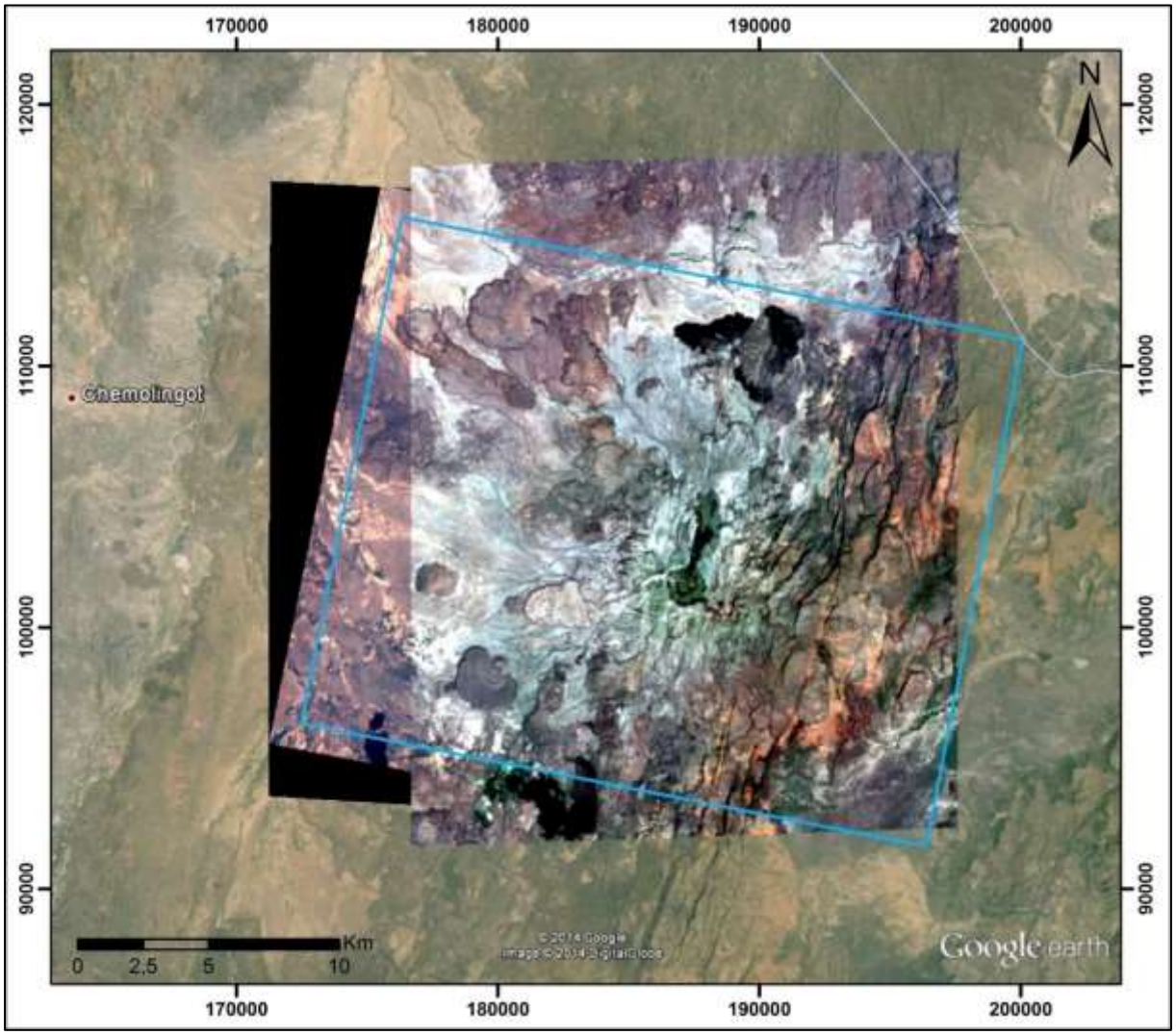

Figure 42: Original DTM extent (blue) and Pléiades stereo images acquired for DTM production on 11/01/2014 and 16/01/2014. Background image Google Earth. Grid: UTM, UTM zone 37 N, WGS-84.

The following parameters summarise the DTM product specification:

- 4 m grid spacing
- ~421 km² coverage
- Horizontal accuracy: RMSE (Root Mean Square Error) 1.9 m
- Vertical accuracy: RMSE 4.8 m
- Spatial reference UTM zone 37 N, WGS-84

The DTM was delivered in GeoTIFF format and ASCII Grid format (Attachments 6 and 7). Additionally, 30 single ortho-image tiles with a resolution of 0.5 m in GeoTIFF format were delivered (Attachment 8).

4.2 Structural analysis based on DTM

Figure 43 shows a shaded relief map generated from the DTM based on Pléiades data. This form of illustration visualises all different structural elements at Paka volcano. Visible are e.g. Paka´s caldera in the centre of the image, NE-SW aligned smaller domes northeast of the caldera, lava flows, and a distinctive fault system on the eastern flank that partly cuts older lava flows.

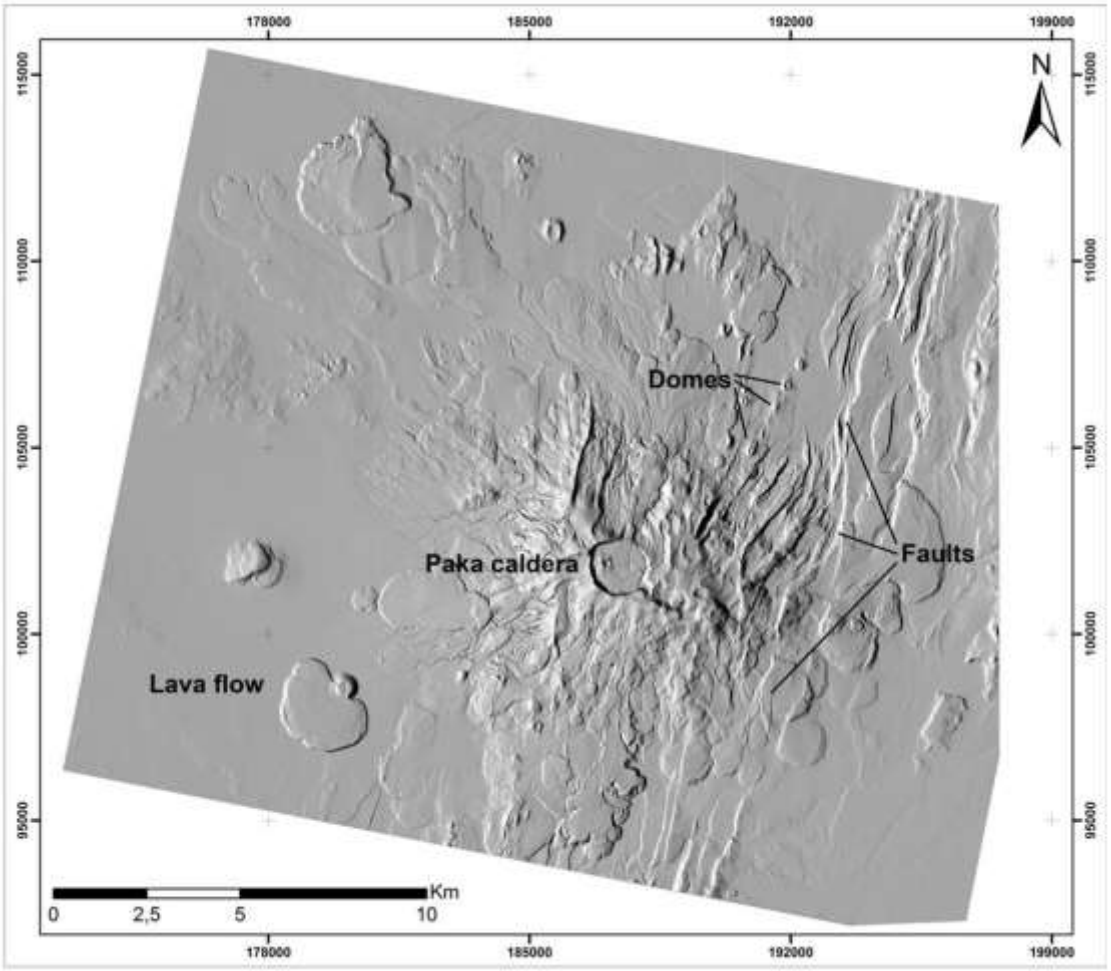

Figure 43: Shaded relief map calculated from the DTM derived from Pléiades satellite data (azimuth 270, incidence angle 45°) displaying different structural elements. Grid: UTM zone 37 N, WGS-84.

A way of displaying the topography of the area is to create a colour coded 3D image (Figure 44). Using this form of illustration a generally plain topography on the western area of Paka volcano is recognizable. Two clearly visible lava flows appear in a brighter blue indicating a topographic raise in that area (Figure 44). On the eastern flank of Paka volcano, the fault system is clearly observable by the abrupt changes of the colour. An abrupt change in colour indicates an abrupt change in height. Furthermore, this illustration displays that the eastern part of Paka volcano has generally a higher elevation than the western part. The rim of Paka´s caldera and a small area east of the caldera built up the highest topographic raise displayed in red colour.

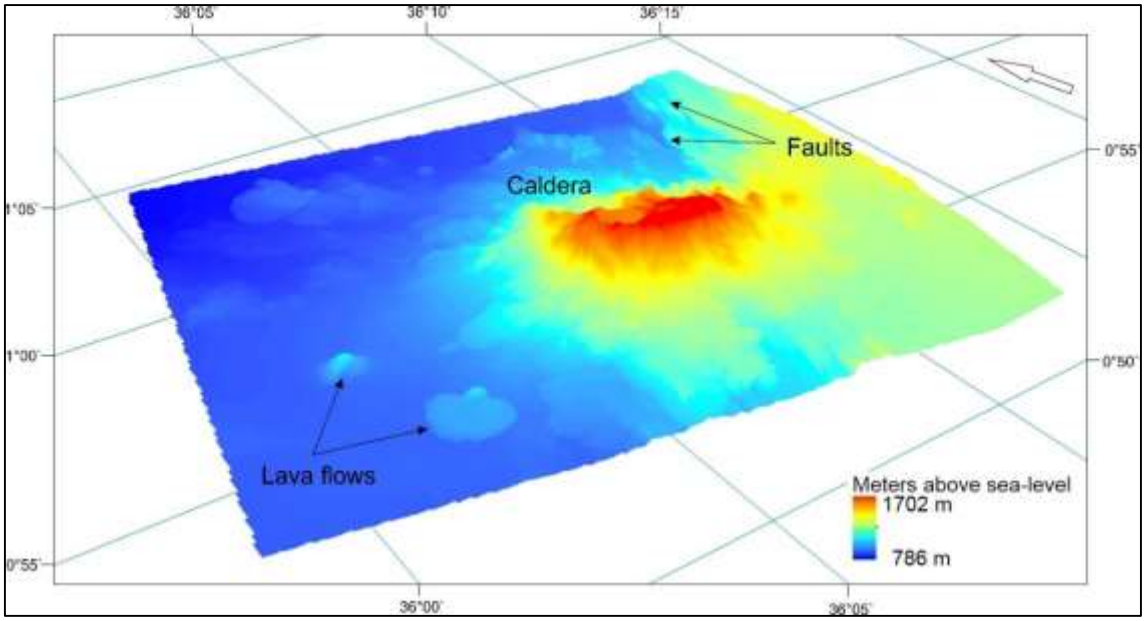

Figure 44: Colour coded 3D image of DTM calculated from Pléiades satellite data.

The Kenyan Rift has a total width of 60 km to 70 km (Figure 45). The inner trough of the northern Kenya Rift has a width of 35 km in the south and 17 km in the north (Dunkley et al. 1993, Frisch & Meschede, 2007). In the south, the trough is an asymmetrical graben structure that is bounded to the west and the east by escarpments that take the form of a symmetrical valley towards the north (Dunkley at al. 1993). Chorowicz (2005) describes the northern Kenya Rift as west-dipping roll-over half-graben, with major border faults running along the western shoulders (Figure 46). Paka volcano, located in the southern part of the northern Kenya Rift, is dominated by a 7.5 km wide zone of normal faulting that shows a right stepping en echelon arrangement across the volcano that developed in an oblique rifting system (Dunkley et al. 1993). Especially the eastern and north-eastern flanks of Paka are intensely faulted by NNE-striking faults that rise to a series of stepped and tilted westerly facing escarpments separating the volcano from the eastern margin of the rift. Such an en echelon arrangement of normal faults is typical in extensional area with horst and graben structures (Frisch & Meschede, 2007). The N-S to NNE-SSW trending faults at Paka volcano correlate with the general N and NNE-trending structures of the East African Rift Valley in northern Kenya (Figure 45) where, in many cases, faults develop parallel to structures of the Precambrian basement (Frisch & Meschede, 2007). NW trending structures are also important and present at Paka. In regions with E-W extension, NW-SE and NE-SW trending rift segments follow the older zones of weakness (Morley, 2010). Figure 45 gives an overview of the regional structures of the Rift Valley between Lake Baringo and Lake Turkana, with the Paka volcano area indicated by a red quadrangle.

Figure 45: Regional structures of the Rift Valley between Lake Baringo and Lake Turkana (Dunkley et al. 1993), the red rectangle indicates the location of Paka volcano.

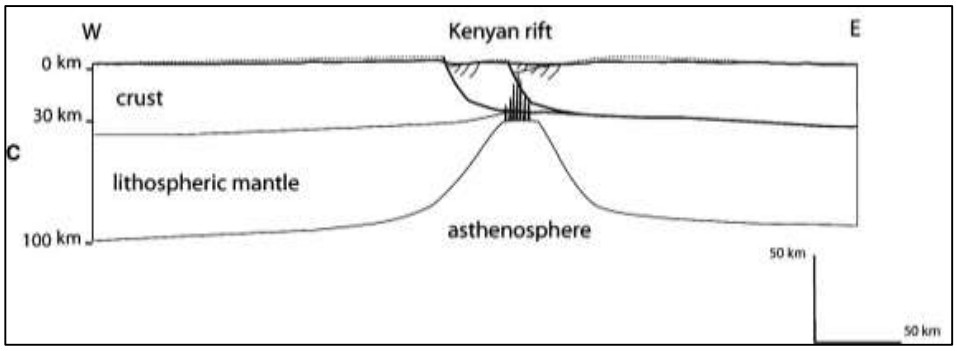

Figure 46: Cross-section of the northern Kenya Rift (modified after Chorowicz, 2005).

At Paka volcano, the rift zone is defined by two faults, the Eastern and Western Boundary faults (Figure 47). The Eastern Boundary fault is a complex fault zone where the cumulative throw is estimated to be in excess of 250 m with minor displacements of the individual faults (Dunkley et al. 1993). The Western Boundary fault is located ~1 km west of the Paka caldera. Westwards of the Western Boundary fault, the area is mainly covered by alluvial sediments with some very well preserved lava flows. No surface manifestations of faults can be recognised in that area. The complex fault zone in the eastern part of Paka volcano (Figure 47) partly cut the existing lava flows. This evidences that the faults developed after the lava flows were erupted and that the area was still tectonically active after the eruption of the lava flows. Defined and mapped as faults (Figure 48; highlighted in red) are structures with a vertical or horizontal displacement recognisable on the satellite image e.g. Landsat TM and the DTM. Directly at Paka caldera, a sinistral movement is visible (Figure 48 and 49). Sinistral movements occur typically in extensional areas where compression exists in the perpendicular direction.

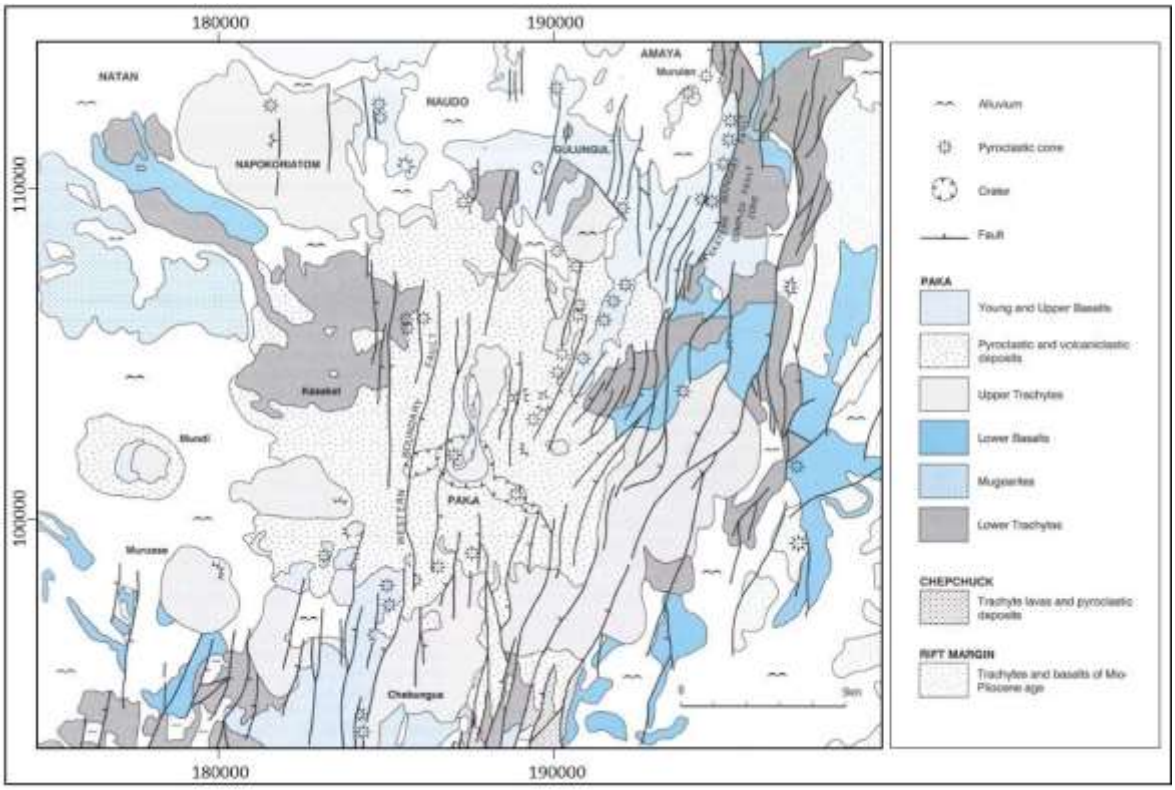

Figure 47: Simplified geological map showing Eastern and Western Boundary fault at Paka volcano (modified after Dunkley et al. 1993).

On the shaded relief map generated from the DTM, further linear structures are recognisable and visualised (Figure 48; highlighted in yellow). In contrary to the faults within the Paka area, these linear structures are well recognisable on the shaded relief map but hardly on the Landsat TM image. No indication of a vertical displacement is recognisable on the shaded relief map or the Landsat TM image for these linear structures. The lineaments generally show a NW-SE trend with only two lineaments in N-S direction. The NW trending lineaments follow the previously described direction of the Precambrian basement structures of the area (Figure 45). The importance of these NW-trending basement structures during the evolution of the Rift has been described by Smith and Mosley (1993). They emphasise “the control exerted by a number of widely spaced ductile-brittle shear zones that segment the rift into its component graben sectors”.

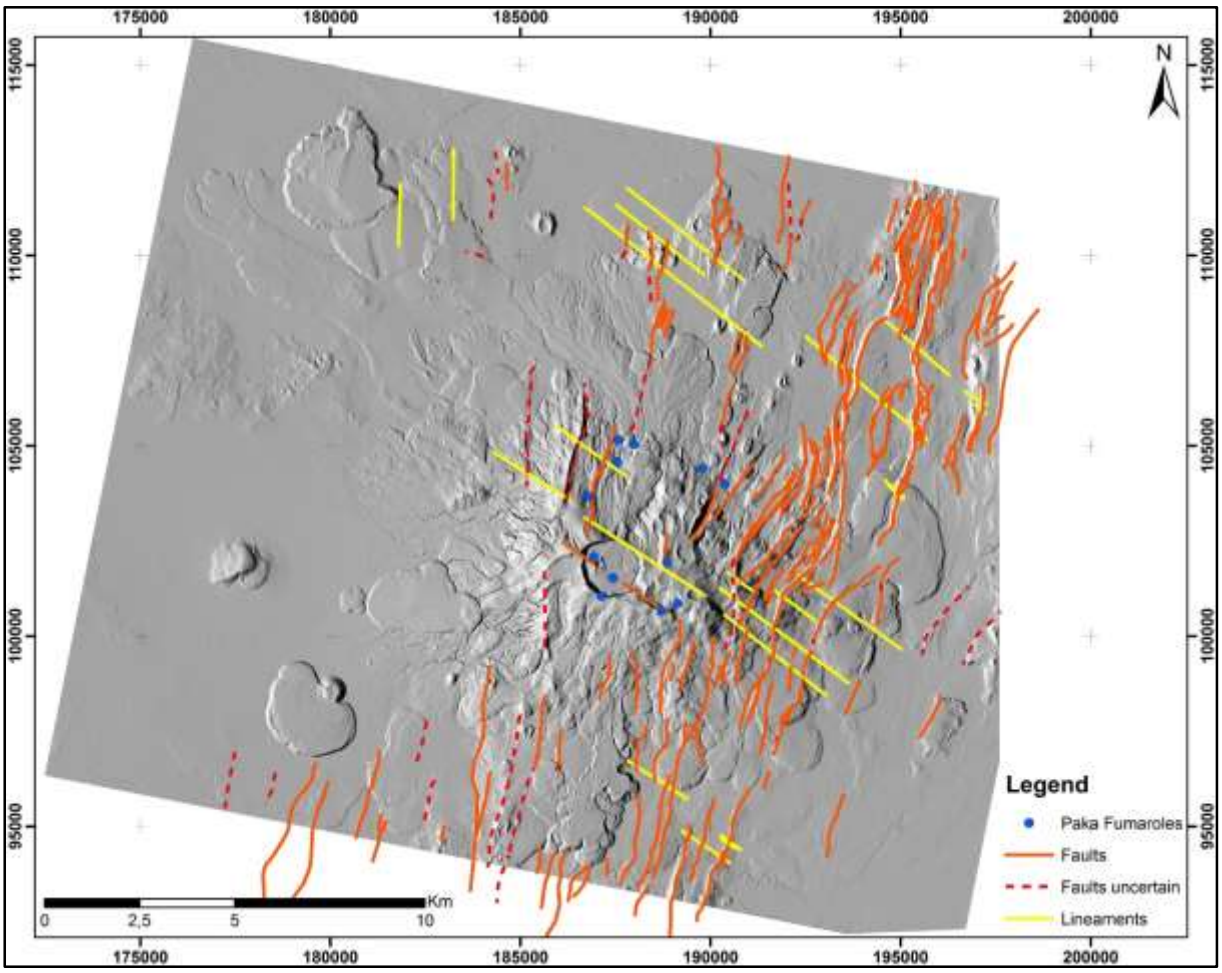

Figure 48: Faults, lineaments and fumaroles superimposed on the shaded relief map of Paka volcano (azimuth 270; incidence angel 45°). Grid: UTM zone 37 N, WGS-84.

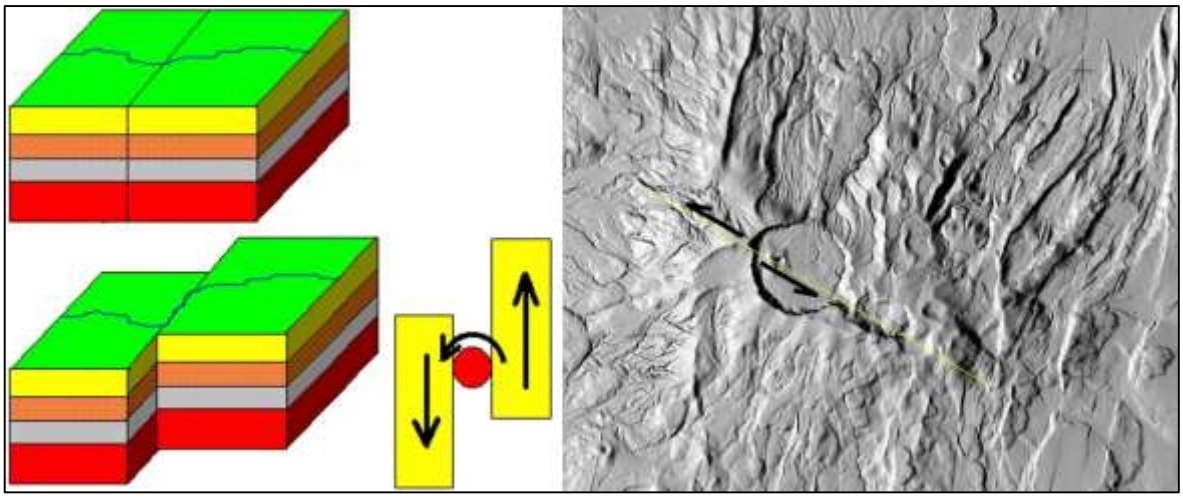

Figure 49: Block diagram of a sinistral movement (www.uwgb.edu) and the corresponding feature at Paka volcano visible on the shaded relief map.

Paka volcano is hydrothermally active. On the eastern and northern area of Paka volcano, geothermal manifestations in the form of fumarolic activity are present. To the west the fumarolic activity is bounded by the Western Boundary fault (see Figure 47 and 48). Twelve fumaroles in the eastern and northern area have been sampled and analysed by GDC (Figure 48). Figure 50 shows two fumaroles on the northern flank of a lava flow that erupted from Paka caldera. The locations of the fumarolic activities are strongly controlled by N to NNE-trending faults and by the caldera structure (Dunkley et al. 1993). Four fumaroles are located close to the Western Boundary fault, four fumaroles are close the sinistral movement at the caldera (Figure 48). This implies that the existing faults give a pathway for the fumaroles to reach the surface. The absence of a fault system and fumarolic activity in the western area might indicate that this area of Paka volcano is tectonically and hydrothermally less active than the eastern and northern regions.

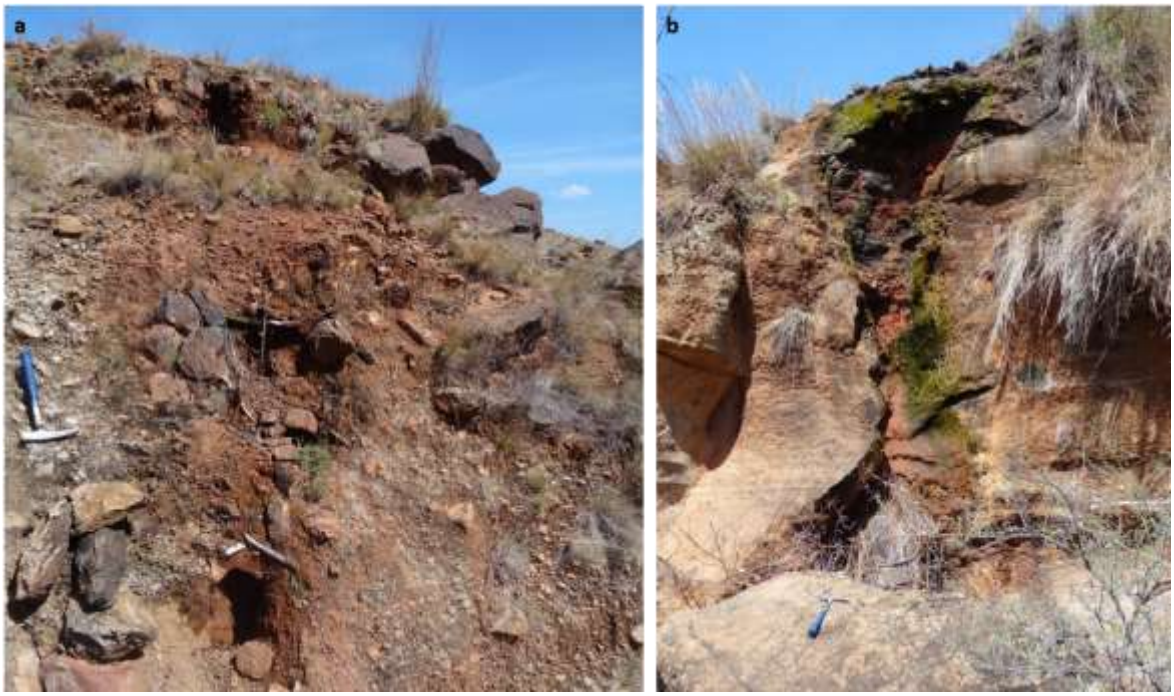

Figure 50: Two fumaroles located at the northern flank of a trachytic lava flow erupting from the Paka caldera (a: E 187878/ N 105328; b: E 187906/ N 105364).

Figure 51 shows a detailed image of the results of the surface deformation study based on TerraSAR-X data. Superimposed are faults and lineaments based on the DTM and the Landsat data, as well as the fumaroles known in that area. No correlation exists between the fault outlines and the InSAR study. No change of the deformation behaviour close to or directly at the faults is recognizable. The deformation rates, yielded from the InSAR data, are consistent on the hanging and lying walls of the faults. This indicates that no vertical deformation took place related to fault activities during the acquisition period of the TerraSAR-X data. The same result was yielded by comparing the Envisat-ASAR data with the fault systems of the area. This indicates that the vertical deformation rates are not linked to the fault activities of the area but to an inflation and deflation of a magma chamber beneath Paka volcano or further hydrothermal sources.

A further structural analysis of Paka volcano and its adjacent areas was performed in the framework of this project during two field trainings that were conducted in cooperation with the University of Potsdam (Chapter 6). During these field trainings the extensional behavior of the region was analyzed on small scale in the field.

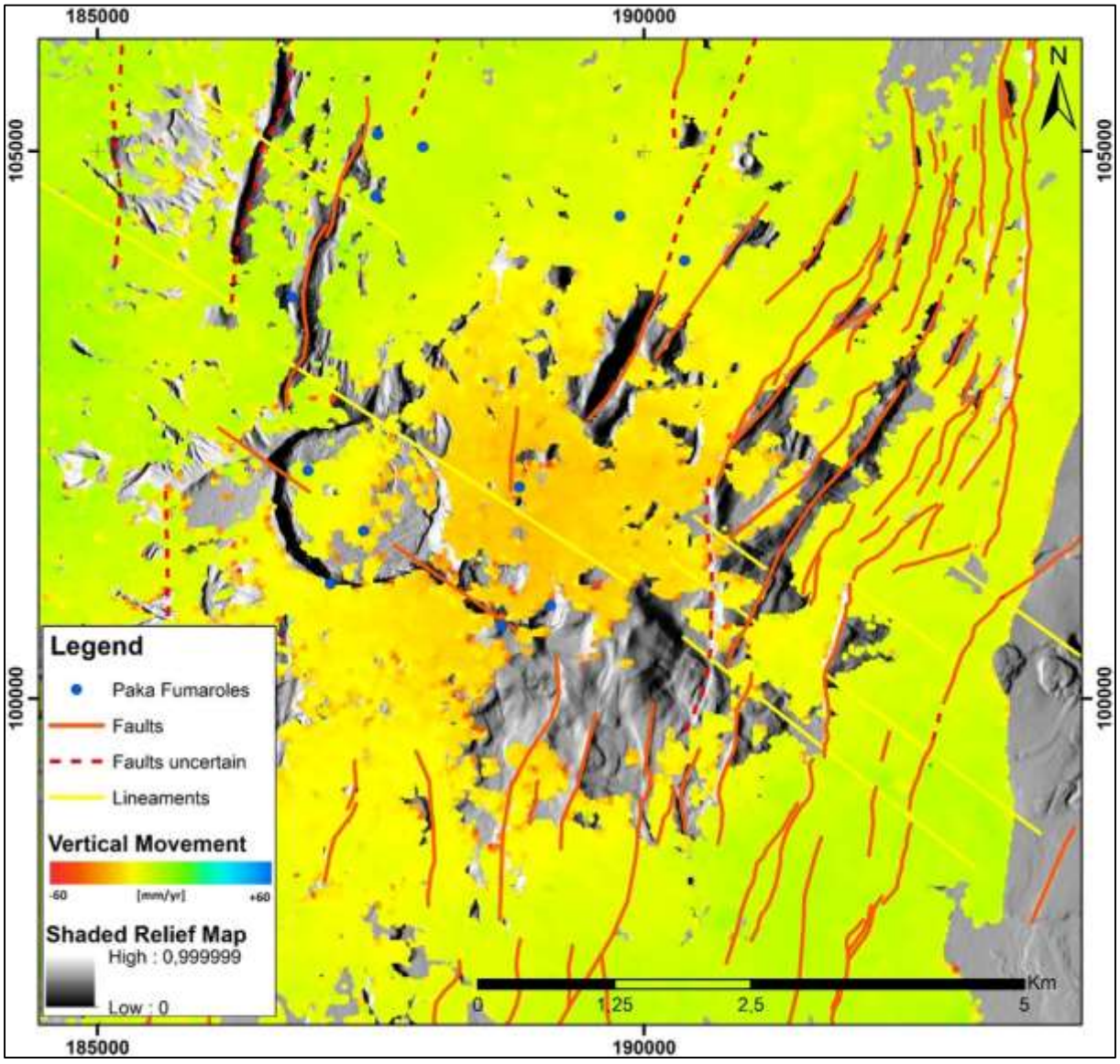

Figure 51: Faults (red), lineaments (yellow), fumaroles (blue) and surface deformation results from TerraSAR-X data plotted on the shaded relief map. Grid: UTM zone 37 N, WGS-84.

5 $^{40}Ar/^{39}Ar$ dating of Paka volcanics

The age dating of Paka volcanics was performed to analyse the eruptive history of the volcanic sequences. Aim of the study is to determine whether there are periods with an intense volcanic activity and if these periods alternate with periods of a minor activity. An important information is the age of the youngest lava flows.

Between February 27 and March 05, 2014 a field campaign to sample 32 different lava flows and pyroclastic deposits at Paka volcano was performed in collaboration of BGR (Andrea Friese, Kai Hahne,), University of Potsdam (Masafumi Sudo), and GDC (Tito Lopeyok, Geoffrey Mibei) (Figures 52 and 53). The fieldwork was excellently organised by GDC.

Figure 52: Team of BGR, GDC and University Potsdam sampling PK 16 (E 183224/ N 103324) on 28/02/2014.

Figure 53: Preparation of a fresh and unaltered rock of sample PK7 (E 194461/ N 102517) suitable for $^{40}Ar/^{39}Ar$ age dating on 27/02/2014.

The 32 sampling localities (PK1 to PK30, M1and M2) were selected based on the different lava flows visible in the Landsat TM image and the existing geological map (Figures 54 and 55). The samples represent the variety of exposed lava flows of the Paka area and all stratigraphic units (Secumius Trachyte, Lower and Upper Trachyte, Mugearite, Lower and Upper Basalt, Pyroclastic Deposits, Trachyte Scoria, and Young Basalts, Table 9).

Table 9: Stratigraphic units of Paka volcano (modified after Dunkley et.al. 1993).

Young Basalts (b^{y})		
Trachytes and mugearites	11±3 ka	INTRA-CALDERA LAVAS
		CALDERA FORMATION
Pyroclastic Deposits (P^{y})	8±4 ka	
Upper Basalts (P^{bu})		
Upper Trachytes (P^{tu})		
Lower Basalts (P^{bl})		
Lower Trachytes (P^{tl})	219±4 ka	SHIELD FORMATION
	390±6 ka	
Mugearites		

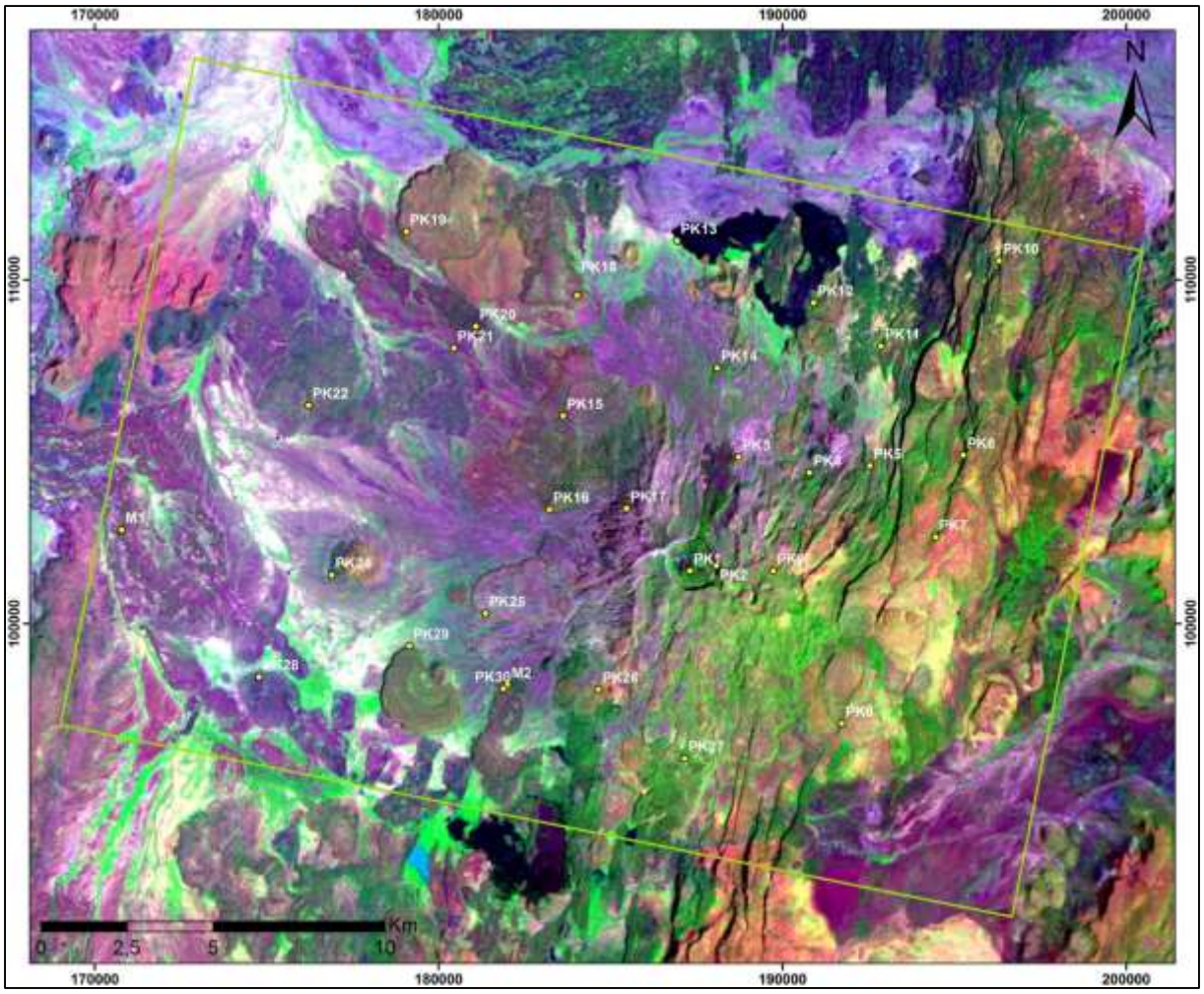

Figure 54: 32 sampling locations superimposed on the Landsat TM image, acquisition date 30/01/2010 (bands 7,4,1 RGB). Yellow dots indicate the locations of samples PK1 to PK30, M1 and M2. The green rectangle indicates the spatial extent of all Paka related lava flows. Grid: UTM zone 37 N, WGS-84.

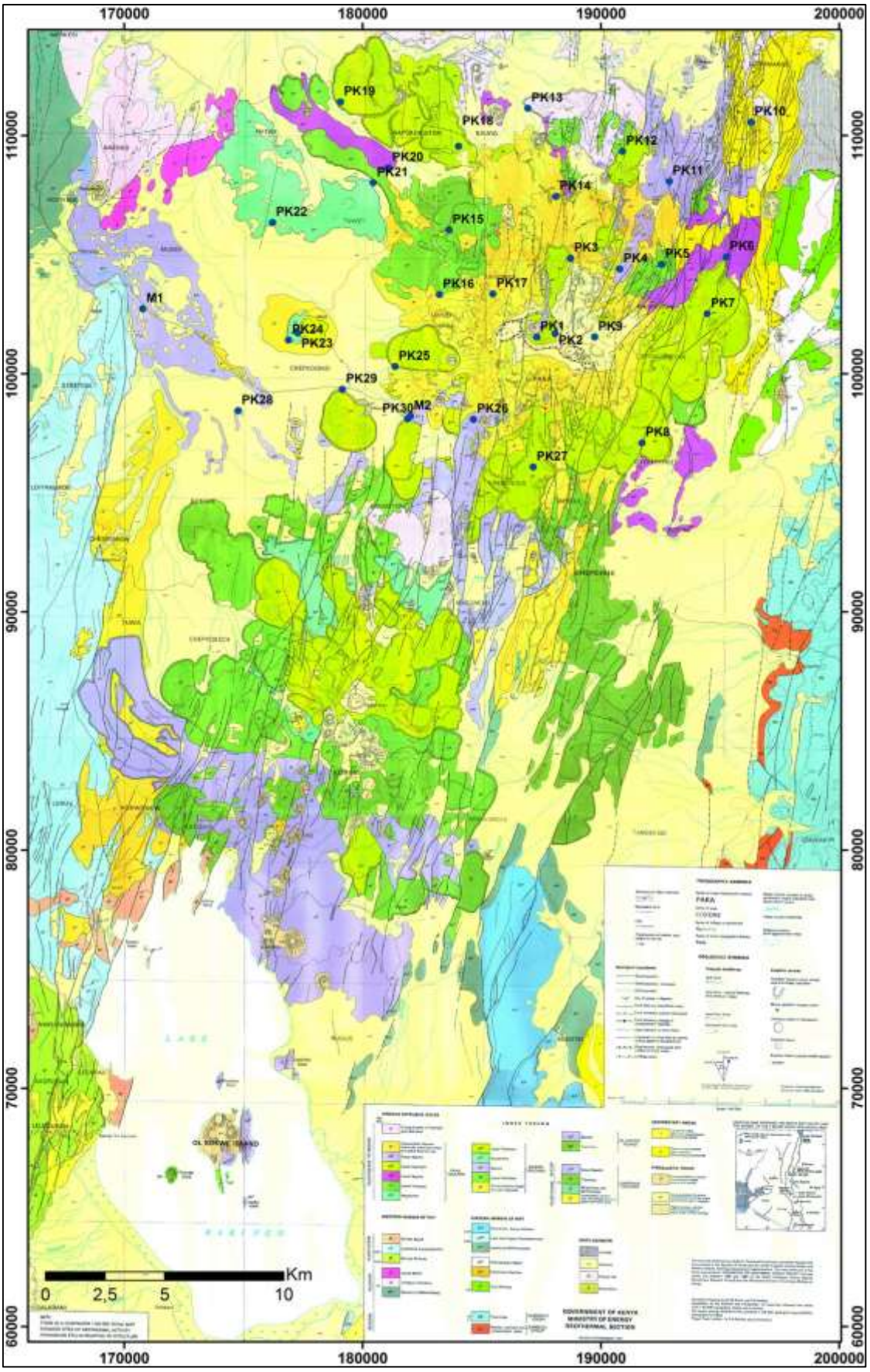

Figure 55: 32 sampling locations superimposed on the geological map published by the British Geological Survey (modified after Dunkley et. al. 1993). Grid: UTM zone 37 N, WGS-84.

5.1 Methodology

The age dating was assigned to the University of Potsdam and performed by Masafumi Sudo.

5.1.1 Preparation of $^{40}Ar/^{39}Ar$ dating

For the age dating analysis fresh, massive lava samples were collected, as fresh rocks are expected to have the least risk of radiogenic ^{40}Ar loss by alteration. Furthermore, massive, vesicle-free rocks and rocks with a low glass content are expected to contain low amounts of atmospheric ^{40}Ar.

For the age dating, the samples were prepared as described in the following chapter. 30 to 80 grams of each sample were crushed and sieved to size fractions of 0.93 – 0.47 mm and 0.47 – 0.26 mm. The proper grain size (0.93 – 0.47 mm or 0.047 – 0.26 mm) was chosen considering the sizes of the phenocrysts within the sample. For samples with an aphyric texture, smaller grain sizes had to be separated. Subsequently, the groundmass was concentrated by the removal of the phenocrysts by magnetic separation with a hand magnet and the Frantz isodynamic separator. Afterwards, the samples were soaked in a 10% HCl solution to remove secondary minerals.

Furthermore, a few samples exhibited a well-developed porphyritic texture. The separated phenocrysts were not used for the dating due to the potential possibility of excess, mantle-derived ^{40}Ar from higher $^{40}Ar/^{36}Ar$ ratios than the common atmospheric value expected within the phenocrysts of volcanic rocks.

5.1.2 Technical set-up and procedure of age dating

The geochronology laboratory for Ar isotopic analyses of the University of Potsdam consists of three components:

1) A new Wave Gantry Dual Wave laser ablation system with a 50 W CO_2 laser (wavelength 10.6 micrometer) for heating the samples and extracting the sample gases;
2) An ultra-high vacuum purification line equipped with SAES getters and the cold trap used at the frozen temperature of ethanol;
3) A high-sensitivity Micromass 5400 noble gas mass spectrometer equipped with an electron multiplier, which conducts pulse-counting analysis.

The neutron activation for the $^{40}Ar/^{39}Ar$ analyses was performed at the Oregon State TRIGA Reactor (OSTR) from the Radiation Center of Oregon State University, USA. The samples, together with a primary standard (sanidine of the Fish Canyon Tuff), a secondary standard (sanidine of the Alder Creek Rhyolite), and crystals of K_2SO_4 and CaF_2 for the determination of correction factors, were wrapped in commercial-grade Al foil and put into 99.999 % pure Al sample containers (22.7 mm diameter and 101.5 mm height). The Al sample containers were finally wrapped in Cadmium foil to cut off the thermal neutron flux and to reduce unnecessary nuclear reactions. The irradiation lasted 4 hours with a fast neutron flux of 2.5×10^{13} n/cm^2/s. The following cooling period of the samples lasted two weeks. After these two weeks, the radioactivity of the samples was low enough to be sent back to the University of Potsdam for further treatment.

The neutron-flux correction values (J) required to calculate the sample ages were determined by Ar-Ar analysis of the primary standard (Fish Canyon Tuff sanidine FC3S (Uto et al., 1997; Ishizuka, 1998; Lanphere and Baadsgaard, 2001) using an age of 27.5 Ma for the FC3S. Factors to correct for interferences due to Ar isotopes produced from K and Ca during neutron

activation were determined from crystals of K_2SO_4 and CaF_2 irradiated together with the samples.

The error associated with the J values was evaluated from the sanidine of the Fish Canyon Tuff. The error obtained by curve fitting the J values among the different locations of the Fish Canyon Tuff was almost negligible, but was estimated as 0.4% (1 standard deviation) from J values obtained from 4 sanidine grains at identical location in the Al container. The error accompanying each J value was therefore fixed at 0.4% for measurements made at the OSTR reactor.

The Paka volcano samples were analysed using the system of the University of Potsdam mentioned above by a stepwise heating using a CO_2 laser to detect and remove steps of partial Ar loss at the sample surface or the involvement of excess ^{40}Ar. The age calculation and error estimation follow the principles outlined by Uto et al. (1997). Normal and inverse isochron ages were calculated both with following the method of York (1969).

In the present study, the sanidines of the Alder Creek Rhyolite (Turrin, 1994) and the Fish Canyon Tuff were measured together with the Paka samples to confirm the accuracy of the system. Two single-grain total fusion analyses were performed at the University of Potsdam obtaining statistically indistinguishable ages of 1.140 ± 0.007 Ma and 1.148 ± 0.009 Ma, respectively, calibrated against the age of 27.5 Ma of the sanidine of the Fish Canyon Tuff. The yielded ages for the sanidine of the Alder Creek Rhyolite are consistent with recent age determinations of the sanidine of the Alder Creek of 1.16 ± 0.02 Ma and 1.15 ± 0.02 Ma calibrated against the age of 27.84 Ma of the sanidine of the Fish Canyon Tuff (Schmitt et al. 2003).

5.1.3 Criteria concerning plateau steps and $^{40}Ar/^{39}Ar$ ages

The “plateau ages” (Attachment 9) were obtained from the weighted average of “plateau” steps in stepwise-heating age-spectra diagrams according to the following criteria defined by Fleck et al. (1977):

1) Two ages of the contiguous two steps in the “plateau” agree within the 2 sigma error excluding the J value error;
2) The total fraction of the “plateau” covers more than 50% of the total amount of analysed ^{39}Ar;
3) One “plateau” step has more than 3% of the total amount of the analysed ^{39}Ar.

To estimate best reasonable “plateau” ages for the young ages of the Paka samples following the 4 additional criteria were applied:

4) Two ages at both ends of the “plateau” agree within the 2 sigma error range;
5) The last step was not considered in the “plateau age” when the central value of the last step is beyond the 2 sigma range of the weighted average age of the remaining plateau steps;
6) For ages older than 0.1 Ma, the error of the “plateau” step is less than 50%;
7) For ages of 0.1 Ma or younger, the error of the “plateau” step is less than 1 sigma error.

However, sample M1 (Upper Basalt Member) fails criterion 6 as its error is greater than 50% 1 sigma in all steps. Therefore, the latter condition were not applied to estimate a “plateau” step for this sample.

The final age of each sample was obtained by comparing plateau and isochron ages. All age spectra, normal isochron and inverse isochron plots of $^{40}Ar/^{39}Ar$ analyses are shown in attachment 9. All data obtained by the stepwise heating are shown in attachment 10. Inverse isochron ages are generally more reliable than normal isochron ages because of the use of

more precise $^{39}Ar/^{40}Ar$ ratios rather than $^{39}Ar/^{36}Ar$ ratios. In the present study, the isochron age was represented by the inverse isochron age for comparison reasons. For those samples, where the initial $^{40}Ar/^{36}Ar$ ratio of the isochron agreed with the atmospheric value within the 2 sigma error range, the age with the smaller absolute error was chosen between the plateau age and the isochron age. In cases where the initial $^{40}Ar/^{36}Ar$ ratio of the isochron was beyond that range, the isochron age calculated from all steps was chosen for that sample. If no plateau age could be defined (no plateau), the isochron age calculated form all steps was chosen for the sample.

5.2 Results of $^{40}Ar/^{39}Ar$ dating

Meaningful ages were obtained for 30 samples by a careful evaluation of plateau or isochron ages. Two samples yielded negative ages and are therefore meaningless.

The results of the age dating suggest a protracted volcanic activity during the past ~ 0.6 Ma. Three phases of pronounced volcanic activities are recognised.

(1) between 0.428 and 0.372 Ma;
(2) between 0.160 and 0.126 Ma; and
(3) between 0.039 and 0.012 Ma.

It is noticeable, that the intervals of pronounced activity shortens from the 1st to the 3rd phase. Seven lava flows erupted during the 56.000-year time span of the 1st phase. The 2nd phase lasted 34.000 years including five eruptions and the 3rd phase lasted 27.000 years including six eruptions. The time span of the intervals between the pronounced phases shorten as well towards present. During the intervals with an intense activity, basaltic and trachytic lava flows were repeatedly erupted (Table 10, Figure 56). The same was noticeable for the periods with a less intense activity.

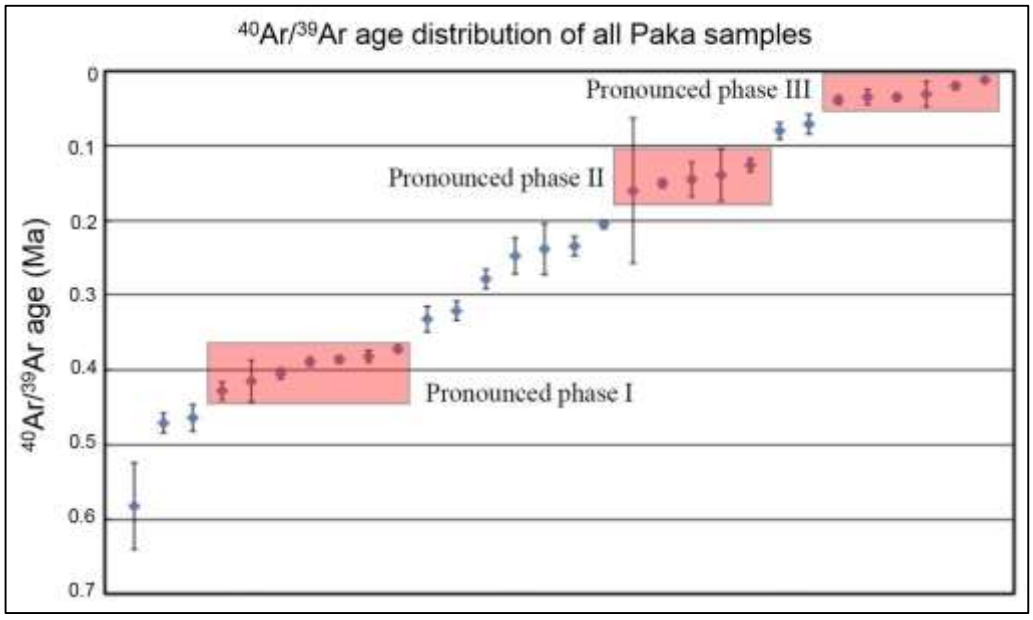

Figure 56: Distribution of $^{40}Ar/^{39}Ar$ ages of Paka volcano samples showing three periods with pronounced volcanic activities.

The age results are given in table 10. The results are ordered according to the geological units of the geological map published by Dunkley et al. (1993). Additionally, the results are superimposed on the geological map (Figure 57 and attachment 11) and on the shaded relief map generated from the DTM of the Pléiades satellite data (Figure 58 and attachment 12).

Table 10: Age dating results ordered according to the geological units of the geological map published by Dunkley et al. (1993). Coordinates are in UTM zone 37 N, WGS-84.

Unit Name	Sample ID	$^{40}Ar/^{39}Ar$ ages (Ma)	Age derived from	Isochron age width	Localities Easting	Northing	Elevation (m)
Young Basalt	PK-13	0.145±0.023	Plateau age		186937.80	111141.09	871.42
Upper Basalt	PK-1	-0.037±0.007	Inverse isochron age	all steps	187309.19	101542.31	1483.37
	PK-4	0.238±0.034	Inverse isochron age	all steps	190790.72	104394.65	1129.07
	PK-11	0.372±0.005	Plateau age		192865.34	108075.97	993.71
	PK-26	0.150±0.006	Plateau age		184649.35	98087.41	1148.85
	PK-28	-0.386±0.047	Inverse isochron age	all steps	174778.32	98449.24	889.10
	PK-M1	0.160±0.097	Plateau age		170780.00	102731.00	874.00
	PK-M2	0.247±0.024	Plateau age		182006.00	98225.00	968.0
Trachyte Scoria and Pumice Lapilli Deposits	PK-9	0.332±0.017	Inverse isochron age	all steps	189736.48	101538.08	1518.24
Late Pyroclastic Deposits	PK-17	0.031±0.017	Inverse isochron age	plateau steps	185465.91	103352.93	1289.43
Upper Trachytes	PK-2	0.035±0.005	Inverse isochron age	all steps	188078.60	101687.45	1473.13
	PK-3	0.020±0.005	Inverse isochron age	plateau steps	188726.09	104848.14	1180.34
	PK-7	0.278±0.013	Plateau age		194461.01	102517.74	1285.86
	PK-8	0.205±0.006	Plateau age		191724.36	97096.95	1227.67
	PK-12	0.012±0.003	Inverse isochron age	plateau steps	190906.60	109337.24	986.36
	PK-14	0.080±0.011	Plateau age		188109.54	107443.26	1027.3
	PK-18	0.382±0.008	Plateau age		184029.92	109549.78	885.44
	PK-19	0.415±0.028	Plateau age		179068.21	111410.80	857.25
	PK-23	0.428±0.012	Plateau age		177285.68	101713.89	977.73
	PK-25	0.035±0.010	Plateau age		181364.78	100300.67	998.04
	PK-27	0.071±0.013	Plateau age		187155.19	96084.02	1171.32
	PK-29	0.039±0.006	Plateau age		179151.69	99349.99	910.74
	PK-30	0.126±0.009	Plateau age		181885.98	98105.25	964.08
Lower Basalts	PK-6	0.389±0.006	Plateau age		195261.76	104907.21	1114.47
	PK-20	0.582±0.058	Inverse isochron age	all steps	181086.59	108650.69	869.69
Mugearites	PK-22	0.471±0.013	Plateau age		176220.72	106349.89	884.65
	PK-24	0.464±0.018	Inverse isochron age	all steps	176889.50	101416.61	914.77
Lower Trachytes	PK-5	0.234±0.013	Plateau age		192546.07	104595.20	1038.55
	PK-15	0.139±0.035	Plateau age		183622.71	106043.19	966.76
	PK-16	0.386±0.005	Plateau age		183224.46	103324.41	1032.39
	PK-21	0.321±0.013	Plateau age		180448.06	108016.32	871.45
Secumius Trachyte	PK-10	0.405±0.007	Plateau age		196303.69	110560.72	1052.47

Error values indicate 1 sigma error.

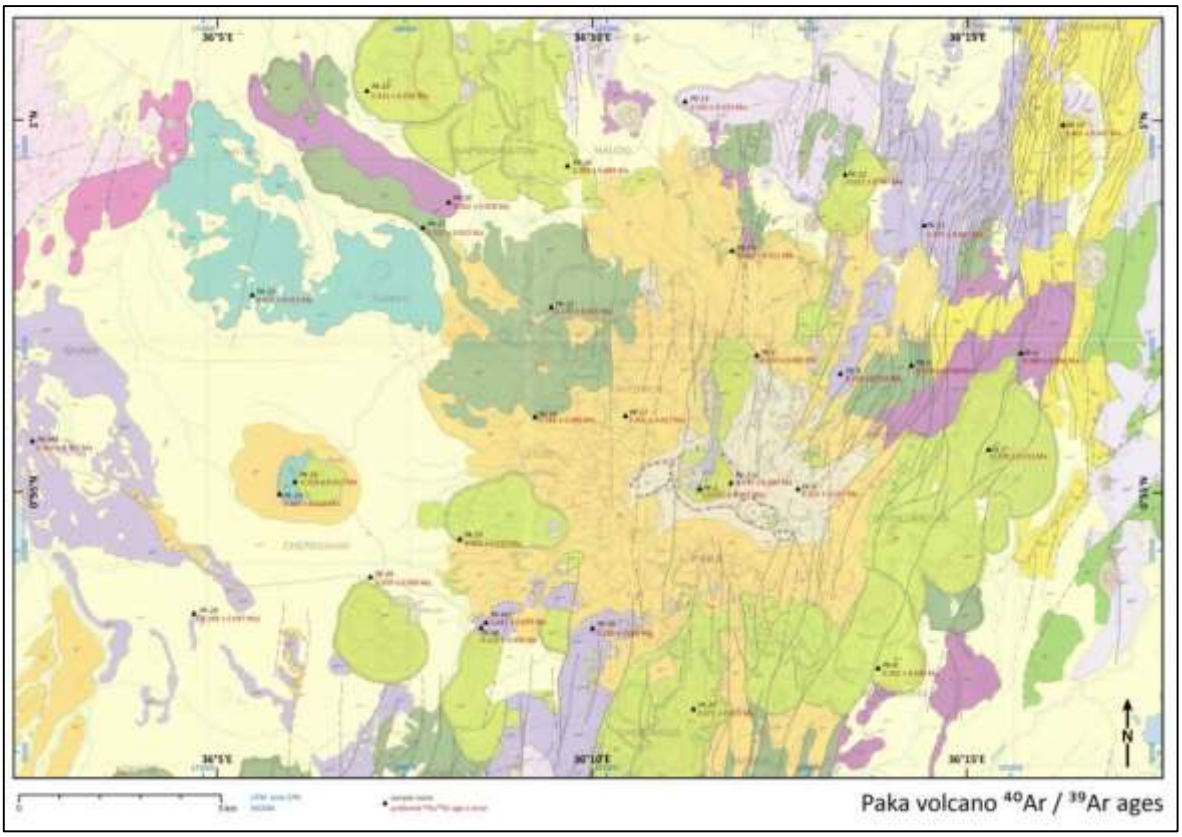

Figure 57: Age dating results superimposed on the geological map published by Dunkley et al. (1993). Grid: UTM zone 37 N, WGS-84. For taller view see attachment 11.

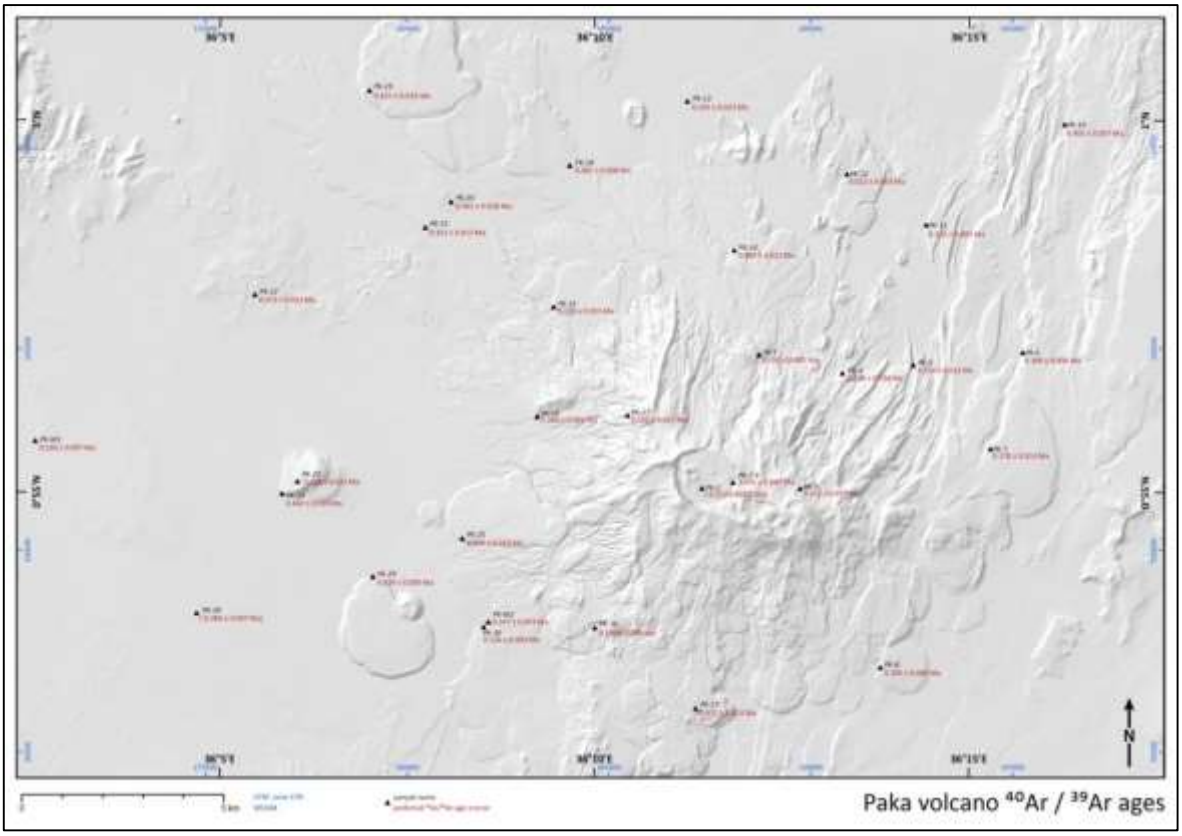

Figure 58: Age dating results superimposed on the shaded relief map created from DTM of Pléiades satellite data. Grid: UTM zone 37 N, WGS-84. For taller view see attachment 12.

Figure 59 shows a Landsat TM image of the western flank of Paka volcano. An analysis of the relative ages of lava flows based solely on the Landsat image is only possible for directly neighbouring flows. In the case of lava flows A and B in Figure 59 it can clearly be recognised that lava flow B overlies lava flow A. This observation is supported by analysing the shaded relief map generated from the DTM (Figure 60) and was finally confirmed by the age dating campaign where for lava flow A an age of 0.464±0.018 Ma and for lava flow B an age of 0.428±0.012 Ma was yielded. In the case of lava flows C and D it can be recognized that lava flow C is highly weathered compared to lava flow D with a still well preserved outline of the flow (Figure 59). On the shaded relief map, the distinct outline of lava flow D is clearly visible as well as the higher topographic elevation (Figure 60). That indicates a younger age for lava flow D compared to lava flow C. This observation is also confirmed by the age dating of both lava flows where for lava flow C an age of 0.247±0.024 Ma and for lava flow D an age of 0.126±0.009 Ma was yielded. For lava flows that are separated by alluvial sediments a determination of the relative age of the lava flows is not possible.

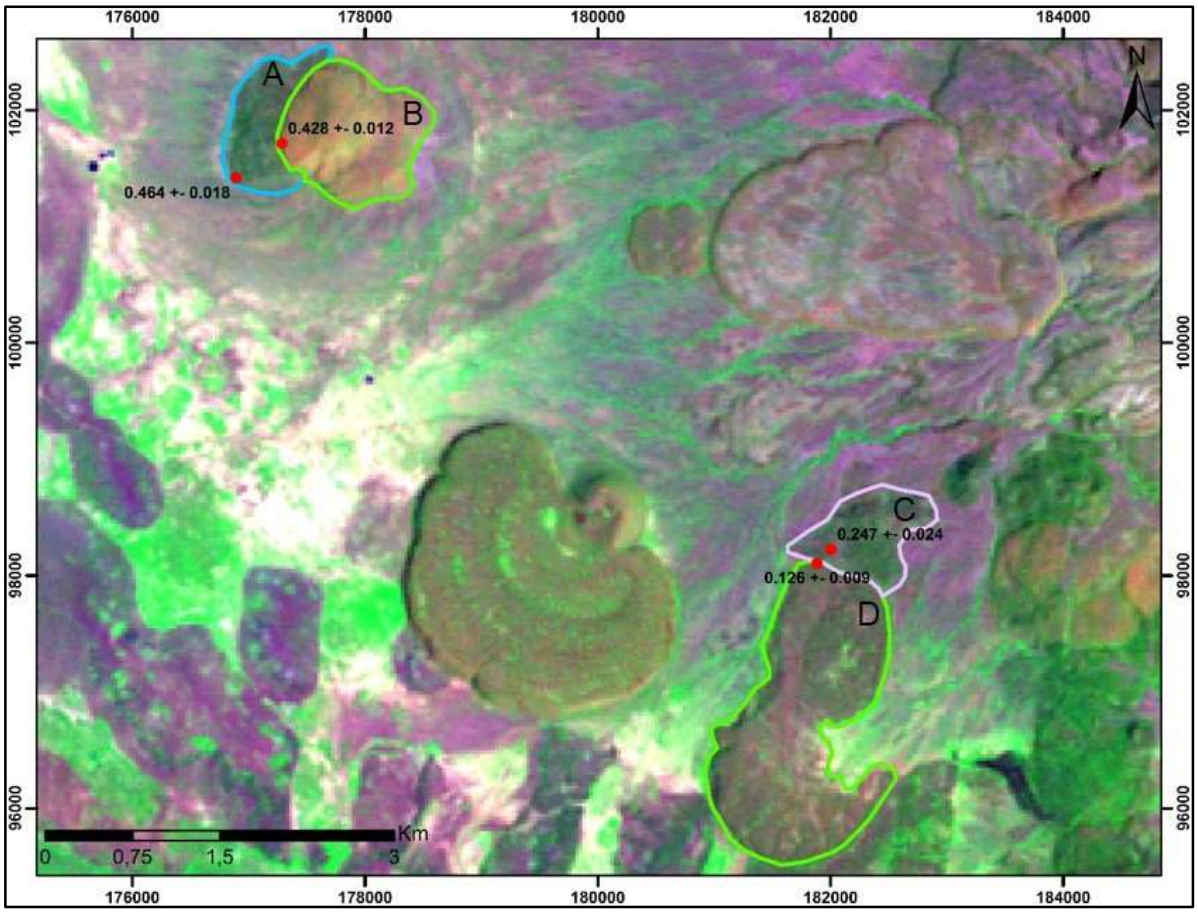

Figure 59: Landsat TM image of the western flank of Paka volcano showing two areas where the relative age determination of volcanic lava flows from mid-resolution satellite images was confirmed by $^{40}Ar/^{39}Ar$ age-dating.

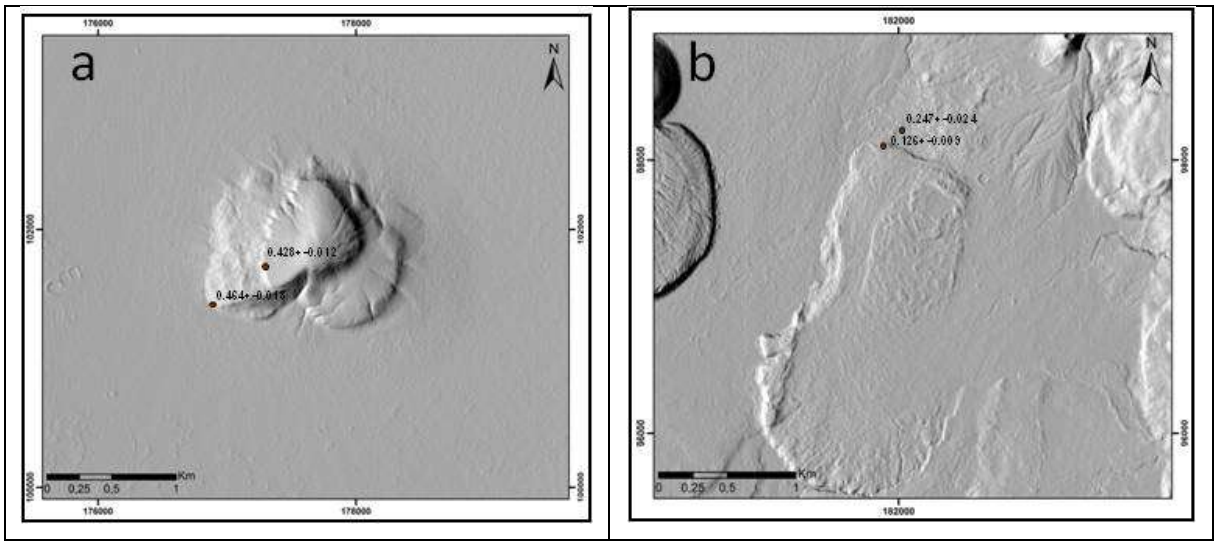

Figure 60: Detailed image of shaded relief map generated from DTM based on Pléiades satellite data supporting analyses of relative ages of neighbouring lava flows based on a mid-resolution satellite image. a) Lava flows A and B; b) lava flows C and D.

A comparison of the age dating results with the geological map of Dunkley et al. (1993) shows that the obtained ages do not coincide with the order of the geological units of the map and the associated report. For example, the Upper Trachytes are described to rest on the Lower and the Secumius Trachytes. The Lower and the Secumius Trachytes yielded ages between 0.405 Ma and 0.139 Ma, the Lower Trachyte yielded ages between 0.428 Ma and 0.012 Ma from the $^{40}Ar/^{39}Ar$ age dating. This implies, the ages of the different units overlap and belong therefore to different phases of volcanic activity.

For the evaluation of the evolution of the lava flows at Paka volcano, it is important to see whether the lava flows of the different phases cluster in distinct areas. Figure 61 shows the distribution of the lava flows of 1st, 2nd and 3rd phase (big dots; red, yellow, blue) together with the lava flows erupted prior to these phases (small dots; red, yellow, blue). It is noticeable that the lava flows prior to the 1st pronounced phase erupted in the northwest of Paka caldera. The seven flows of the 1st pronounced activity phase erupted northwest and northeast of the caldera. The lava flows erupted prior to the 2nd phase cluster mainly on the eastern flank, with one flow located in the northwest. The lava flows of the 2nd pronounced phase are distributed in the north, the west and the south. They show therefore no clustering in a distinct area. The lava flows erupted prior to and within the 3rd phase are concentrated in the central part of Paka.

It can generally be stated, that the oldest lava flows are located further away from Paka caldera, whereas the youngest lavas flows are located in the closer vicinity of the caldera. This could indicate either that the younger lava flows conceal the older ones or that the magma source changed its location over time.

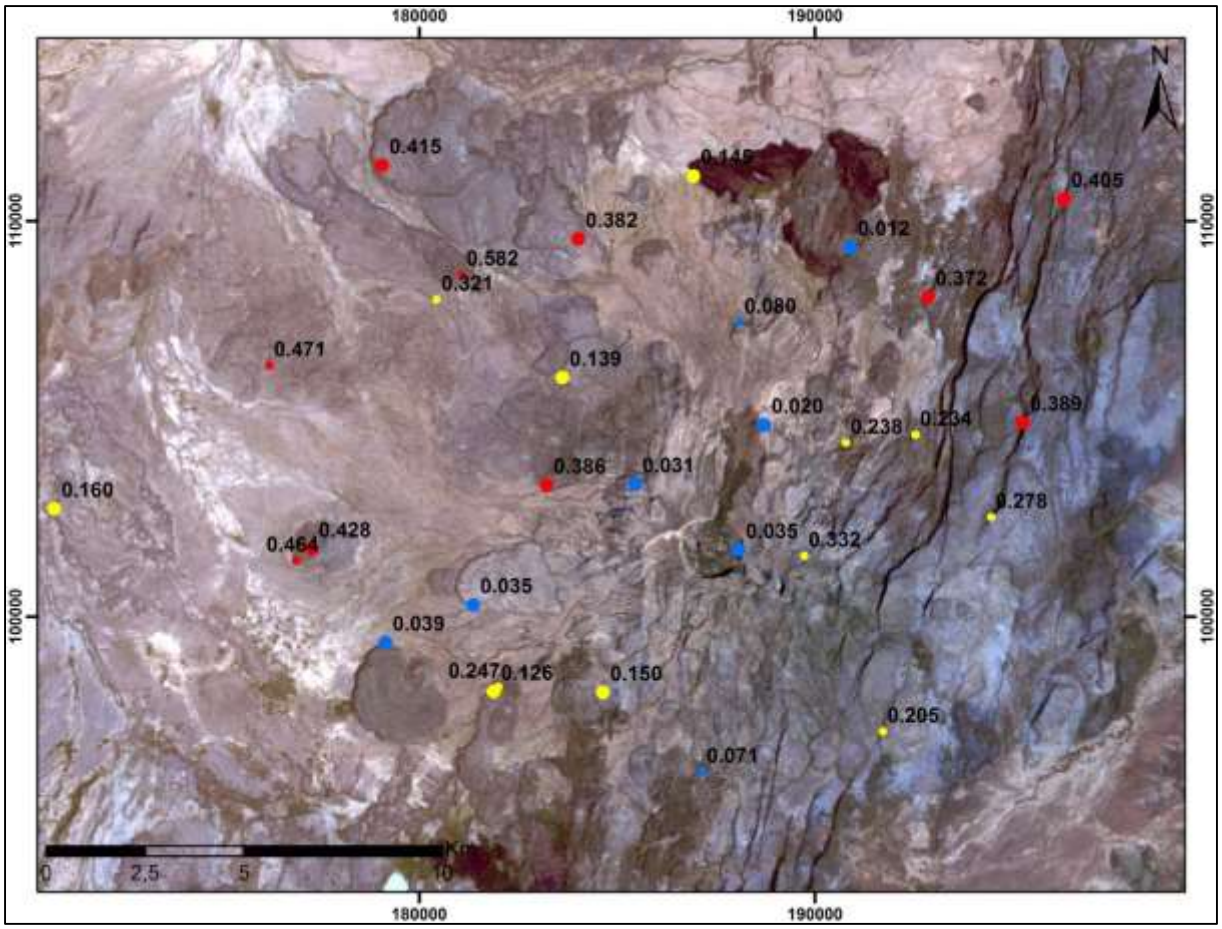

Figure 61: Age distribution of measured samples superimposed on the Landsat TM image, acquisition date 30/01/2010 (bands 1,2,3 RGB). red dots: lava flows prior to and of 1st pronounced activity phase; yellow dots: lava flows prior to and of 2nd pronounced activity phase; blue dots: lava flows prior to and of 3rd pronounced phase. Grid: UTM zone 37 N, WGS-84.

6 Field Training – Tectonics, seismicity, magmatic and geothermal processes of the East African Rift Valley, Kenya

Two Field Trainings about “Tectonics, seismicity, magmatic and geothermal processes of the East African Rift Valley, Kenya” were realised within the project for GDC staff members. For these trainings, the University of Potsdam was assigned.

6.1 Field Training 1 – May 18 to 24, 2014

Field Training 1 took place between May 18 and 24, 2014. The training was conducted by Prof. Dr. Manfred Strecker, Dr. Daniel Melnick and Simon Riedl of the University of Potsdam and Dr. Lydia Atieno Olaka of the University of Nairobi. Fourteen GDC staff members participated at the Field Training 1 (Table 11). The topics covered during the training were composed due to the requirements of GDC.

The Korosi-Paka volcanic complexes are located in the southern sector of the northern Kenyan Rift between Lake Baringo and Lake Turkana. Volcanic, hydrothermal and deformation processes provide a premier view of the youngest rifting processes. An additional aspect of the rift evolution is given by sedimentary deposits related to complex interactions between fluvial processes and multiple lake-level fluctuations during Quaternary. All these processes contribute to understand the degree of tectonic and volcanic activity and the relative chronological evolution in this region.

This one-week training focused on deciphering different geological archives and the analyses of spatiotemporal evolution of young zones of faulting. Fieldwork included the mapping of macro- and mesoscale fractures, normal faults, transfer faults, the assessment of fault-kinematic indicators on meso- and microscale levels, and the recognition of fault-controlled sedimentary environments and hydrologic flow paths. The training also included evening lectures on tectonics of extensional regions. The locations visited during the field training are shown in figure 62.

The lecture material used during this training is attached to the report in digital format (Attachment 13). The daily topics of field work and evening lectures covered during the training between May 18 and 24, 2014 are shortly described in the following.

Day 1 (Sun, May 18)

Fieldwork: morphologic and structural expression of the youngest fault generations in Menengai Caldera; interpretation of fractures and slickenside fault surfaces in light of kinematic characteristics; field recognition of kinematic indicators. Transfer to Lake Baringo.

Day 2 (Mon, May 19)

Fieldwork: stratigraphy of the Baringo-Korosi region; recognition of fluvial and pyroclastic strata; fracture systems vs. faults in extensional regions; cataclastic rocks; paleosols; fault scarps vs. fault-line scarps; kinematic transfer structures; refresher instruction on different fault and bedding measurements.

Lecture 1: tectonic characteristics of mantle diapir regions and the onset of rifting; diapirism and uplift of the lithosphere; geomorphic, climatic and environmental evidence; geophysical anomalies of mantle-diapir regions; melt generation and petrological evidence for mantle diapirism; diapirs, LIPs and extensional tectonism.

Day 3 (Tue, May 20)

Fieldwork: weathering characteristics of different lava flows: horst and graben landscapes; fault geometries and geomorphic expression of fault blocks; synthetic vs. antithetic faults; listric vs. planar geometries; structural development of the inner trough; structures of the eastern rift margin; fault expression of changing extension directions.

Lecture 2: tensional stress fields and extension processes; plate tectonic driving forces and extensional processes; tectonic stress field of Africa; different types of rifts; tectonic stretching models.

Day 4 (Wed, May 21)

Lectures and hands-on exercises at Soi Lodge, field visit of extensional features at Marigat in the afternoon.

Lecture 3 (in the morning): structural characteristics of extensional provinces; fault terminology; different types of normal faults; the role of inherited structures in extensional processes.

Hands-on exercise: construction of geological cross sections.

Lecture 4: kinematic indicators; different types of faulting; relevance of kinematic indicators for structural analysis; geomorphic indicators at outcrop and local scales; fluvial terraces; landforms associated with strike-slip faults; kinematic indicators on fault planes at mesoscale; characteristics of fault surfaces; Riedel R, R' and P shears (R = synthetic shear; R' = antithetic shear; P = synthetic minor fault); kinematic indicators on fault planes at microscale; what, and where should I measure?

Lecture 5 (in the afternoon): plotting structural data on a stereonet (refresher); basic concepts of stereographic projections; plotting fault-slip data; two types of stereonets; projection techniques: from a sphere to a plane; lines and planes.

Hands-on exercise: plots and calculations using manual techniques; plotting of own collection of fault data from first three days.

Hands-on exercise: measuring microfaults and extension fractures in monoclinal downwarp related to normal faulting; sedimentary features related to seismicity and liquefaction; spatial differences in fault density; assessment of inner-trough evolution.

Lecture 6 (in the evening): structural characteristics of extensional provinces; spatiotemporal growth of normal faults; sedimentation in extensional basins.

Day 5 (Thu, May 22)

Fieldwork: pre- and post-caldera structural evolution of Paka volcano; identification of different fault generations; caldera-related extensional structures; local vs. regional normal faults; strain dissipation and extensional systems.

Evening: discussion and wrap-up of observations in the northern rift sector.

Day 6 (Fri, May 23)

Fieldwork: fault-propagation and creation of accommodation space; faulting, volcanism and sedimentary processes in the south western Baringo area; lake-level changes, faulting and facies; progradation and coarsening upward sequences in lacustrine systems; geomorphic field evidence for climatically controlled lake-level fluctuations; preservation of organic materials in lake systems; alluvial fan – lacustrine interactions; role of calcretes; significance of stromatolites; multiple lake-level fluctuations of Lake Baringo and overflow hypothesis.

Day 7 (Sat, May 24)

Preparation for second field training; identification and evaluation of fault systems and volcano-tectonic segmentation in the southern Kenya Rift; manifestation of varying extensional regimes in volcanic and sedimentary rocks; young zones of extension and hydrothermal manifestations.

Table 11: List of participants of Field Training 1.

Joseph Gichira	jgichira@gdc.co.ke
George Igunza	gigunza@gdc.co.ke
Deflorah Kangogo	dkangogo@gdc.co.ke
Loice Kipchumba	lkipchumba@gdc.co.ke
Jeremiah Kipngok	Jkipngok@gdc.co.ke
Tito Lopeyok	tlopeyok@gdc.co.ke
Geoffrey Mibei	gmibei@gdc.co.ke
Marietta Mutonga	mmutonga@gdc.co.ke
Fredrick Mutua	fmutua@gdc.co.ke
Noel Ndombi	nndombi@gdc.co.ke
Lucy Njue	lnjue@gdc.co.ke
Yussuf Noor	ynoor@gdc.co.ke
David Nwai	dnwai@gdc.co.ke
David C. Oduor	doduor@gdc.co.ke

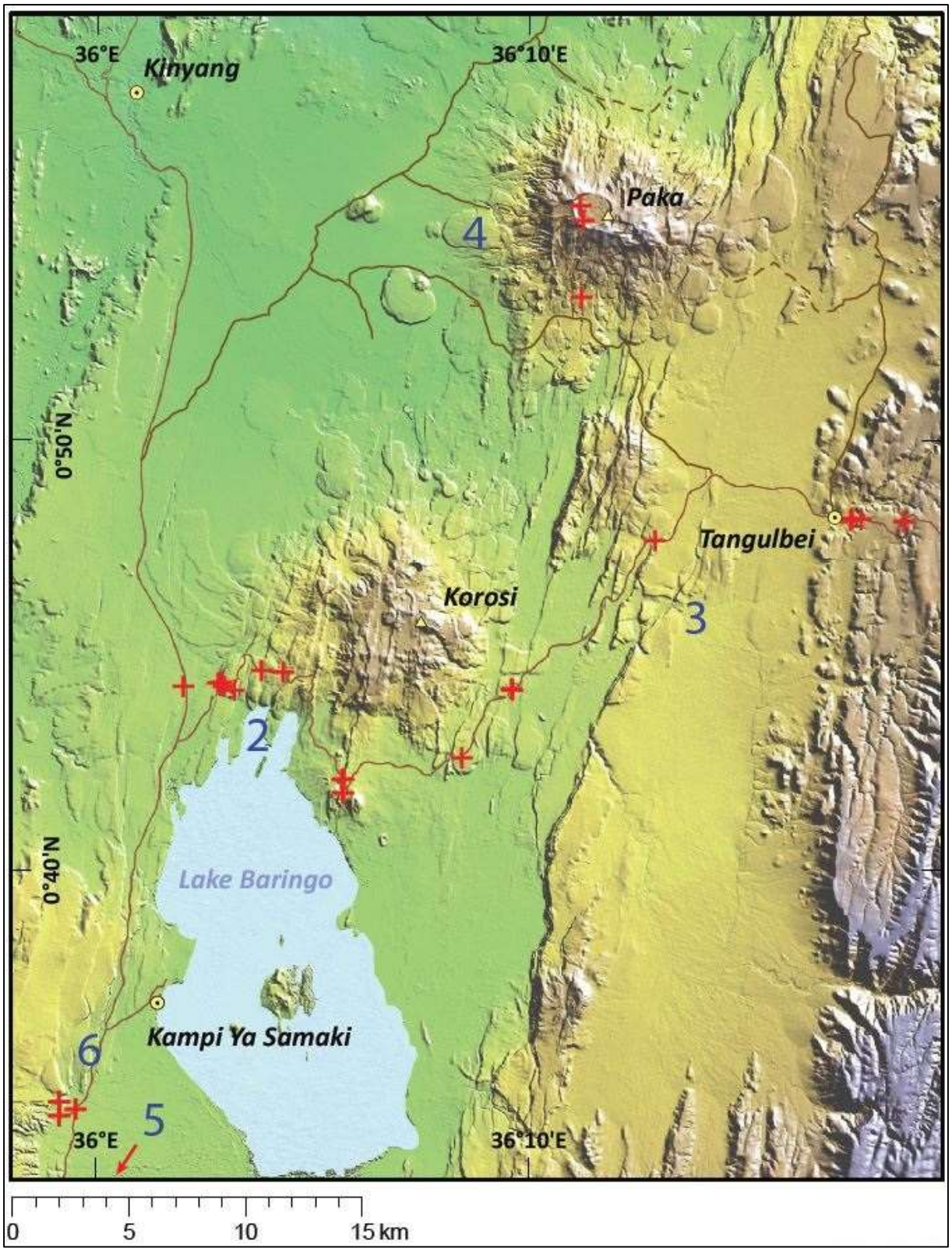

Figure 62: Locations visited during Field Training 1 (red crosses). Blue numbers indicate focus area of corresponding day. Days 1 and 7 (Menengai, Southern Kenya Rift) are not covered in this map.

6.2 Field Training 2 – September 20 to 26, 2014

Field Training 2 was conducted between September 20 and 26, 2014 by Prof. Dr. Manfred Strecker, Dr. Daniel Melnick and Simon Riedl of the University of Potsdam. Twelve GDC staff members and five students from Uganda and Tanzania participated this training (Table 12). The topics covered during the second training were assembled to the requirements of GDC. The locations visited during the training were selected in roundtable discussions in accordance to the objectives of the upcoming exploration and implementation phase of GDC in the Marigat – Korosi – Silali area.

Main objectives of the Field Training 2 was the identification of faults and tectonically created landforms that helps to understand the temporal and spatial evolution of young extension zones. Emphasis was given to the collection of field data, the integration of field observations into existing geological and geophysical data, and rock sampling techniques.

Field Training 2 additionally focussed on kinematic evolution of extensional fault systems. Outcrops in the Korosi-Paka-Silali area comprised examples of normal faulting and transfer zones with strike-slip kinematics. They therefore help to understand the long-term evolution of rift development and rift geometry in the tectonically active “inner trough”. Structures in the Marigat – Korosi area were visited to recapitulate, analyse and discuss the tectonic geomorphology of extension zones and to provide hands-on experiences in evaluating micro- and meso-scale kinematic indicators.

Outcrops in the Pliocene Chemeron Formation to the west of Paka highlighted the tectonics, stratigraphy and hydrothermal activity within rift units, which exemplify the composition and the structural setup of similar, younger Plio-Pleistocene units that may be encountered in exploratory drilling.

The caldera of Silali volcano and its flanks provided the unique opportunity to assess active faulting on rift volcanoes. Fault scarps and geothermally active areas were visited in order to provide the basis for a detailed discussion of the activity of structures of the larger Silali region. Visited locations comprised normal faults at the caldera rim and its floor, Katenmening crater to the south, and zones of normal and transfer faulting on the eastern flanks.

The lecture material used in Field Training 2 is attached to this report in digital format (Attachment 14). The locations visited during the field training are shown in figures 63 and 64. The daily lectures covered during Field Training 2 from September 20 to 26, 2014 are shortly described in the following:

Day 1 (Sat, September 20)

Drive to field-course venue at Lake Baringo with en route-stops to introduce, discuss and measure faults in Pliocene to mid-Pleistocene trachytes; analysis of slickensides in Quaternary faults in Marigat area.

Upon arrival at field-course venue discussion of program and targeted topics.

Day 2 (Sun, September 21)

Analysis of faults and extensional fractures in 0.37 Ma pyroclastic and fluvial strata and overlying 0.31 Ma trachyte flows; discussion of paleo-environmental sedimentary conditions, comparison with present-day phenomena along the active volcano-tectonic axis; fault-kinematic measurements of obliquely slipping normal faults and sinistral transfer faults; temporal characteristics of slickenside overprint phenomena and deformational history. Relationships between aligned volcanic canters, normal faults and fracture systems.

Characterization of relative fault activity, recognition of fault-ramps and fault-line scarps in the 0.4 Ma Baringo Trachytes.

Lecture: fault kinematic measurements and the use of STEREONET and FaultKin software.

Day 3 (Mon, September 22)

Analysis of the narrowing of the deformation zone in the inner trough of the rift; characterization of the 2.17 Ma fluvio-lacustrine Chemeron Formation beds; discussion of the role of frequent lake-level oscillations on sedimentary patterns, areal extent of lacustrine systems with depths >120 m, and activity of hydrothermal systems; discussion of insolation-driven climate forcing in the Kenya Rift and importance for logging cores in hydrothermal exploration; discussion of hydrothermally altered volcanics exposed within the Chemeron Formation as an analog for similar units encountered in exploratory drilling; recognition and characterization of synsedimentary faults in the Chemeron Formation; hydrothermal alteration of diatomaceous beds and the formation of cherty horizons in lacustrine systems.

Lecture: recapitulation of the tectonic evolution of the northern Kenya Rift and the importance of the Chemeron diatomaceous layers for regional sedimentary and tectonic reconstructions as well as paleoclimate assessments.

Roundtable discussion: structural target areas for mapping Silali caldera.

Day 4 (Tue, September 23)

Transfer of three teams to Silali volcano in two field vehicles and one helicopter; identification, mapping and sampling strategies to assess the degree of tectonic activity on Silali and adjacent fault zones; repeated systematic helicopter transfer of all groups to three observation stations; recognition of different levels of fault activity in an E-W transect across the volcanic edifice; discussion of post-collapse volcano-tectonic phenomena in light of recently acquired geophysical data; identification of localized thrusting and dextral strike-slip faulting in the volcanic edifice.

Day 5 (Wed, September 24)

Embedded, helicopter-aided two-shift training with geologists working on the characterization of fault zones on Silali; LiDAR-aided mapping of young fault zones, systematic sampling of volcanic units to date tectonic activity and to quantify vertical motion and amount of extension.

Separate group instruction for team 3 (participants, who had not been introduced concerning structural and geomorphic signals of young extensional processes affecting trachytes and sedimentary sequences); discussion of the fluvial knick point concept and recognition of tectonically active fault zones; migration of volcano-tectonic activity.

Day 6 (Thu, September 25)

Visit of the youngest manifestations of the volcano-tectonic zone on Ol Kokwe Island, Lake Baringo; relationships between faults, tilted fault blocks and hydrothermal manifestations; discussion of tectonic activity and the relationship with lake-level oscillations and the formation of staircase abrasion platforms and strandlines as marker horizons to quantify vertical motions.

Synopsis of northern rift evolution during a lecture at workshop venue; open discussion of structural evolution of Silali. Return to Nakuru in the late afternoon.

Day 7 (Fri, September 26)

Verification of remotely mapped structures and fissure system in the west-central sector of Menengai; measurements of sinistral fault motion indicators, recognition of altered shear zones, geomorphic aspects of sinistral faulting near well location 8. Recognition of fissure systems, horsetail structures and topography related fissure eruptions in an inferred dextrally oblique normal fault zone; discussion of structures and surface manifestations related to inflation of magma chambers.

Return to GDC management office, briefing of course-related activities. Return to Nairobi in early evening.

Table 12: List of participants of Field Training 2.

GDC staff members

Noel Ndombi	Fredrick Mutua
Loice Kipchumba	Evans Bett
Tito Lopeyok	Lawrence Ranka
Geoffrey Mibei	Joseph Gichira
David Oduor	Deflora Kangogo
David Mwai	Yussuf Noor

Students from Uganda and Tanzania

Solomon Maswi	James Natukunda
Edward Isabirye	Joseph Mmasy
Peter Mawejje	

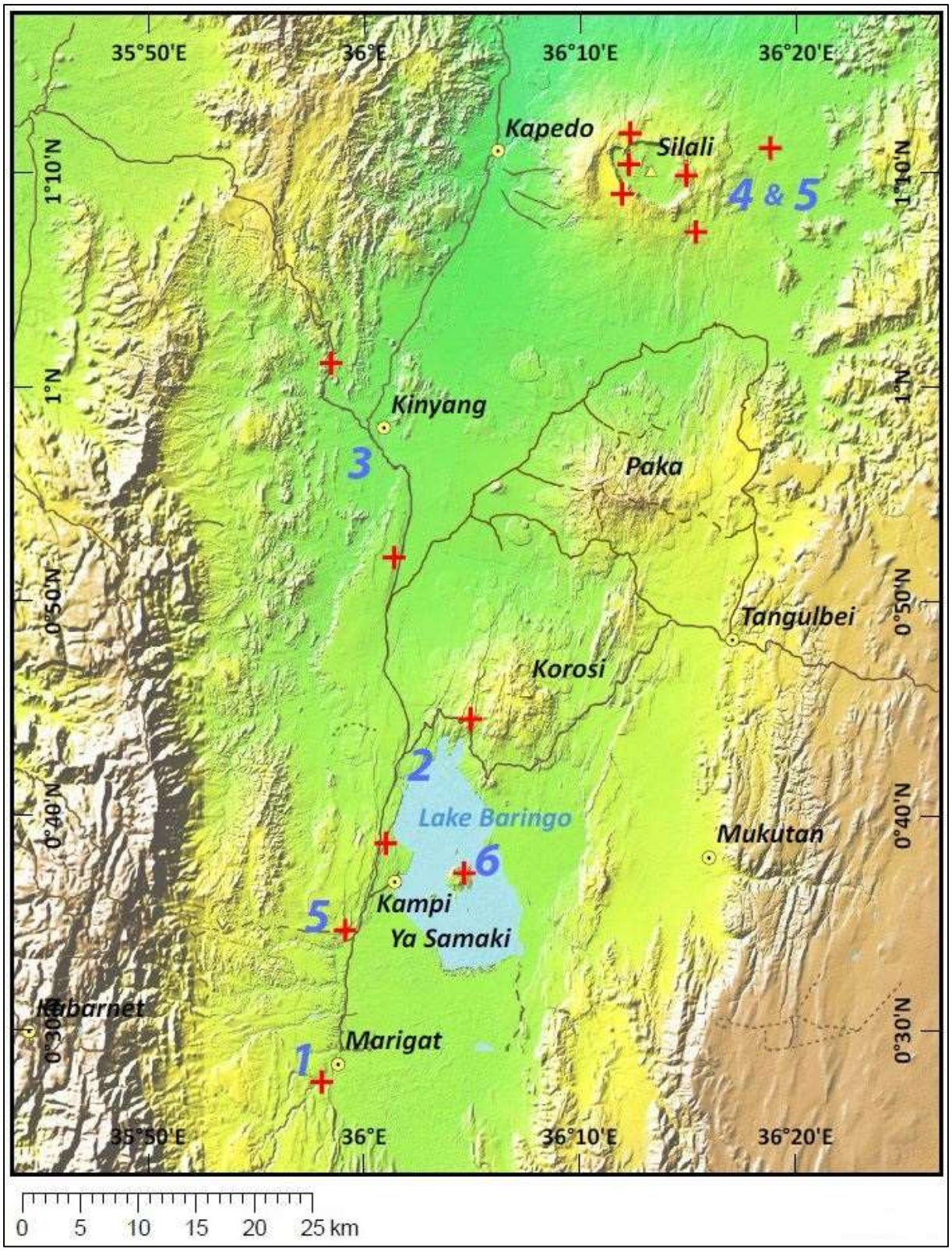

Figure 63: Locations visited during Field Training 2 from September 20 to 26 (red crosses) between Marigat and Silali volcano. Blue numbers indicate the corresponding day of field training. Day 7 at Menengai is not included on the map.

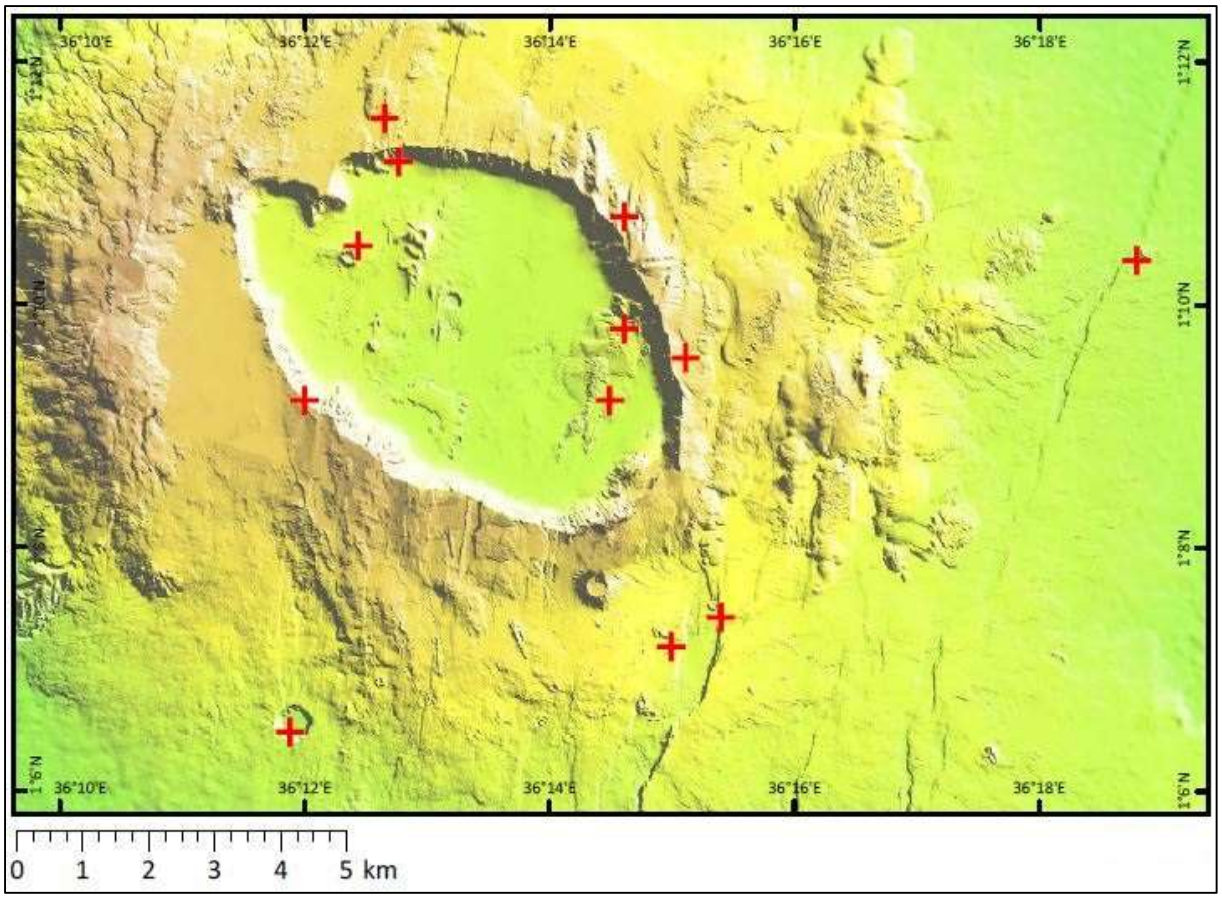

Figure 64: Locations (red crosses) visited at Silali volcano on Tuesday, September 23 and Wednesday, September 24 (days 4 and 5).

7 Summary and conclusion

This technical report summarizes the results achieved within the project “InSAR, structural analyses and dating of Paka volcanic products, Northern Kenya Rift”. All indicators of achievement according to the Implementation Agreement signed in 2013 are achieved.

An InSAR study for the period between 2006 and 2010 using Envisat data was performed. For the processing of the 11 suitable scenes, the SBAS method was used. More than two million points were identified within the Envisat-ASAR single image mode coverage of ~10,250 km². The results of the study are compiled in a shapefile, an accompanying surface deformation map and a time series plot of five points. The study shows only one area with a detectable surface deformation: The eastern flank of Paka volcano shows an uplift of up to 20 cm until February 2008. From October 2009 to September 2010, the area remains stable. This result correlates with two previous studies of Biggs et al. (2009 and 2013).

For the second InSAR study based on TerraSAR-X data, 17 scenes were acquired for the period between March and October 2013. The SBAS method was used to process of the data. The TerraSAR-X Strip Map Mode covered an area of ~1,900 km² and yielded more than three million points that are detectable during the entire investigation period. A shapefile compiles the parameter for every single point. Based on the shapefile, a surface deformation map for the entire area was created, as well as two time series plots of five points to show the development over time. Within the study area, two regions show a surface deformation. One is located in the north-western part of the study area. As the whole extent of this deformation area is not covered in the dataset and the area is quite far from Paka volcano the area is not discussed in detail in this report. The second area affected by deformation is the eastern flank of Paka volcano. A subsidence of up to 20 mm is detectable between March and July 2013. This subsidence is followed by a short period of stability and uplift of ~5 mm between August and October 2013.

The deformation rates of both InSAR studies are in the expectable range for volcanic areas. Such an alternating inflation and deflation has been detected and measured before in other volcanic regions. Important to mention is, that in both studies the deformation is concentrated on the eastern flank of Paka volcano.

For an area of ~420 km², a DTM with a spatial resolution of 4 m was generated using Pléiades satellite data. This DTM, together with the Landsat TM image was used for a structural analysis. Most faults are oriented in a N-S or NNE-SSW direction and show a right stepping en echelon arrangement of normal faults that correlates with the general orientation of the East African Rift Valley in northern Kenya. This development is typical for regions with an extensional behaviour as in the Kenyan Rift Valley. Another offset of linear structures were identified on the shaded relief map generated from the DTM. These lineaments are hardly visible on the Landsat TM image. These structures follow described Precambrian basement structures in a NW-SE direction. Geothermal manifestations in the form of fumarolic activity is strongly controlled by the faults and lineaments. They occur only in areas affected by tectonics and are bounded to the west by the Western Boundary fault close to the Paka caldera. This indicates that the faults give a pathway for the fumarolic activity. Also noticeable is that the analyses of the DTM data show no correlation with the InSAR data results. The areas of deformation show no change in their deformation behaviour directly at or close to the faults. Another field of application of such a high-resolution DTM is the infrastructural planning in the area of Paka. Delivered together with the DTM in tiff- and Ascii-format are 30 ortho-images of the area in tiff-format with a spatial resolution of 0.5 m.

The age dating of Paka volcanics was performed to analyse the eruptive history of the volcanic sequences. Aim was to determine whether there are periods with an intense volcanic activity and if these periods alternate with periods of minor volcanic activity. Interesting is also to determine the ages of the youngest lava flows. 32 lava flows and pyroclastic deposits were dated using the $^{40}Ar/^{39}Ar$ method. Sampling was performed in cooperation with GDC in February/March 2014. The age dating was performed at the University of Potsdam. 30 samples yielded reliable ages between ~0.6 and 0.012 Ma. Three pronounced periods of volcanic activity were distinguished: (1) between 0.428 and 0.372 Ma, (2) between 0.160 and 0.126 Ma, and (3) between 0.039 and 0.012 Ma. It is noticeable, that the periods of pronounced activity shorten towards present. The same can be observed for the periods with minor activity. Furthermore it can be noticed, that the lava flows erupted prior to and within the 1st phase are located further distant from the Paka caldera than the lava flows of the 2nd and 3rd phase. The youngest lavas erupted during the 3rd phase are concentrated in the closer vicinity of the Paka caldera. Generally, it can be stated that the older the lava flows, the further away they are located from Paka caldera. This could indicate either that the younger lava flows conceal the older ones or that the magma source changed its location over time.

Two Field Trainings about “Tectonics, seismicity, magmatic and geothermal processes of the East African Rift Valley, Kenya” were realised within the project. The first Field Training was conducted between May 18 to 24, 2014 in the area of Lake Baringo and Paka volcano. The second Field Training took place between September 20 and 26, 2014. During that training, locations at Lake Baringo and Silali were surveyed. The topics of both training units were composed to the wishes and requirements of GDC.

8 Acknowledgements

The German team expresses its sincere thanks to the management and staff of GDC for all of their very professional support during the whole mission and for the allocation of the excellent infrastructure and logistics. This has been essential for the success of this survey. Furthermore, we give credit to the Federal Ministry for Economic Cooperation and Development, Germany, which initiated the GEOTHERM Programme and financed the German contribution to this project.

9 References

Bamler, R. & Hartl, P. (1998): Synthetic aperture radar interferometry. IOPScience, Inverse Problems, Volume 14, Number 4.

Bamler, R (2006): Radar Interferometry for Surface Deformation Assessment. Summerschool Alpbach 2006.

Berardino, P., Fornaro, G., Lanari, R. & Sansosti, E. (2002): A New Algorithm for Surface Deformation Monitoring Based on Small Baseline Differential SAR Interferograms. IEEE Transaction on Geoscience and Remote Sensing, 40, 2375-2383.

Biggs, J., Anthony, E.Y., & Ebinger, C.J. (2009): Multiple inflation and deflation events at Kenyan volcanoes, East African Rift. Geology, 2009, Volume 37, Number 11, 979-982.

Biggs, J., Robertson, E. & Mace, M. (2013): ISMER – Active Magmatic Processes in the East African Rift: A Satellite Radar Perspective. Earth System Sciences, 81-91.

Biggs, J., Ebmeier, S.K., Aspinall, W.P., Lu, Z., Pritchard, M.E., Sparks, R.S.J. & Mather T.A. (2014): Global link between deformation and volcanic eruption quantified by satellite imagery. Nature Communications.

Chorowicz, J. (2005): The East African rift system. Journal of African Earth Sciences, 43, 379-410.

Cigna, F., Osmanoglu, B., Cabral-Cano, E., Dixon, T.H., Avila-Olivera J.A., Garduno-Monroy, V.H., DeMets, C. & Wdowinski, S. (2012): Monitoring land subsidence and its induced geological hazard with Synthetic Aperture Radar Interferometry: A case study in Morelia, Mexico. Remote Sensing of Environment, 117, 146 – 161.

Dunkley, P.M., Smith, M., Allen, D.J. & Darling W.G. (1993): The geothermal activity and geology of the northern sector of the Kenya Rift Valley. International Series, Research Report SC/93/1, 185pp, British Geological Survey.

Ferretti, A (2014): Satellite InSAR Data: reservoir monitoring from space. European Association of Geoscientists & Engineers.

Fleck, R.J., Sutter, J.F. & Elliot, D.H. (1977): Interpretation of discordant $^{40}Ar/^{39}Ar$ age-spectra of Mesozoic tholeiites from Antarctica. Geochimica et Cosmochimica Acta, 41, 15-32.

Frisch, W. & Meschede, M. (2007): Plattentektonik – Kontinentverschiebung und Gebirgsbildung, Primus Verlag.

Gatelli, F., Gaurnieri, M.M., Parizzi, F., Pasquali, P., Prati, C. & Rocca, F. (1994): The wavenumber shift in SAR interferometry. IEEE Transactions on Geoscience and Remote Sensing, 32(4), 855-865.

Holzner, J. (2003): Performance of Envisat/ASAR interferometric Products. Proc. Of Envisat Validation Workshop, Frascati, Italy, 9-13 December 2002 (ESA SP-531, August 2003).

Hutnak, M., Hurwith, S., Ingebritsen. S.E. & Hsieh, P.A. (2009): Numerical models of caldera deformation: Effects of multiphase and multicomponent hydrothermal fluid flow. Journal of Geophysical Research, 114.

Ishizuka, O. (1998): Vertical and horizontal variation of the fast neutron flux in a single irradiation capsule and their significance in the laser-heating $^{40}Ar/^{39}Ar$ analysis: Case study for the hydraulic rabbit facility of the JMTR reactor, Japan. Geochemical Journal, 32, 243-252.

Lagat, J., Wamalwa, A. & Ochieng, L. (2013): Baringo-Silali Block Prospect: Investigations for Geothermal Potential- A Geothermal Resource Assessment Project Report.

Lanphere, M.A. & Baadsgaard, H. (2001): Precise K-Ar, $^{40}Ar/^{39}Ar$, Rb-Sr and U/Pb mineral ages from the 27.5 Ma Fish Canyon Tuff reference standard. Chemical Geology, 175, 653-671.

Lundgren, P., Usai, S., Sansosti, R., Lanari, R., Tesauro, M., Fornaro, G. & Berardino, P. (2001): Modeling surface deformation observed with SAR Interferometry at Campei Flegrei Caldera. Journal of Geophysical Research, 106, 19355-19367.

Morley, C.K. (2010): Stress re-orientation along zones of weak fabrics in rifts: An explanation for pure extension in “oblique” rift segments?. Earth and Planetary Science Letters, 297, 667-673.

Omenda, P. (2010): Geothermal Exploration in Kenya. Short Course V on Exploration for Geothermal Resources, Lake Naivasha, Kenya.

Prati, C., Rocca, F., Monti Guarnieri, A. & Pasquali, P (1994): ESA Study Contract Report. Contract N. 3-7439/92/HE-I.C.

Schmitt, A.K., Grove, M., Harrison, T.M., Lovera, O., Hilen, J & Walters, M. (2003): The Geyzers – Cobb Mountain Magma System, Califonia (Part 1): U-Pb zircon ages of volcanic rocks, conditions of zircon crystallization and magma residence times. Geochimica et Cosmochimica Acta, 67, 3423-3442.

Smith, M. & Mosley, P.N. (1993): Crustal heterogeneity and basement influences on the development of the Kenya Rift, East Africa. Tectonics, 12, 591-606.

Sörgel, P. D.-I. (2008): Radar mit synthetischer Apertur (SAR)- Radarfernerkundung, Kapitel 5, Sommersemester 2008, Institut für Photogrammetrie und GeoInformation (IPI).

Tarikhi, P. (2012): InSAR of aquatic bodies. International Archives of the Photogrammetry, Remote Sensing and Spatial Information Sciences; ISPRS Congress, 25 August – 01 September, Melbourne, Australia.

Turrin, B.D., Donnelly-Nolan, J.M. & Hearn, B.C. Jr. (1994): $^{40}Ar/^{39}Ar$ ages from the rhyolite of Alder Creek, Califonia: Age of the Cobb Mountain Normal-Polarity Subchron revisited. Geology, 22, 251-254.

Usai, S. (2001): A new approach for long term monitoring of deformation by differential SAR interferometry. Ph.D. thesis, Delft Univ. Press, Delft, The Netherlands.

Uto, K., Ishizuka, O., Matsumoto, A., Kamioka, H. & Togashi, S (1997): Laser-heating $^{40}Ar/^{39}Ar$ dating system of the Geological Survey of Japan: System outline and preliminary results. Bulletin of the Geological Survey of Japan, 48, 23-46.

Wicks, C., Thather, W. & Dzurisin, D. (1998): Migration of Fluids Beneath Yellowstone Caldera Inferred from Satellite Radar Interferometry. Science, 282, 458-462.

York, D. (1969): Least squares fitting of a straight line with correlated errors. Earth Planetary Science Letters, 5, 320-324.

Online References

www.dlr.de

www.globalcmt.org

www.isc.ac.uk

www.uwgb.edu

Attachment 1: Surface Deformation Map of Paka Volcano, Kenya – Envisat-ASAR data

Surface Deformation Map of Paka Volcano, Kenya

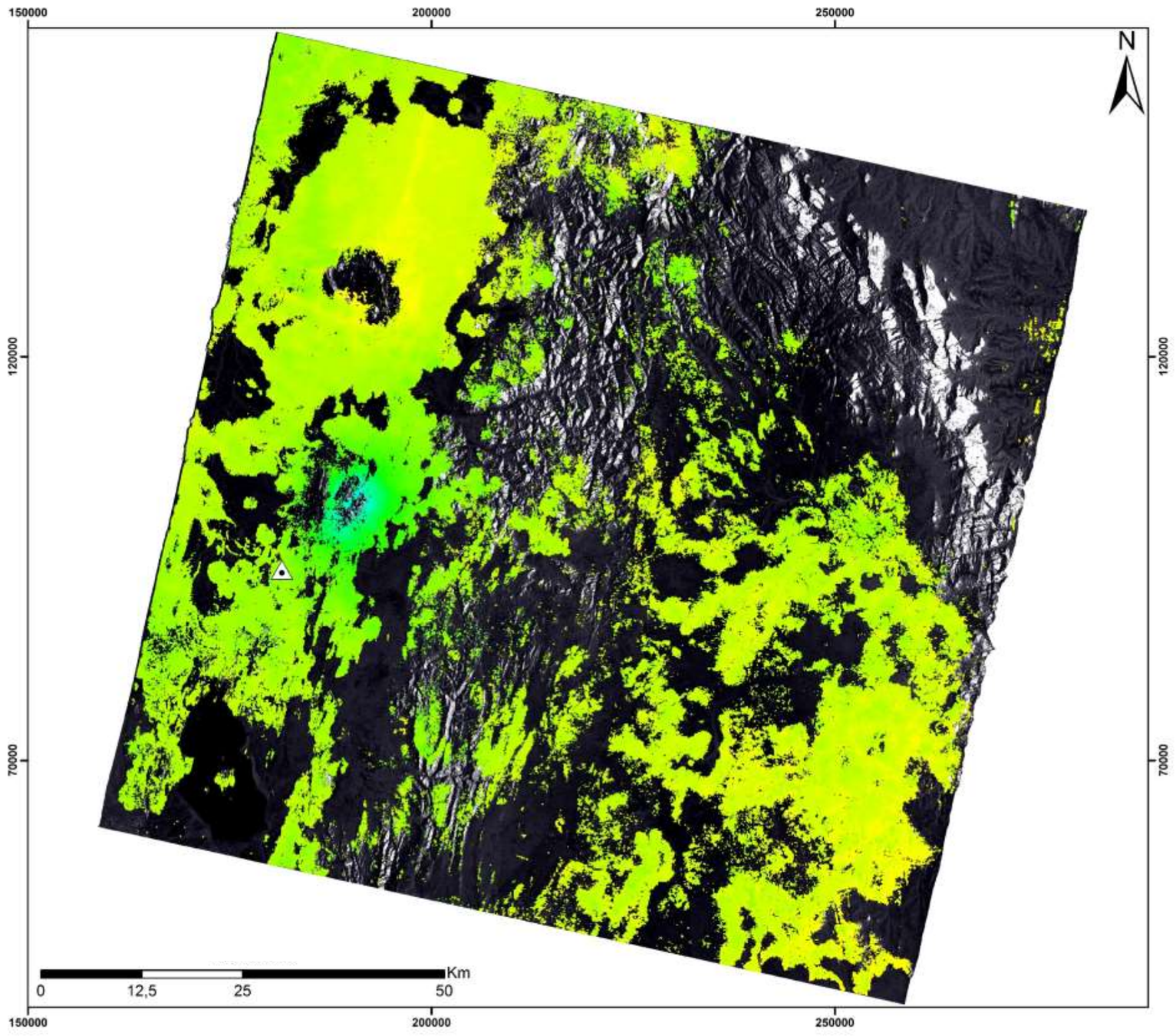

Spaceborne Surface Deformation Map generated from Envisat-ASAR ImagingMode Data

Location of Scene

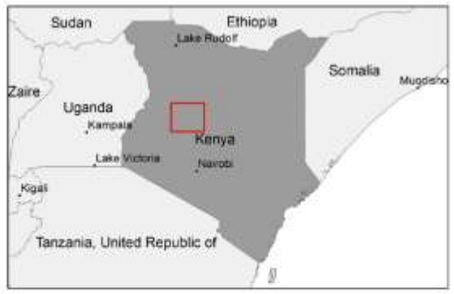

Vertical Movement

-60 [mm/yr] +60

Ground Control Point (GCP)

Map Projection:

Universal Transverse Mercator
Ellipsoid: WGS 84
Datum: WGS 84
Zone: 37 N

Satellite Image Information

Acquisition Date	2006-03-20 - 2010-09-20
Number of Scenes	11
Satellite	ENVISAT
Imaging Mode	ASAR ImagingMode
Ground Range Resolution	~ 20 m
Polarization	HH
Incidence Angle	~ 23°
Orbit Direction	Descending

Acknowledgment:

Map is based on SBAS processing performed by Airbus Defence and Space

Attachment 2: Surface Deformation Map of Paka Volcano, Kenya – TerraSAR-X data

Surface Deformation Map of Paka Volcano, Kenya

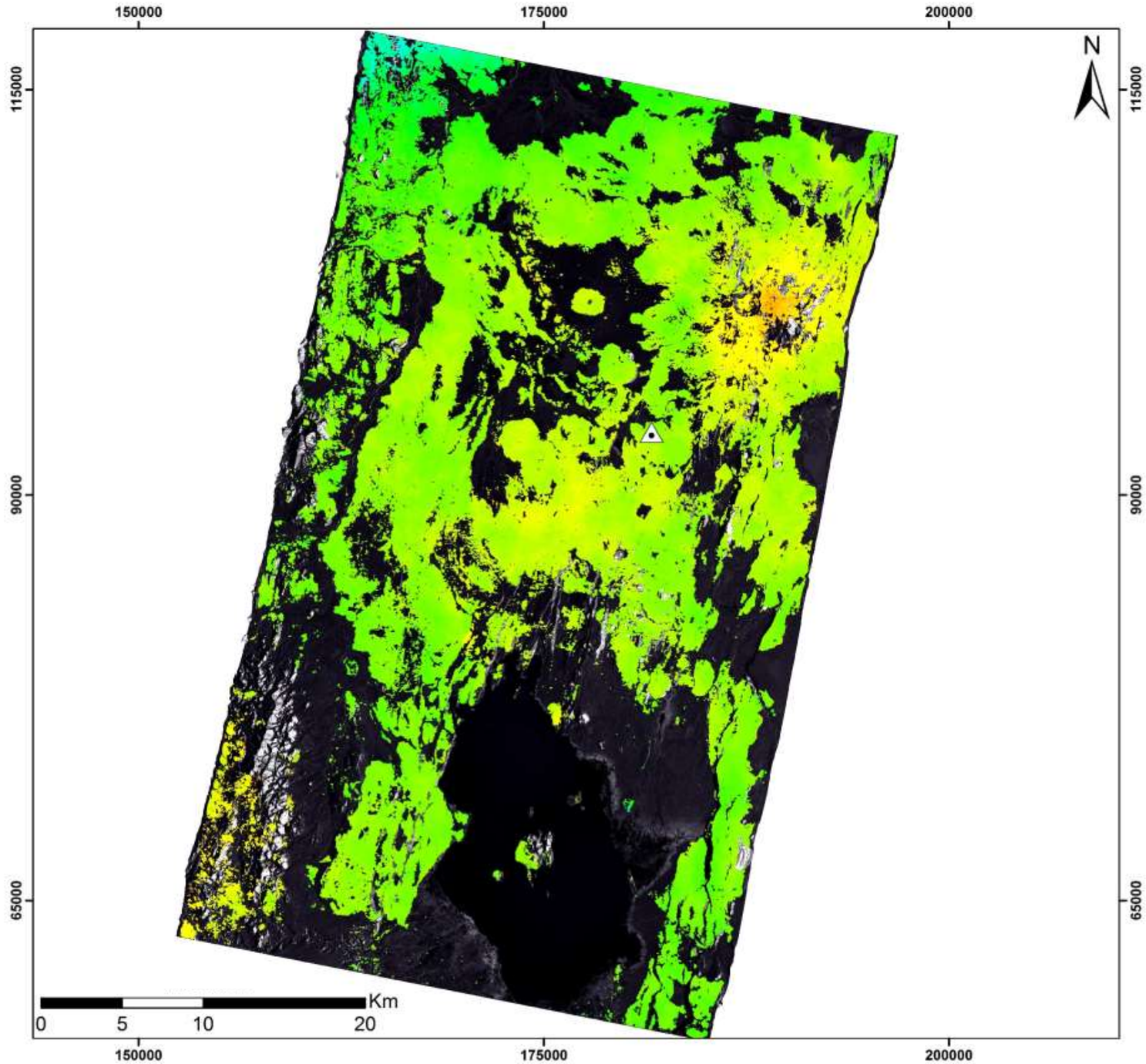

Spaceborne Surface Deformation Map generated from TerraSAR-X StripMap Data

Location of Scene

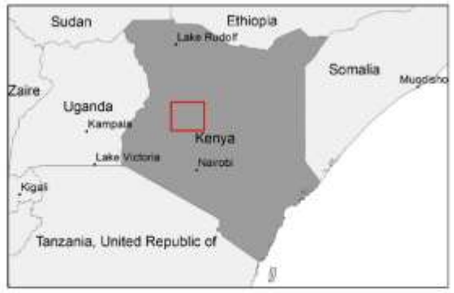

Vertical Movement

-60 [mm/yr] +60

Ground Control Point (GCP)

Map Projection:

Universal Transverse Mercator
Ellipsoid: WGS 84
Datum: WGS 84
Zone: 37 N

Satellite Image Information

Acquisition Date	2006-03-20 - 2010-09-20
Number of Scenes	11
Satellite	ENVISAT
Imaging Mode	ASAR ImagingMode
Ground Range Resolution	~ 20 m
Polarization	HH
Incidence Angle	~ 23°
Orbit Direction	Descending

Acknowledgment:

Map is based on SBAS processing performed by Airbus Defence and Space

Fieldname	**Data Type**	**Description**
FID	Object ID	Identification number of shape file feature
Shape	Point	Geometry of shape file
X	Double	Location of the feature: East value using the reference UTM zone [m]
Y	Double	Location of the feature: North value using the reference UTM zone [m]
Z	Double	Location of the feature: Height value based on the Digital Elevation Model value corrected using Interferometric measurement [m]
Velocity	Double	Average vertical surface deformation velocity [mm/year] - Positive value: uplift of measurement point - Negative value: subsidence of measurement point
V_Precisio	Double	Precision corresponding to the average surface deformation velocity at the measurement pixel [mm/year]
LOS_In	Double	Line-of-Sight of satellite (incidence angle) Has been used for transformation of LOS-measurement into vertical estimates [degree]
D_*YYYYMMDD*	Double	Vertical surface deformation at acquisition date *YYYYMMDD* (Y = Year, M = Month, D = Day) referred to the first acquisition date [mm] - Positive value: uplift of surface/ scatterer - Negative value: subsidence of surface/ scatterer

Attachment 9: Age dating, normal isochron and inverse isochron plots of $^{40}Ar/^{39}Ar$ analysis

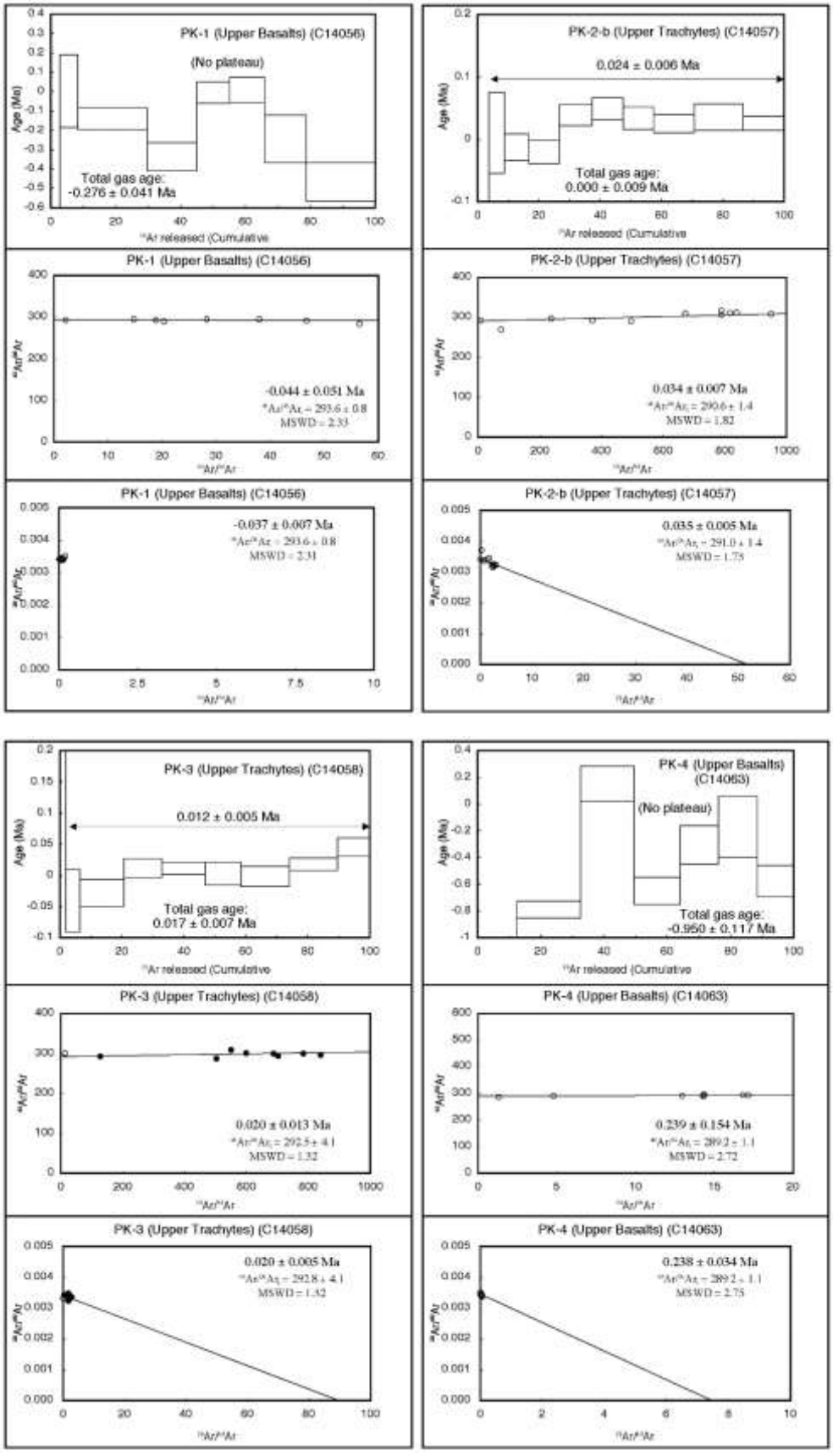

Attachment 9: Age dating, normal isochron and inverse isochron plots of $^{40}Ar/^{39}Ar$ analysis

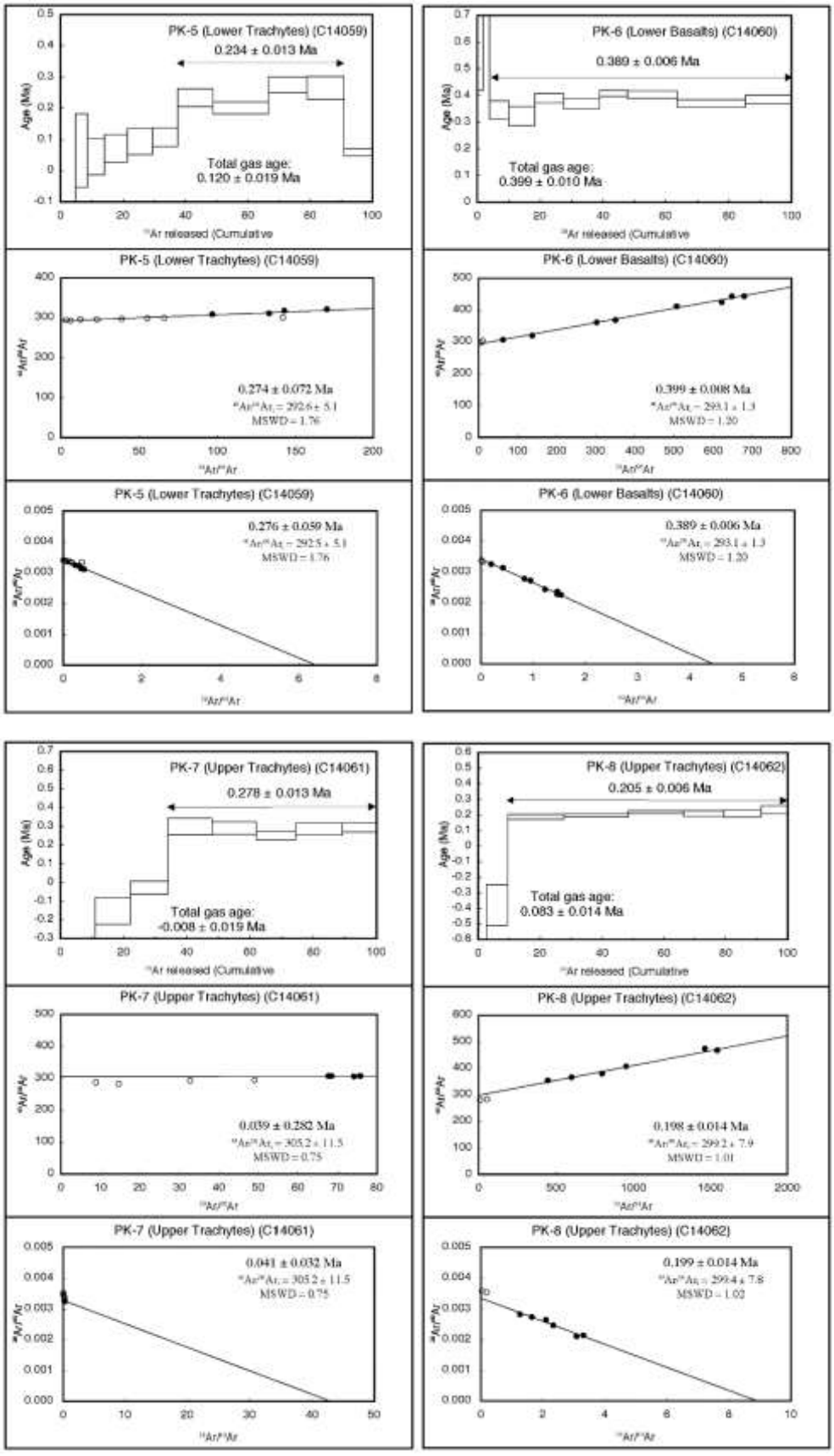

Attachment 9: Age dating, normal isochron and inverse isochron plots of $^{40}Ar/^{39}Ar$ analysis

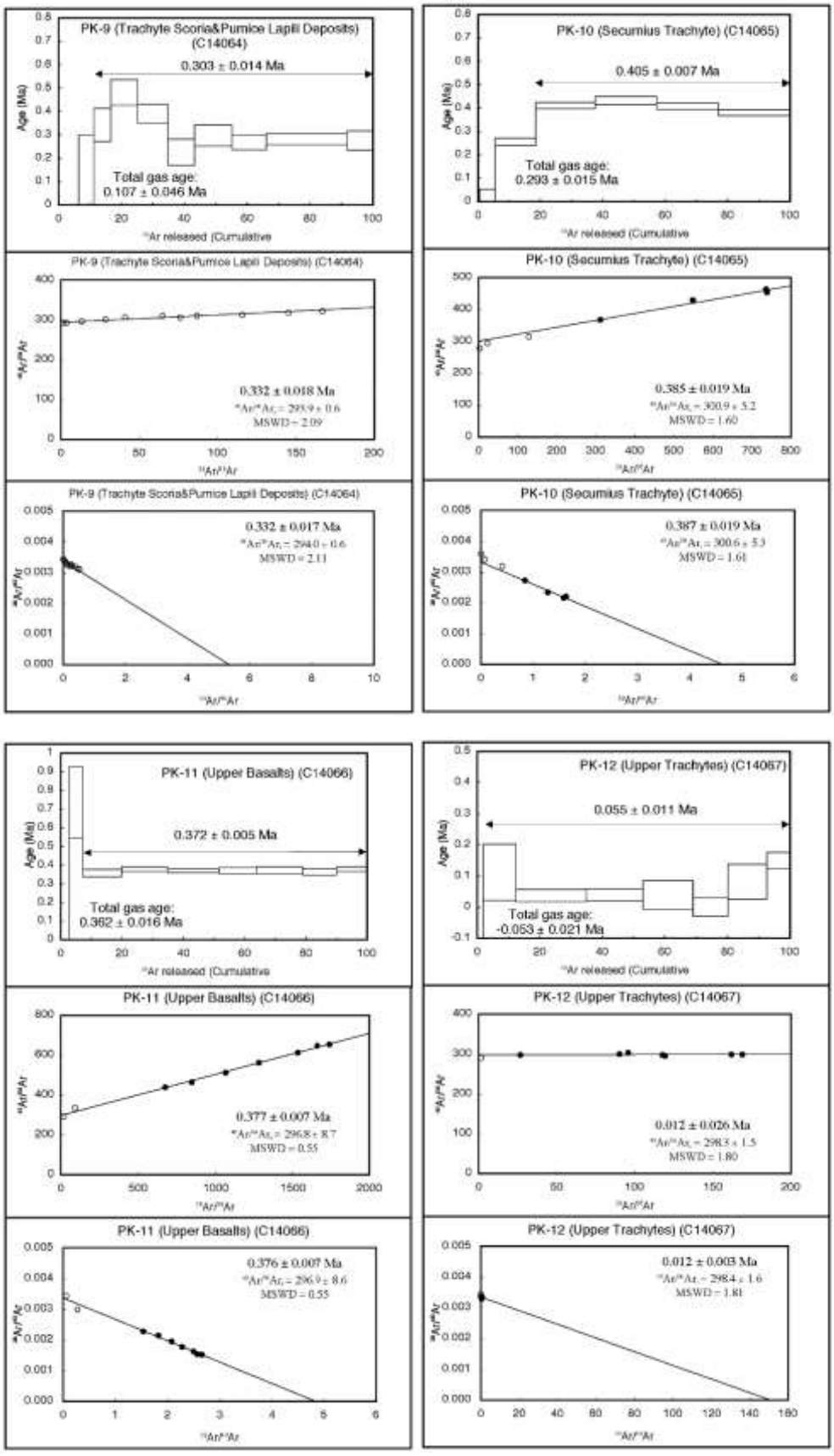

Attachment 9: Age dating, normal isochron and inverse isochron plots of $^{40}Ar/^{39}Ar$ analysis

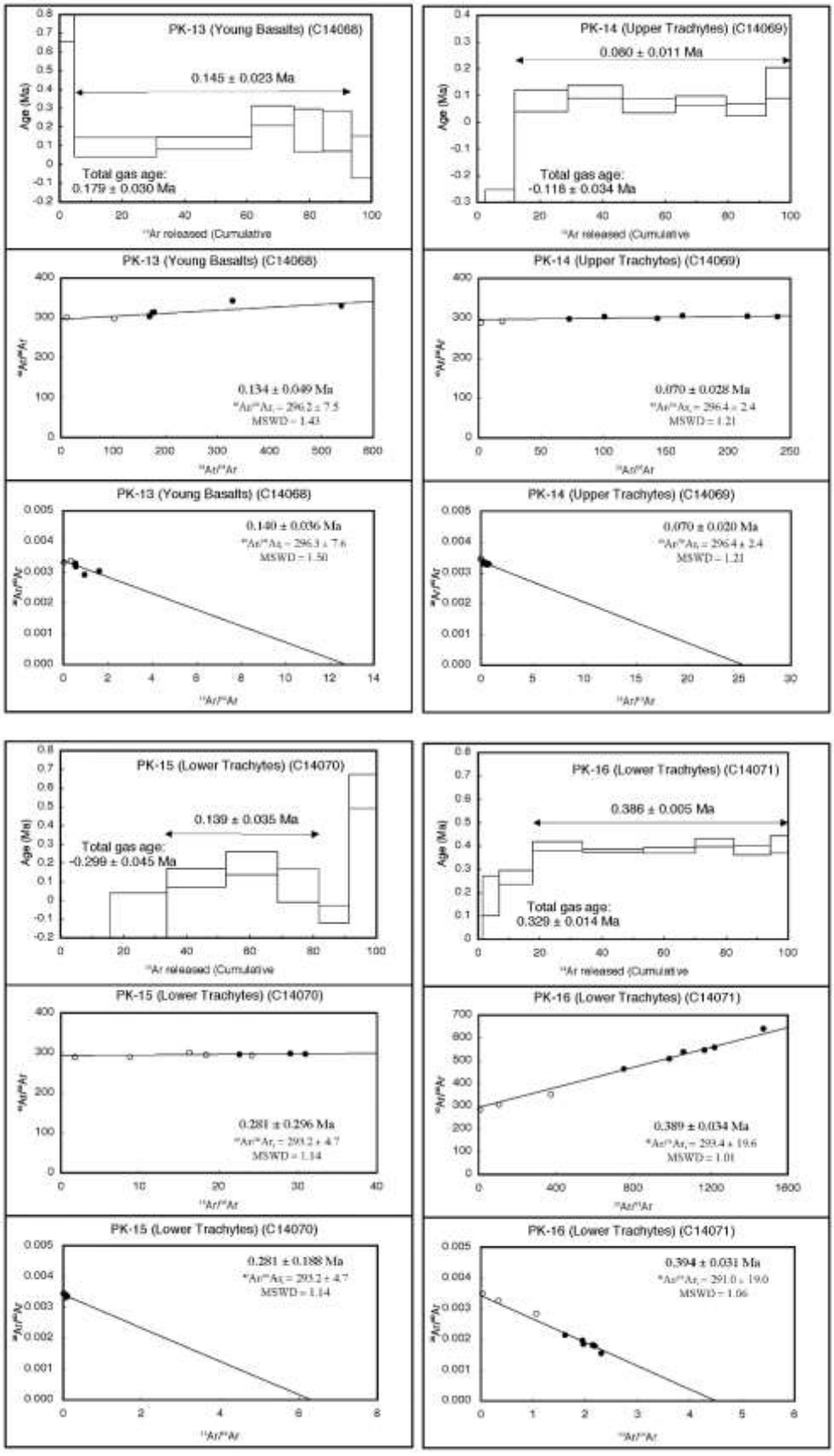

Attachment 9: Age dating, normal isochron and inverse isochron plots of $^{40}Ar/^{39}Ar$ analysis

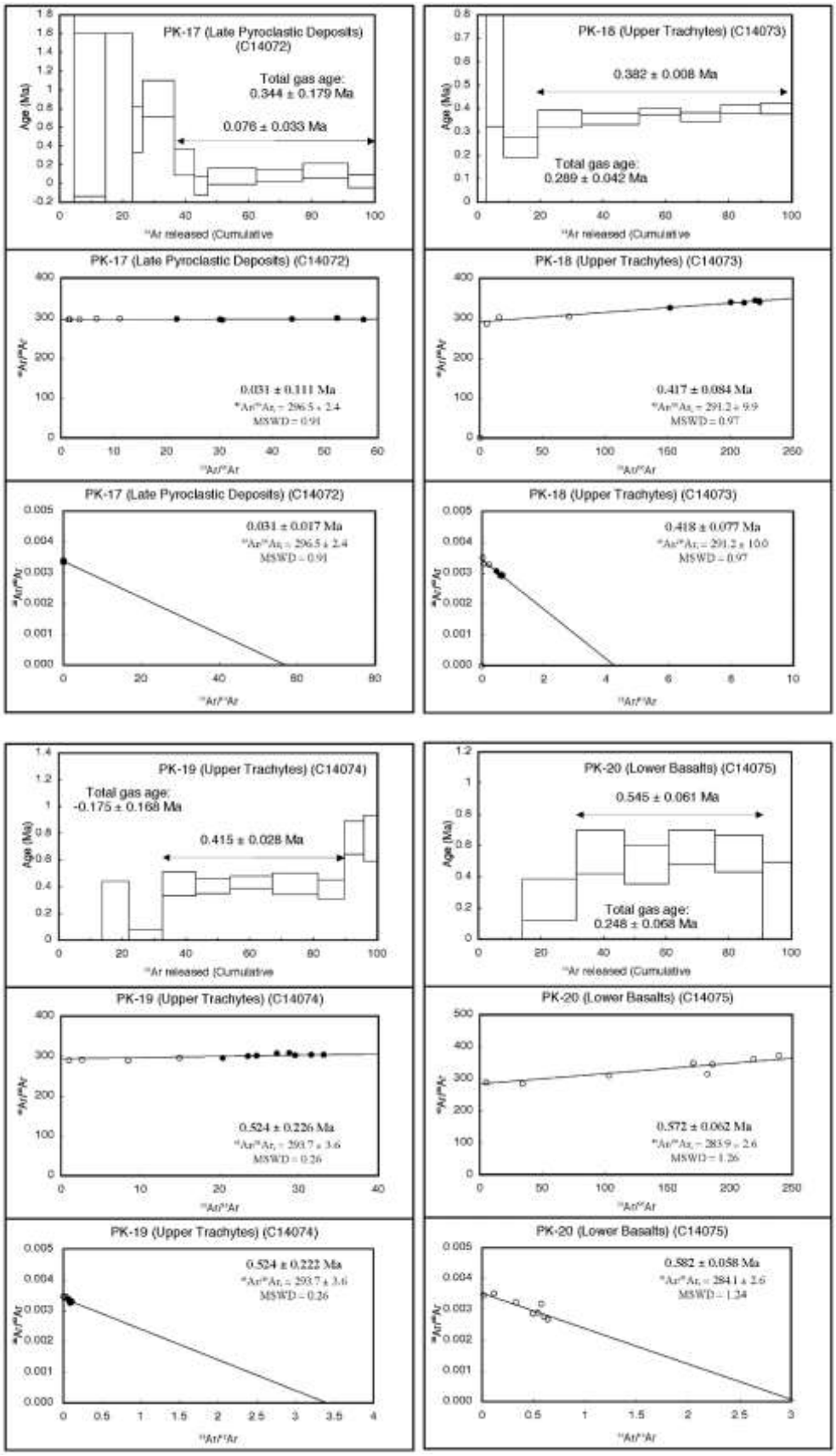

Attachment 9: Age dating, normal isochron and inverse isochron plots of $^{40}Ar/^{39}Ar$ analysis

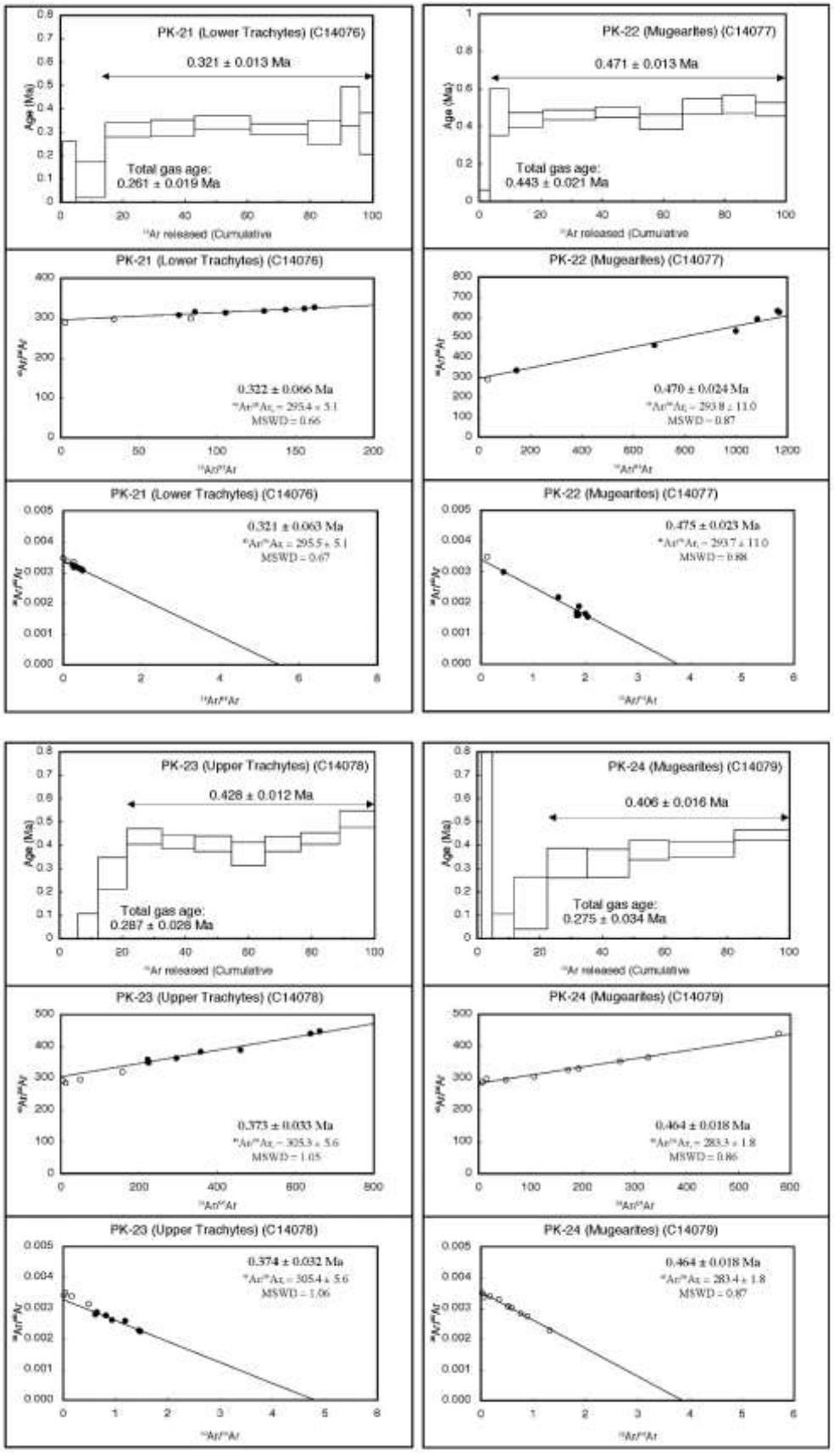

Attachment 9: Age dating, normal isochron and inverse isochron plots of $^{40}Ar/^{39}Ar$ analysis

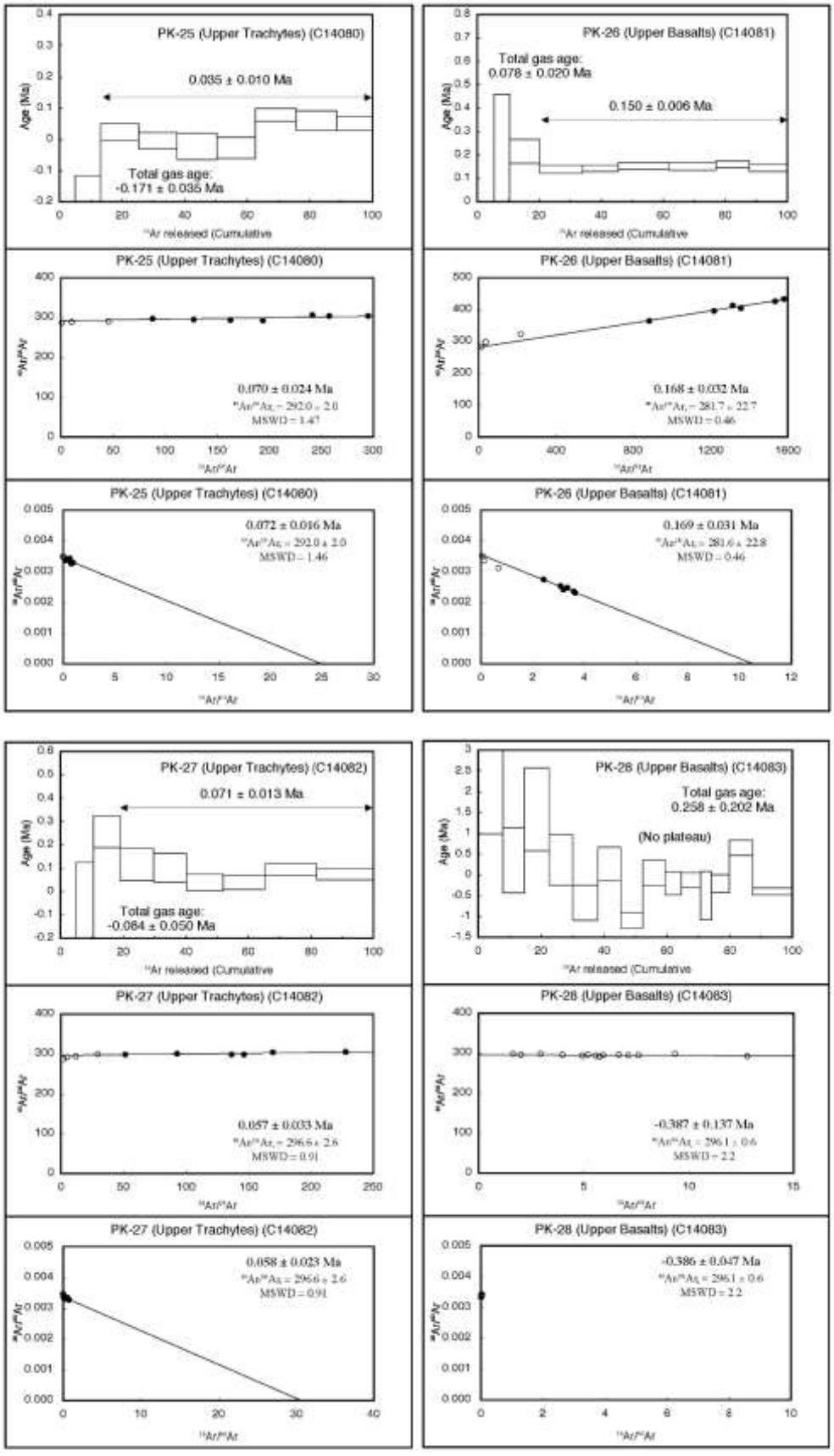

Attachment 9: Age dating, normal isochron and inverse isochron plots of $^{40}Ar/^{39}Ar$ analysis

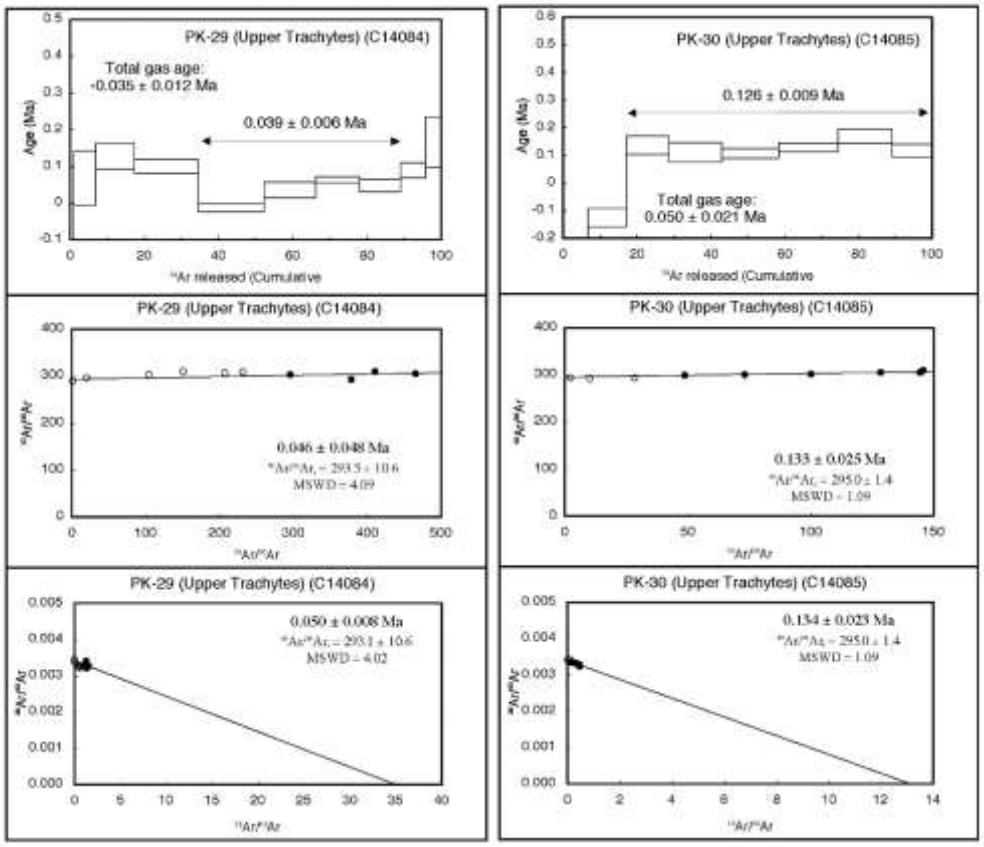

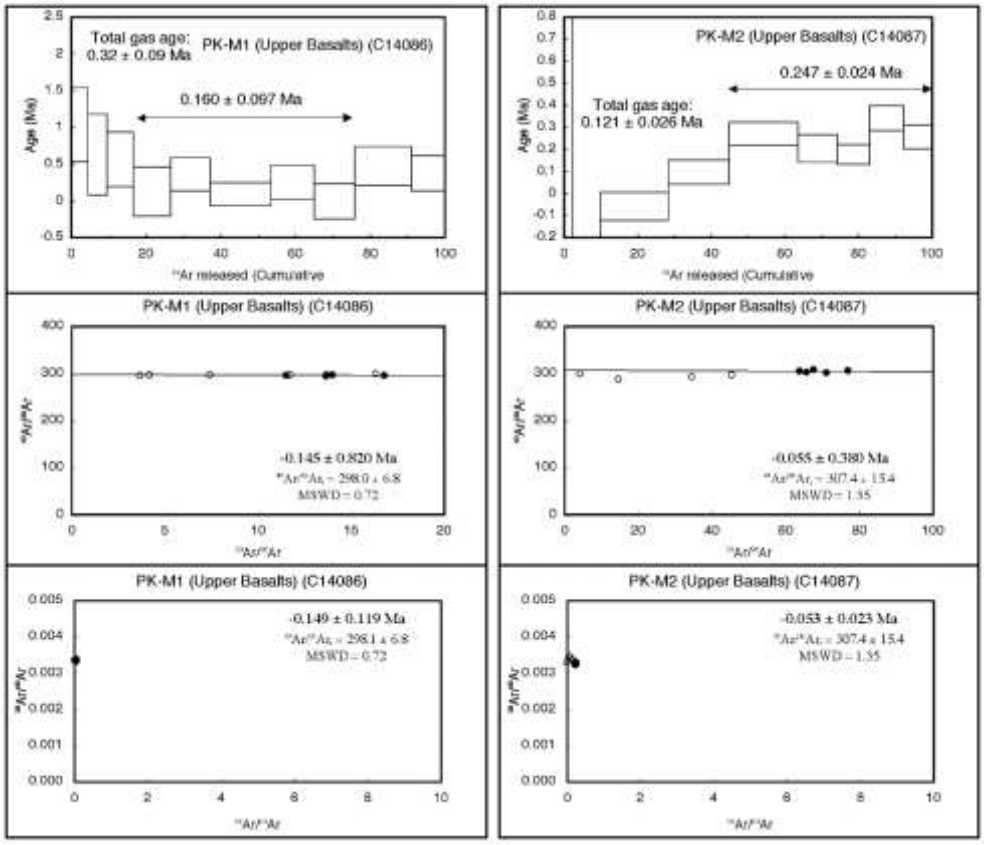

Attachment 10: $^{40}Ar/^{39}Ar$ analytical results of Paka volcanics

Laser Output*	$^{40}Ar/^{39}Ar$	$^{37}Ar/^{39}Ar$	$^{36}Ar/^{39}Ar$ (x10^{-3})	K/Ca	$^{40}Ar^{*}$ (%)	$^{39}Ar_{k}$ (%)	$^{40}Ar^{*}/^{39}Ar_{k}$	Age(±1s) (Ma)
Sample ID: PK-1 (Upper Basalts)								
J= 0.000994		*Laboratory ID: C14056*		*Neutron Irradiation ID: PO-2*				
1.6%	137.095 ± 0.6257	0.4117 ± 0.0038	468.412 ± 2.599	1.4284	-0.9	2.8	-1.2890 ± -0.4449	-2.313 ± -0.799
1.8%	20.0297 ± 0.0473	0.5087 ± 0.0025	67.912 ± 0.385	1.1560	0.0	5.5	0.0014 ± 0.1049	0.003 ± 0.188
2.2%	6.2535 ± 0.0102	0.6606 ± 0.0019	21.600 ± 0.106	0.8901	-1.2	21.4	-0.0779 ± -0.0309	-0.140 ± -0.055
2.4%	5.0422 ± 0.0076	0.6976 ± 0.0015	17.881 ± 0.139	0.8429	-3.7	15.2	-0.1874 ± -0.0409	-0.336 ± -0.073
2.6%	7.7792 ± 0.0078	0.6677 ± 0.0020	26.511 ± 0.107	0.8806	0.0	10.3	-0.0026 ± -0.0313	-0.005 ± -0.056
3.0%	10.4476 ± 0.0137	0.7236 ± 0.0022	35.532 ± 0.126	0.8126	0.0	10.7	0.0045 ± 0.0367	0.008 ± 0.066
3.6%	15.5621 ± 0.0195	0.7864 ± 0.0027	53.334 ± 0.234	0.7476	-0.9	12.7	-0.1369 ± -0.0684	-0.245 ± -0.123
4.2%	14.2569 ± 0.0217	0.9952 ± 0.0022	49.389 ± 0.195	0.5907	-1.8	21.3	-0.2600 ± -0.0553	-0.466 ± -0.099
	***Plateau age** (Plateau: **no plateau**) :*		±					
	***Total gas age** :*		***-0.276 ± 0.041***					
	***Normal isochron age** (of all steps) :*		***-0.044 ± 0.051***		*Initial $^{40}Ar/^{36}Ar$:*		*293.6 ± 0.8*	MSWD: 2.33
	***Inverse isochron age** (of all steps) :*		***-0.037 ± 0.007***		*Initial $^{40}Ar/^{36}Ar$:*		*293.6 ± 0.8*	MSWD: 2.31

Laser Output*	$^{40}Ar/^{39}Ar$	$^{37}Ar/^{39}Ar$	$^{36}Ar/^{39}Ar$ (x10^{-3})	K/Ca	$^{40}Ar^{*}$ (%)	$^{39}Ar_{k}$ (%)	$^{40}Ar^{*}/^{39}Ar_{k}$	Age(±1s) (Ma)
Sample ID: PK-2 (Upper Trachytes)								
J= 0.000992		*Laboratory ID: C14057*		*Neutron Irradiation ID: PO-2*				
1.6%	39.0806 ± 0.2387	0.1955 ± 0.0020	133.461 ± 0.843	3.0079	-0.9	1.4	-0.3419 ± -0.2009	-0.612 ± -0.360
1.8%	3.59557 ± 0.0164	0.1112 ± 0.0025	13.367 ± 0.264	5.2914	-9.6	2.2	-0.3458 ± -0.0773	-0.619 ± -0.138
2.2%	1.25229 ± 0.0052	0.0750 ± 0.0006	4.238 ± 0.122	7.8406	0.5	5.1	0.0057 ± 0.0362	0.010 ± 0.065
2.2%	0.7927 ± 0.0032	0.0654 ± 0.0005	2.724 ± 0.039	8.9906	-0.9	7.9	-0.0072 ± -0.0118	-0.013 ± -0.021
2.4%	0.5843 ± 0.0036	0.0548 ± 0.0005	2.031 ± 0.034	10.7360	-1.9	9.9	-0.0114 ± -0.0104	-0.020 ± -0.019
3.0%	0.4612 ± 0.0025	0.0456 ± 0.0004	1.499 ± 0.031	12.9126	4.7	10.8	0.0217 ± 0.0095	0.039 ± 0.017
3.6%	0.4022 ± 0.0027	0.0400 ± 0.0004	1.279 ± 0.033	14.7067	6.8	10.0	0.0274 ± 0.0099	0.049 ± 0.018
3.0%	0.3803 ± 0.0026	0.0404 ± 0.0003	1.234 ± 0.033	14.5692	4.9	10.0	0.0188 ± 0.0100	0.034 ± 0.018
3.4%	0.3889 ± 0.0023	0.0481 ± 0.0003	1.281 ± 0.026	12.2414	3.6	13.2	0.0141 ± 0.0079	0.025 ± 0.014
3.8%	0.3725 ± 0.0023	0.0663 ± 0.0004	1.210 ± 0.039	8.8723	5.4	16.0	0.0200 ± 0.0118	0.036 ± 0.021
4.2%	0.3252 ± 0.0026	0.0992 ± 0.0006	1.079 ± 0.020	5.9288	4.4	13.4	0.0143 ± 0.0063	0.026 ± 0.011
	***Plateau age** (Plateau: 3rd to 11th step) :*		***0.024 ± 0.006***					
	***Total gas age** :*		***0.000 ± 0.009***					
	***Normal isochron age** (of all steps) :*		***0.034 ± 0.007***		*Initial $^{40}Ar/^{36}Ar$:*		*290.6 ± 1.4*	MSWD: 1.82
	***Inverse isochron age** (of all steps) :*		***0.035 ± 0.005***		*Initial $^{40}Ar/^{36}Ar$:*		*291.0 ± 1.4*	MSWD: 1.73

Attachment 10: $^{40}Ar/^{39}Ar$ analytical results of Paka volcanics

Laser Output*	$^{40}Ar/^{39}Ar$	$^{37}Ar/^{39}Ar$	$^{36}Ar/^{39}Ar$ (x10^{-3})	K/Ca	$^{40}Ar^*$ (%)	$^{39}Ar_K$ (%)	$^{40}Ar^*/^{39}Ar_K$	Age(±1s) (Ma)
Sample ID: PK-3 (Upper Trachytes)								
J= 0.000992		*Laboratory ID: C14058*		*Neutron Irradiation ID: PO-2*				
1.6%	22.0181 ± 0.0850	0.0803 ± 0.0011	73.268 ± 0.406	7.3252	1.7	1.9	0.3736 ± 0.1164	0.668 ± 0.208
2.0%	2.30591 ± 0.0095	0.0491 ± 0.0007	7.893 ± 0.093	11.9695	-1.0	4.5	-0.0226 ± -0.0276	-0.040 ± -0.049
2.4%	0.5714 ± 0.0025	0.0338 ± 0.0002	1.997 ± 0.040	17.4101	-2.8	14.3	-0.0160 ± -0.0120	-0.029 ± -0.022
2.6%	0.4354 ± 0.0024	0.0305 ± 0.0002	1.460 ± 0.028	19.3090	1.5	12.3	0.0064 ± 0.0085	0.012 ± 0.015
2.8%	0.3829 ± 0.0023	0.0288 ± 0.0003	1.282 ± 0.017	20.4002	1.6	14.0	0.0063 ± 0.0056	0.011 ± 0.010
3.0%	0.3532 ± 0.0025	0.0282 ± 0.0003	1.197 ± 0.034	20.8573	0.4	11.6	0.0016 ± 0.0102	0.003 ± 0.018
3.4%	0.4189 ± 0.0025	0.0379 ± 0.0002	1.431 ± 0.030	15.5031	-0.3	15.6	-0.0011 ± -0.0090	-0.002 ± -0.016
3.8%	0.5026 ± 0.0023	0.0597 ± 0.0004	1.683 ± 0.018	9.8489	2.0	15.5	0.0099 ± 0.0057	0.018 ± 0.010
4.2%	0.5608 ± 0.0025	0.1119 ± 0.0005	1.842 ± 0.027	5.2580	4.5	10.4	0.0252 ± 0.0083	0.045 ± 0.015
	***Plateau age** (Plateau: 2nd to 9th step) :*		***0.012 ± 0.005***					
	Total gas age :		***0.017 ± 0.007***					
	***Normal isochron age** (of plateau steps) :*		***0.020 ± 0.013***	*Initial $^{40}Ar/^{36}Ar$:*			*292.5 ± 4.1*	MSWD: 1.32
	***Inverse isochron age** (of plateau steps) :*		***0.020 ± 0.005***	*Initial $^{40}Ar/^{36}Ar$:*			*292.8 ± 4.1*	MSWD: 1.32

Laser Output*	$^{40}Ar/^{39}Ar$	$^{37}Ar/^{39}Ar$	$^{36}Ar/^{39}Ar$ (x10^{-3})	K/Ca	$^{40}Ar^*$ (%)	$^{39}Ar_K$ (%)	$^{40}Ar^*/^{39}Ar_K$	Age(±1s) (Ma)
Sample ID: PK-4 (Upper Basalts)								
J= 0.000988		*Laboratory ID: C14063*		*Neutron Irradiation ID: PO-2*				
1.6%	216.777 ± 1.3779	0.7020 ± 0.0107	761.408 ± 7.423	0.8376	-3.8	3.1	-8.1686 ± -1.8675	14.619 ± -3.356
2.0%	60.9007 ± 0.2075	1.1044 ± 0.0072	209.348 ± 0.825	0.5322	-1.4	9.2	-0.8760 ± -0.1793	-1.562 ± -0.320
2.4%	22.3186 ± 0.0452	0.9291 ± 0.0039	77.269 ± 0.184	0.6327	-2.0	20.2	-0.4420 ± -0.0353	-0.788 ± -0.063
2.7%	20.6979 ± 0.0569	0.8323 ± 0.0043	69.976 ± 0.311	0.7064	0.4	17.1	0.0850 ± 0.0742	0.151 ± 0.132
3.0%	20.3758 ± 0.0332	0.7993 ± 0.0032	70.395 ± 0.218	0.7355	-1.8	14.5	-0.3638 ± -0.0562	-0.648 ± -0.100
3.3%	17.0352 ± 0.0286	0.8462 ± 0.0036	58.450 ± 0.285	0.6948	-1.0	12.0	-0.1709 ± -0.0808	-0.305 ± -0.144
3.7%	17.4647 ± 0.0532	1.0266 ± 0.0044	59.697 ± 0.455	0.5726	-0.5	12.2	-0.0956 ± -0.1277	-0.170 ± -0.228
4.2%	20.2469 ± 0.0399	1.5238 ± 0.0056	70.014 ± 0.253	0.3856	-1.6	11.6	-0.3236 ± -0.0660	-0.577 ± -0.118
	***Plateau age** (Plateau: **no plateau**) :*		±					
	Total gas age :		+					
	***Normal isochron age** (of all steps) :*		***-0.950 ± 0.117***	*Initial $^{40}Ar/^{36}Ar$:*			*289.2 ± 1.1*	MSWD: 2.72
	***Inverse isochron age** (of all steps) :*		***0.238 ± 0.034***	*Initial $^{40}Ar/^{36}Ar$:*			*289.2 ± 1.1*	MSWD: 2.75

Attachment 10: $^{40}Ar/^{39}Ar$ analytical results of Paka volcanics

Laser Output*	$^{40}Ar/^{39}Ar$	$^{37}Ar/^{39}Ar$	$^{36}Ar/^{39}Ar$ ($x10^{-3}$)	K/Ca	$^{40}Ar^*$ (%)	$^{39}Ar_K$ (%)	$^{40}Ar^*/^{39}Ar_K$	Age(±1s) (Ma)
Sample ID: PK-5 (Lower Trachytes)								
J= 0.000987		*Laboratory ID: C14059*			*Neutron Irradiation ID: PO-2*			
1.6%	88.0966 ± 0.2463	0.1161 ± 0.0045	299.941 ± 1.270	5.0659	-0.6	1.8	-0.5270 ± -0.3320	-0.939 ± -0.592
2.0%	46.4622 ± 0.1617	0.0803 ± 0.0023	158.695 ± 0.852	7.3246	-0.9	3.1	-0.4260 ± -0.2192	-0.759 ± -0.391
2.2%	24.0120 ± 0.0419	0.0555 ± 0.0007	81.151 ± 0.256	10.5907	0.2	3.7	0.0364 ± 0.0657	0.065 ± 0.117
2.4%	12.9527 ± 0.0122	0.0534 ± 0.0006	43.762 ± 0.114	11.0233	0.2	5.4	0.0253 ± 0.0331	0.045 ± 0.059
2.6%	7.6772 ± 0.0106	0.0616 ± 0.0003	25.859 ± 0.086	9.5501	0.5	7.3	0.0405 ± 0.0246	0.072 ± 0.044
3.0%	5.4014 ± 0.0050	0.0767 ± 0.0005	18.122 ± 0.079	7.6679	1.0	8.2	0.0524 ± 0.0232	0.093 ± 0.041
3.4%	4.5438 ± 0.0038	0.0911 ± 0.0003	15.196 ± 0.056	6.4548	1.3	7.9	0.0604 ± 0.0167	0.108 ± 0.030
3.8%	3.1781 ± 0.0045	0.0595 ± 0.0004	10.326 ± 0.055	9.8896	4.1	11.4	0.1314 ± 0.0160	0.234 ± 0.029
3.7%	2.3339 ± 0.0034	0.0414 ± 0.0002	7.528 ± 0.037	14.2020	4.8	17.7	0.1127 ± 0.0109	0.201 ± 0.019
4.0%	2.2252 ± 0.0039	0.0425 ± 0.0004	7.017 ± 0.047	13.8323	7.0	12.4	0.1550 ± 0.0140	0.276 ± 0.025
4.4%	1.8834 ± 0.0038	0.0626 ± 0.0003	5.886 ± 0.069	9.3984	7.9	12.0	0.1489 ± 0.0203	0.265 ± 0.036
4.8%	2.1126 ± 0.0047	0.0912 ± 0.0005	7.062 ± 0.024	6.4485	1.6	9.0	0.0328 ± 0.0068	0.058 ± 0.012
	Plateau age *(Plateau: 8th to 11th step)* :		***0.234 ± 0.013***					
	Total gas age :		***0.120 ± 0.019***					
	Normal isochron age *(of plateau steps)* :		***0.274 ± 0.072***		*Initial $^{40}Ar/^{36}Ar$:*		*292.6 ± 5.1*	MSWD: 1.76
	Inverse isochron age *(of plateau steps)* :		***0.276 ± 0.059***		*Initial $^{40}Ar/^{36}Ar$:*		*292.5 ± 5.1*	MSWD: 1.76

Laser Output*	$^{40}Ar/^{39}Ar$	$^{37}Ar/^{39}Ar$	$^{36}Ar/^{39}Ar$ ($x10^{-3}$)	K/Ca	$^{40}Ar^*$ (%)	$^{39}Ar_K$ (%)	$^{40}Ar^*/^{39}Ar_K$	Age(±1s) (Ma)
Sample ID: PK-6 (Lower Basalts)								
J= 0.000985		*Laboratory ID: C14060*			*Neutron Irradiation ID: PO-2*			
1.6%	61.393 ± 0.1720	0.0765 ± 0.0014	206.372 ± 0.815	7.6916	0.7	1.9	0.4160 ± 0.1806	0.739 ± 0.321
2.0%	27.2725 ± 0.1063	0.0572 ± 0.0010	90.182 ± 0.475	10.2757	2.3	2.0	0.6283 ± 0.1349	1.116 ± 0.240
2.4%	4.92964 ± 0.0085	0.0257 ± 0.0005	16.032 ± 0.067	22.9153	3.9	6.1	0.1943 ± 0.0191	0.345 ± 0.034
2.6%	2.34009 ± 0.0042	0.0203 ± 0.0004	7.309 ± 0.068	28.9515	7.8	8.3	0.1818 ± 0.0200	0.323 ± 0.036
2.8%	1.1982 ± 0.0032	0.0173 ± 0.0002	3.316 ± 0.032	33.9452	18.3	9.1	0.2196 ± 0.0096	0.390 ± 0.017
3.0%	1.0529 ± 0.0025	0.0156 ± 0.0002	2.865 ± 0.034	37.6475	19.7	11.6	0.2075 ± 0.0103	0.369 ± 0.018
3.2%	0.8113 ± 0.0027	0.0144 ± 0.0002	1.973 ± 0.019	40.8090	28.3	9.0	0.2295 ± 0.0062	0.408 ± 0.011
3.6%	0.6830 ± 0.0025	0.0201 ± 0.0002	1.548 ± 0.024	29.1998	33.2	15.8	0.2271 ± 0.0074	0.404 ± 0.013
4.0%	0.6838 ± 0.0024	0.0444 ± 0.0003	1.621 ± 0.026	13.2540	30.5	21.5	0.2085 ± 0.0080	0.370 ± 0.014
4.3%	0.6524 ± 0.0024	0.0788 ± 0.0003	1.493 ± 0.030	7.4599	33.3	14.8	0.2173 ± 0.0090	0.386 ± 0.016
	Plateau age *(Plateau: 3rd to 10th step)* :		***0.389 ± 0.006***					
	Total gas age :		***0.399 ± 0.010***					
	Normal isochron age *(of plateau steps)* :		***0.399 ± 0.008***		*Initial $^{40}Ar/^{36}Ar$:*		*293.1 ± 1.3*	MSWD: 1.20
	Inverse isochron age *(of plateau steps)* :		***0.389 ± 0.006***		*Initial $^{40}Ar/^{36}Ar$:*		*293.1 ± 1.3*	MSWD: 1.20

Attachment 10: $^{40}Ar/^{39}Ar$ analytical results of Paka volcanics

Laser Output*	$^{40}Ar/^{39}Ar$	$^{37}Ar/^{39}Ar$	$^{36}Ar/^{39}Ar$ ($x10^{-3}$)	K/Ca	$^{40}Ar^*$ (%)	$^{39}Ar_k$ (%)	$^{40}Ar^*/^{39}Ar_k$	Age(±1s) (Ma)
Sample ID: PK-7 (Upper Trachytes)								
J= *0.000984*		*Laboratory ID: C14061*		*Neutron Irradiation ID: PO-2*				
1.6%	32.3515 ± 0.0837	0.1546 ± 0.0013	112.885 ± 0.506	3.8039	-3.1	4.8	-0.9940 ± -0.1431	-1.765 ± -0.254
2.0%	19.3354 ± 0.0418	0.0865 ± 0.0011	68.239 ± 0.238	6.8006	-4.3	6.2	-0.8226 ± -0.0648	-1.461 ± -0.115
2.4%	8.9596 ± 0.0205	0.0574 ± 0.0007	30.626 ± 0.143	10.2419	-1.0	11.1	-0.0859 ± -0.0404	-0.153 ± -0.072
2.7%	5.9967 ± 0.0129	0.0417 ± 0.0002	20.357 ± 0.067	14.0994	-0.3	12.0	-0.0154 ± -0.0194	-0.027 ± -0.034
3.0%	4.5328 ± 0.0097	0.0346 ± 0.0003	14.778 ± 0.084	16.9775	3.7	13.9	0.1686 ± 0.0249	0.299 ± 0.044
3.3%	4.0635 ± 0.0054	0.0356 ± 0.0004	13.207 ± 0.062	16.5107	4.0	14.1	0.1636 ± 0.0183	0.290 ± 0.032
3.6%	4.1231 ± 0.0048	0.0426 ± 0.0007	13.487 ± 0.043	13.8179	3.4	12.3	0.1411 ± 0.0124	0.250 ± 0.022
4.0%	4.0664 ± 0.0053	0.0641 ± 0.0004	13.236 ± 0.060	9.1819	3.9	14.7	0.1602 ± 0.0174	0.284 ± 0.031
4.4%	4.4788 ± 0.0061	0.0900 ± 0.0003	14.621 ± 0.047	6.5330	3.7	10.9	0.1654 ± 0.0131	0.294 ± 0.023
	Plateau age *(Plateau: 5th to 9th step) :*		***0.278 ± 0.013***					
	Total gas age :		***-0.008 ± 0.019***					
	Normal isochron age *(of plateau steps) :*		***0.039 ± 0.282***		*Initial $^{40}Ar/^{36}Ar$:*		*305.2 ± 11.5*	MSWD: 0.75
	Inverse isochron age *(of plateau steps) :*		***0.041 ± 0.032***		*Initial $^{40}Ar/^{36}Ar$:*		*305.2 ± 11.5*	MSWD: 0.75

Laser Output*	$^{40}Ar/^{39}Ar$	$^{37}Ar/^{39}Ar$	$^{36}Ar/^{39}Ar$ ($x10^{-3}$)	K/Ca	$^{40}Ar^*$ (%)	$^{39}Ar_k$ (%)	$^{40}Ar^*/^{39}Ar_k$	Age(±1s) (Ma)
Sample ID: PK-8 (Upper Trachytes)								
J= *0.000983*		*Laboratory ID: C14062*		*Neutron Irradiation ID: PO-2*				
1.6%	28.3549 ± 0.1252	0.1118 ± 0.0014	101.457 ± 0.672	5.2597	-5.7	2.7	-1.6170 ± -0.1933	-2.870 ± -0.344
2.0%	5.13659 ± 0.0687	0.0715 ± 0.0011	18.123 ± 0.257	8.2235	-4.1	6.9	-0.2130 ± -0.0736	-0.378 ± -0.131
2.4%	0.47464 ± 0.0049	0.0456 ± 0.0008	1.262 ± 0.028	12.8854	22.2	18.2	0.1054 ± 0.0089	0.187 ± 0.016
2.7%	0.30295 ± 0.0025	0.0353 ± 0.0002	0.657 ± 0.015	16.6870	36.9	20.7	0.1117 ± 0.0051	0.198 ± 0.009
3.0%	0.3243 ± 0.0024	0.0311 ± 0.0003	0.691 ± 0.019	18.8999	37.8	18.0	0.1225 ± 0.0060	0.217 ± 0.011
3.3%	0.4269 ± 0.0027	0.0324 ± 0.0004	1.056 ± 0.033	18.1807	27.5	12.9	0.1173 ± 0.0099	0.208 ± 0.018
3.7%	0.6094 ± 0.0024	0.0514 ± 0.0003	1.677 ± 0.041	11.4473	19.3	12.1	0.1177 ± 0.0124	0.209 ± 0.022
4.2%	0.7904 ± 0.0027	0.1021 ± 0.0010	2.257 ± 0.052	5.7610	16.6	8.5	0.1315 ± 0.0155	0.233 ± 0.027
	Plateau age *(Plateau: 3rd to 8th step) :*		***0.205 ± 0.006***					
	Total gas age :		***0.083 ± 0.014***					
	Normal isochron age *(of plateau steps) :*		***0.198 ± 0.014***		*Initial $^{40}Ar/^{36}Ar$:*		*299.2 ± 7.9*	MSWD: 1.01
	Inverse isochron age *(of plateau steps) :*		***0.199 ± 0.014***		*Initial $^{40}Ar/^{36}Ar$:*		*299.4 ± 7.8*	MSWD: 1.02

Attachment 10: $^{40}Ar/^{39}Ar$ analytical results of Paka volcanics

Laser Output*	$^{40}Ar/^{39}Ar$	$^{37}Ar/^{39}Ar$	$^{36}Ar/^{39}Ar$ (x10^{-3})	K/Ca	$^{40}Ar^*$ (%)	$^{39}Ar_k$ (%)	$^{40}Ar^*/^{39}Ar_k$	Age(±1s) (Ma)
Sample ID: PK-9 (Trachyte Scoria and Pumice Lapilli Deposits)								
J= 0.000989		*Laboratory ID: C14064*		*Neutron Irradiation ID: PO-2*				
1.6%	232.867 ± 0.8603	0.2403 ± 0.0038	798.836 ± 4.059	2.4480	-1.4	2.0	-3.1707 ± -1.1232	-5.666 ± -2.010
2.0%	80.4312 ± 0.2380	0.0644 ± 0.0020	274.835 ± 0.909	9.1276	-1.0	4.4	-0.7776 ± -0.2287	-1.388 ± -0.408
2.2%	22.3888 ± 0.0671	0.0269 ± 0.0010	75.496 ± 0.299	21.8456	0.4	4.8	0.0819 ± 0.0859	0.146 ± 0.153
2.4%	10.5738 ± 0.0154	0.0233 ± 0.0007	35.141 ± 0.136	25.2683	1.8	5.4	0.1913 ± 0.0397	0.341 ± 0.071
2.7%	7.4807 ± 0.0095	0.0244 ± 0.0005	24.411 ± 0.105	24.1550	3.6	8.6	0.2692 ± 0.0306	0.480 ± 0.055
3.0%	4.7811 ± 0.0116	0.0267 ± 0.0003	15.448 ± 0.080	22.0499	4.6	9.5	0.2184 ± 0.0220	0.390 ± 0.039
3.3%	4.0104 ± 0.0085	0.0343 ± 0.0005	13.153 ± 0.106	17.1559	3.2	8.4	0.1264 ± 0.0307	0.225 ± 0.055
3.7%	3.5674 ± 0.0036	0.0467 ± 0.0005	11.522 ± 0.085	12.5882	4.7	12.0	0.1662 ± 0.0252	0.296 ± 0.045
4.1%	2.6993 ± 0.0054	0.0645 ± 0.0006	8.644 ± 0.060	9.1149	5.6	10.9	0.1501 ± 0.0175	0.268 ± 0.031
5.0%	2.1916 ± 0.0036	0.0849 ± 0.0004	6.906 ± 0.044	6.9277	7.2	25.6	0.1576 ± 0.0133	0.281 ± 0.024
5.4%	1.9239 ± 0.0040	0.0781 ± 0.0009	6.009 ± 0.077	7.5289	8.0	8.2	0.1543 ± 0.0229	0.275 ± 0.041
	***Plateau age** (Plateau: 4th to 11th step) :*		***0.303 ± 0.014***					
	Total gas age :		***0.107 ± 0.046***					
	***Normal isochron age** (of all steps) :*		***0.332 ± 0.018***		*Initial $^{40}Ar/^{36}Ar$:*		*293.9 ± 0.6*	MSWD: 2.09
	***Inverse isochron age** (of all steps) :*		***0.332 ± 0.017***		*Initial $^{40}Ar/^{36}Ar$:*		*294.0 ± 0.6*	MSWD: 2.11

Laser Output*	$^{40}Ar/^{39}Ar$	$^{37}Ar/^{39}Ar$	$^{36}Ar/^{39}Ar$ (x10^{-3})	K/Ca	$^{40}Ar^*$ (%)	$^{39}Ar_k$ (%)	$^{40}Ar^*/^{39}Ar_k$	Age(±1s) (Ma)
Sample ID: PK-10 (Secumius Trachytes)								
J= 0.000991		*Laboratory ID: C14065*		*Neutron Irradiation ID: PO-2*				
1.6%	120.782 ± 0.7039	0.1296 ± 0.0068	432.821 ± 4.135	4.5370	-5.9	0.5	-7.1074 ± -1.0099	12.752 ± -1.819
2.0%	13.0643 ± 0.0776	0.0647 ± 0.0008	44.491 ± 0.380	9.0921	-0.6	5.0	-0.0778 ± -0.1074	-0.139 ± -0.192
2.4%	2.42874 ± 0.0086	0.0496 ± 0.0007	7.746 ± 0.028	11.8645	5.9	13.0	0.1436 ± 0.0084	0.257 ± 0.015
2.4%	1.1786 ± 0.0031	0.0410 ± 0.0005	3.222 ± 0.026	14.3571	19.5	19.1	0.2298 ± 0.0080	0.411 ± 0.014
2.7%	0.7799 ± 0.0025	0.0409 ± 0.0005	1.832 ± 0.032	14.3662	31.0	19.9	0.2418 ± 0.0096	0.432 ± 0.017
3.3%	0.6299 ± 0.0024	0.0495 ± 0.0004	1.371 ± 0.026	11.8947	36.3	19.6	0.2286 ± 0.0080	0.409 ± 0.014
3.7%	0.6134 ± 0.0025	0.0757 ± 0.0003	1.374 ± 0.023	7.7751	34.8	22.9	0.2132 ± 0.0072	0.381 ± 0.013
	***Plateau age** (Plateau: 4th to 7th step) :*		***0.405 ± 0.007***					
	Total gas age :		***0.293 ± 0.015***					
	***Normal isochron age** (of plateau steps) :*		***0.385 ± 0.019***		*Initial $^{40}Ar/^{36}Ar$:*		*300.9 ± 5.2*	MSWD: 1.60
	***Inverse isochron age** (of plateau steps) :*		***0.387 ± 0.019***		*Initial $^{40}Ar/^{36}Ar$:*		*300.6 ± 5.3*	MSWD: 1.61

Attachment 10: $^{40}Ar/^{39}Ar$ analytical results of Paka volcanics

Laser Output*	$^{40}Ar/^{39}Ar$	$^{37}Ar/^{39}Ar$	$^{36}Ar/^{39}Ar$ (x10^{-3})	K/Ca	$^{40}Ar^*$ (%)	$^{39}Ar_k$ (%)	$^{40}Ar^*/^{39}Ar_k$	Age(±1s) (Ma)
Sample ID: PK-11 (Upper Basalts)								
J= *0.000992*		*Laboratory ID: C14066*			*Neutron Irradiation ID: PO-2*			
1.6%	16.2489 ± 0.1550	0.1663 ± 0.0017	55.894 ± 0.842	3.5375	-1.6	2.9	-0.2548 ± -0.2450	-0.456 ± -0.439
2.0%	3.5881 ± 0.0517	0.0601 ± 0.0020	10.766 ± 0.358	9.7936	11.5	4.3	0.4114 ± 0.1071	0.736 ± 0.192
2.4%	0.5483 ± 0.0028	0.0381 ± 0.0004	1.190 ± 0.036	15.4564	36.4	12.6	0.1997 ± 0.0108	0.357 ± 0.019
2.7%	0.3897 ± 0.0031	0.0294 ± 0.0005	0.610 ± 0.019	20.0154	54.3	15.0	0.2117 ± 0.0064	0.379 ± 0.012
3.0%	0.3761 ± 0.0026	0.0241 ± 0.0003	0.581 ± 0.014	24.3850	54.8	16.9	0.2063 ± 0.0049	0.369 ± 0.009
3.3%	0.3999 ± 0.0027	0.0237 ± 0.0003	0.659 ± 0.027	24.8486	51.8	12.2	0.2072 ± 0.0084	0.371 ± 0.015
3.7%	0.4396 ± 0.0024	0.0341 ± 0.0004	0.790 ± 0.034	17.2260	47.5	15.1	0.2089 ± 0.0103	0.374 ± 0.018
4.1%	0.4808 ± 0.0025	0.0732 ± 0.0004	0.957 ± 0.031	8.0394	42.4	11.2	0.2037 ± 0.0096	0.365 ± 0.017
4.6%	0.6505 ± 0.0028	0.1393 ± 0.0006	1.522 ± 0.024	4.2239	32.6	9.9	0.2118 ± 0.0074	0.379 ± 0.013
	Plateau age *(Plateau: 3rd to 9th step) :*		***0.372 ± 0.005***					
	Total gas age :		***0.362 ± 0.016***					
	Normal isochron age *(of plateau steps) :*		***0.377 ± 0.007***		*Initial $^{40}Ar/^{36}Ar$:*		*296.8 ± 8.7*	MSWD: 0.55
	Inverse isochron age *(of plateau steps) :*		***0.376 ± 0.007***		*Initial $^{40}Ar/^{36}Ar$:*		*296.9 ± 8.6*	MSWD: 0.55

Laser Output*	$^{40}Ar/^{39}Ar$	$^{37}Ar/^{39}Ar$	$^{36}Ar/^{39}Ar$ (x10^{-3})	K/Ca	$^{40}Ar^*$ (%)	$^{39}Ar_k$ (%)	$^{40}Ar^*/^{39}Ar_k$	Age(±1s) (Ma)
Sample ID: PK-12 (Upper Trachytes)								
J= *0.000992*		*Laboratory ID: C14067*			*Neutron Irradiation ID: PO-2*			
1.6%	205.291 ± 0.7046	0.0697 ± 0.0028	705.654 ± 2.681	8.4341	-1.6	1.9	-3.2242 ± -0.4214	-5.779 ± -0.757
2.0%	11.1154 ± 0.0226	0.0423 ± 0.0003	37.416 ± 0.171	13.9049	0.6	10.5	0.0623 ± 0.0503	0.111 ± 0.090
2.4%	2.5268 ± 0.0033	0.0328 ± 0.0002	8.490 ± 0.037	17.9474	0.8	22.6	0.0206 ± 0.0110	0.037 ± 0.020
2.7%	1.7705 ± 0.0035	0.0330 ± 0.0002	5.926 ± 0.036	17.8351	1.2	18.2	0.0219 ± 0.0106	0.039 ± 0.019
3.0%	1.8461 ± 0.0029	0.0329 ± 0.0003	6.182 ± 0.086	17.8783	1.2	16.0	0.0219 ± 0.0254	0.039 ± 0.045
3.4%	2.4686 ± 0.0038	0.0504 ± 0.0002	8.369 ± 0.055	11.6665	0.0	11.1	-0.0004 ± -0.0164	-0.001 ± -0.029
4.0%	3.3195 ± 0.0042	0.1320 ± 0.0003	11.112 ± 0.105	4.4549	1.4	12.4	0.0461 ± 0.0311	0.083 ± 0.056
4.7%	3.1663 ± 0.0047	0.2711 ± 0.0014	10.503 ± 0.048	2.1691	2.6	7.4	0.0838 ± 0.0142	0.150 ± 0.025
	Plateau age *(Plateau: 2nd to 8th step) :*		***0.055 ± 0.011***					
	Total gas age :		***-0.053 ± 0.021***					
	Normal isochron age *(of plateau steps) :*		***0.012 ± 0.026***		*Initial $^{40}Ar/^{36}Ar$:*		*298.3 ± 1.5*	MSWD: 1.80
	Inverse isochron age *(of plateau steps) :*		***0.012 ± 0.003***		*Initial $^{40}Ar/^{36}Ar$:*		*298.4 ± 1.6*	MSWD: 1.81

Attachment 10: $^{40}Ar/^{39}Ar$ analytical results of Paka volcanics

Laser Output*	$^{40}Ar/^{39}Ar$	$^{37}Ar/^{39}Ar$	$^{36}Ar/^{39}Ar$ (x10^{-3})	K/Ca	$^{40}Ar^{*}$ (%)	$^{39}Ar_{K}$ (%)	$^{40}Ar^{*}/^{39}Ar_{K}$	Age(±1s) (Ma)
Sample ID: PK-13 (Young Basalt)								
J= *0.000992*		*Laboratory ID: C14068*			*Neutron Irradiation ID: PO-2*			
1.6%	29.1089 ± 0.0649	1.9255 ± 0.0068	97.065 ± 0.744	0.3051	2.0	4.6	0.5773 ± 0.2112	1.033 ± 0.378
2.0%	1.7954 ± 0.0056	1.7818 ± 0.0068	6.368 ± 0.097	0.3297	2.9	26.4	0.0529 ± 0.0287	0.095 ± 0.051
2.4%	0.6121 ± 0.0033	1.4300 ± 0.0059	2.233 ± 0.061	0.4110	10.4	30.4	0.0639 ± 0.0183	0.114 ± 0.033
2.7%	1.0430 ± 0.0043	1.3354 ± 0.0101	3.390 ± 0.100	0.4401	13.9	13.6	0.1456 ± 0.0297	0.261 ± 0.053
3.2%	1.7518 ± 0.0051	1.5168 ± 0.0061	5.983 ± 0.213	0.3874	5.8	9.2	0.1023 ± 0.0629	0.183 ± 0.113
3.4%	1.7877 ± 0.0054	3.1795 ± 0.0118	6.553 ± 0.201	0.1846	5.6	9.4	0.0998 ± 0.0598	0.179 ± 0.107
4.0%	2.9178 ± 0.0086	5.4859 ± 0.0261	11.246 ± 0.211	0.1068	0.8	6.4	0.0229 ± 0.0628	0.041 ± 0.112
	Plateau age *(Plateau: 2nd to 6th step) :*		***0.145 ± 0.023***					
	Total gas age :		***0.179 ± 0.030***					
	Normal isochron age *(of plateau steps) :*		***0.134 ± 0.049***		*Initial $^{40}Ar/^{36}Ar$:*		*296.2 ± 7.5*	MSWD: 1.43
	Inverse isochron age *(of plateau steps) :*		***0.140 ± 0.036***		*Initial $^{40}Ar/^{36}Ar$:*		*296.3 ± 7.6*	MSWD: 1.50

Laser Output*	$^{40}Ar/^{39}Ar$	$^{37}Ar/^{39}Ar$	$^{36}Ar/^{39}Ar$ (x10^{-3})	K/Ca	$^{40}Ar^{*}$ (%)	$^{39}Ar_{K}$ (%)	$^{40}Ar^{*}/^{39}Ar_{K}$	Age(±1s) (Ma)
Sample ID: PK-14 (Upper Trachytes)								
J= *0.000990*		*Laboratory ID: C14069*			*Neutron Irradiation ID: PO-2*			
1.6%	163.451 ± 0.7685	0.1144 ± 0.0019	564.459 ± 2.911	5.1435	-2.0	2.6	-3.3386 ± -0.6243	-5.973 ± -1.119
2.0%	15.4004 ± 0.0439	0.0583 ± 0.0009	52.872 ± 0.277	10.0863	-1.4	9.3	-0.2187 ± -0.0782	-0.391 ± -0.140
2.3%	4.1215 ± 0.0149	0.0448 ± 0.0003	13.807 ± 0.077	13.1289	1.1	17.0	0.0452 ± 0.0228	0.081 ± 0.041
2.6%	1.8717 ± 0.0038	0.0384 ± 0.0005	6.127 ± 0.045	15.3002	3.4	17.5	0.0642 ± 0.0134	0.115 ± 0.024
3.0%	1.2678 ± 0.0030	0.0377 ± 0.0004	4.185 ± 0.049	15.5929	2.7	16.9	0.0341 ± 0.0145	0.061 ± 0.026
3.5%	1.4161 ± 0.0034	0.0480 ± 0.0004	4.650 ± 0.033	12.2671	3.2	16.1	0.0458 ± 0.0100	0.082 ± 0.018
4.1%	2.0893 ± 0.0049	0.1048 ± 0.0004	7.010 ± 0.045	5.6112	1.2	12.7	0.0261 ± 0.0133	0.047 ± 0.024
4.8%	3.0168 ± 0.0056	0.2371 ± 0.0012	9.992 ± 0.110	2.4802	2.7	7.9	0.0827 ± 0.0323	0.148 ± 0.058
	Plateau age *(Plateau: 3rd to 8th step) :*		***0.080 ± 0.011***					
	Total gas age :		***-0.118 ± 0.034***					
	Normal isochron age *(of plateau steps) :*		***0.070 ± 0.028***		*Initial $^{40}Ar/^{36}Ar$:*		*296.4 ± 2.4*	MSWD: 1.21
	Inverse isochron age *(of plateau steps) :*		***0.070 ± 0.020***		*Initial $^{40}Ar/^{36}Ar$:*		*296.4 ± 2.4*	MSWD: 1.21

Attachment 10: $^{40}Ar/^{39}Ar$ analytical results of Paka volcanics

Laser Output*	$^{40}Ar/^{39}Ar$	$^{37}Ar/^{39}Ar$	$^{36}Ar/^{39}Ar$ (x10^{-3})	K/Ca	$^{40}Ar^*$ (%)	$^{39}Ar_k$ (%)	$^{40}Ar^*/^{39}Ar_k$	Age(±1s) (Ma)
Sample ID: PK-15 (Lower Trachytes)								
J=	*0.000986*	*Laboratory ID: C14070*		*Neutron Irradiation ID: PO-2*				
1.6%	167.283 ± 0.6345	0.1857 ± 0.0020	578.596 ± 2.302	3.1680	-2.2	3.6	-3.6778 ± -0.3345	-6.554 ± -0.598
2.0%	32.8848 ± 0.1074	0.0923 ± 0.0023	113.796 ± 0.429	6.3757	-2.2	12.1	-0.7346 ± -0.1137	-1.307 ± -0.202
2.3%	12.1404 ± 0.0276	0.0694 ± 0.0015	41.282 ± 0.260	8.4720	-0.4	18.1	-0.0529 ± -0.0752	-0.094 ± -0.134
2.6%	9.60929 ± 0.0101	0.0605 ± 0.0004	32.306 ± 0.096	9.7224	0.7	18.8	0.0676 ± 0.0277	0.120 ± 0.049
2.9%	10.2900 ± 0.0183	0.0522 ± 0.0006	34.458 ± 0.129	11.2594	1.1	16.3	0.1118 ± 0.0349	0.199 ± 0.062
3.2%	13.0868 ± 0.0176	0.0522 ± 0.0004	44.151 ± 0.175	11.2594	0.3	13.0	0.0441 ± 0.0496	0.078 ± 0.088
3.5%	16.0174 ± 0.0167	0.0769 ± 0.0009	54.362 ± 0.098	7.6514	-0.3	9.6	-0.0406 ± -0.0257	-0.072 ± -0.046
3.9%	18.4422 ± 0.0222	0.1812 ± 0.0009	61.352 ± 0.183	3.2468	1.8	8.7	0.3270 ± 0.0511	0.581 ± 0.091
	Plateau age *(Plateau: 4th to 6th step) :*		***0.139 ± 0.035***					
	Total gas age :		***-0.299 ± 0.045***					
	Normal isochron age *(of plateau steps) :*		***0.281 ± 0.296***		*Initial $^{40}Ar/^{36}Ar$:*		*293.2 ± 4.7*	MSWD: 1.14
	Inverse isochron age *(of plateau steps) :*		***0.281 ± 0.188***		*Initial $^{40}Ar/^{36}Ar$:*		*293.2 ± 4.7*	MSWD: 1.14

Laser Output*	$^{40}Ar/^{39}Ar$	$^{37}Ar/^{39}Ar$	$^{36}Ar/^{39}Ar$ (x10^{-3})	K/Ca	$^{40}Ar^*$ (%)	$^{39}Ar_k$ (%)	$^{40}Ar^*/^{39}Ar_k$	Age(±1s) (Ma)
Sample ID: PK-16 (Lower Trachytes)								
J=	*0.000982*	*Laboratory ID: C14071*		*Neutron Irradiation ID: PO-2*				
1.6%	34.0403 ± 0.3128	0.1646 ± 0.0027	119.152 ± 1.410	3.5743	-3.4	1.6	-1.1563 ± -0.4068	-2.050 ± -0.722
2.0%	2.93021 ± 0.0267	0.0705 ± 0.0018	9.578 ± 0.160	8.3457	3.6	5.3	0.1055 ± 0.0477	0.187 ± 0.084
2.3%	0.941 ± 0.0043	0.0522 ± 0.0007	2.689 ± 0.055	11.2702	16.0	10.6	0.1504 ± 0.0163	0.267 ± 0.029
2.6%	0.61808 ± 0.0029	0.0404 ± 0.0004	1.340 ± 0.035	14.5613	36.5	16.3	0.2254 ± 0.0107	0.399 ± 0.019
2.9%	0.5137 ± 0.0024	0.0334 ± 0.0004	1.021 ± 0.011	17.6360	41.8	19.7	0.2147 ± 0.0041	0.380 ± 0.007
3.2%	0.4572 ± 0.0025	0.0323 ± 0.0003	0.828 ± 0.022	18.1836	47.0	16.4	0.2151 ± 0.0068	0.381 ± 0.012
3.6%	0.4345 ± 0.0026	0.0509 ± 0.0005	0.692 ± 0.031	11.5486	53.9	12.6	0.2340 ± 0.0096	0.415 ± 0.017
4.2%	0.4683 ± 0.0025	0.1545 ± 0.0011	0.897 ± 0.037	3.8059	46.0	11.8	0.2155 ± 0.0110	0.382 ± 0.020
4.8%	0.5084 ± 0.0032	0.1739 ± 0.0014	0.989 ± 0.071	3.3824	45.2	5.7	0.2298 ± 0.0213	0.407 ± 0.038
	Plateau age *(Plateau: 4th to 9th step) :*		***0.386 ± 0.005***					
	Total gas age :		***0.329 ± 0.014***					
	Normal isochron age *(of plateau steps) :*		***0.389 ± 0.034***		*Initial $^{40}Ar/^{36}Ar$:*		*293.4 ± 19.6*	MSWD: 1.01
	Inverse isochron age *(of plateau steps) :*		***0.394 ± 0.031***		*Initial $^{40}Ar/^{36}Ar$:*		*291.0 ± 19*	MSWD: 1.06

Attachment 10: $^{40}Ar/^{39}Ar$ analytical results of Paka volcanics

Laser Output*	$^{40}Ar/^{39}Ar$	$^{37}Ar/^{39}Ar$	$^{36}Ar/^{39}Ar$ (x10^{-3})	K/Ca	$^{40}Ar^*$ (%)	$^{39}Ar_K$ (%)	$^{40}Ar^*/^{39}Ar_K$	Age(±1s) (Ma)
Sample ID: PK-17 (Late Pyroclastic Deposits)								
J=	*0.000990*	*Laboratory ID: C14072*		*Neutron Irradiation ID: PO-2*				
1.6%	211.764 ± 0.7276	0.1223 ± 0.0050	714.757 ± 5.801	4.8094	0.3	4.5	0.5626 ± 1.5877	1.005 ± 2.834
2.0%	179.12 ± 0.4665	0.0366 ± 0.0053	604.779 ± 2.208	16.0696	0.2	9.9	0.4110 ± 0.4879	0.734 ± 0.871
2.2%	83.7469 ± 0.2048	0.0175 ± 0.0021	282.221 ± 1.952	33.5753	0.4	8.6	0.3521 ± 0.5467	0.629 ± 0.976
2.4%	26.7536 ± 0.0417	0.0304 ± 0.0011	89.457 ± 0.472	19.3285	1.2	3.3	0.3216 ± 0.1351	0.574 ± 0.241
2.7%	44.3627 ± 0.0857	0.0461 ± 0.0012	148.424 ± 0.416	12.7603	1.1	10.0	0.5069 ± 0.1089	0.905 ± 0.194
3.1%	13.5805 ± 0.0239	0.0758 ± 0.0008	45.546 ± 0.268	7.7618	0.9	6.3	0.1275 ± 0.0781	0.228 ± 0.140
3.3%	9.6427 ± 0.0150	0.0657 ± 0.0009	32.694 ± 0.184	8.9557	-0.1	4.3	-0.0134 ± -0.0542	-0.024 ± -0.097
3.7%	9.8509 ± 0.0108	0.0810 ± 0.0005	33.208 ± 0.171	7.2653	0.4	15.5	0.0442 ± 0.0502	0.079 ± 0.090
4.0%	6.7896 ± 0.0128	0.0725 ± 0.0005	22.826 ± 0.124	8.1118	0.7	14.7	0.0501 ± 0.0351	0.090 ± 0.063
4.4%	5.7276 ± 0.0092	0.0792 ± 0.0006	19.139 ± 0.150	7.4299	1.4	14.3	0.0781 ± 0.0443	0.140 ± 0.079
4.8%	5.1695 ± 0.0095	0.0760 ± 0.0006	17.463 ± 0.129	7.7386	0.3	8.4	0.0150 ± 0.0379	0.027 ± 0.068
	Plateau age *(Plateau: 6th to 11th step) :*		***0.076 ± 0.033***					
	Total gas age *:*		***0.344 ± 0.179***					
	Normal isochron age *(of plateau steps) :*		***0.031 ± 0.111***		*Initial $^{40}Ar/^{36}Ar$:*		*296.5 ± 2.4*	MSWD: 0.91
	Inverse isochron age *(of plateau steps) :*		***0.031 ± 0.017***		*Initial $^{40}Ar/^{36}Ar$:*		*296.5 ± 2.4*	MSWD: 0.91

Laser Output*	$^{40}Ar/^{39}Ar$	$^{37}Ar/^{39}Ar$	$^{36}Ar/^{39}Ar$ (x10^{-3})	K/Ca	$^{40}Ar^*$ (%)	$^{39}Ar_K$ (%)	$^{40}Ar^*/^{39}Ar_K$	Age(±1s) (Ma)
Sample ID: PK-18 (Upper Trachytes)								
J=	*0.000990*	*Laboratory ID: C14073*		*Neutron Irradiation ID: PO-2*				
1.6%	51.2128 ± 0.3268	0.1788 ± 0.0034	178.911 ± 2.342	3.2900	-3.2	2.8	-1.6415 ± -0.6861	-2.934 ± -1.227
2.0%	19.5231 ± 0.1479	0.1121 ± 0.0012	64.682 ± 0.810	5.2458	2.1	5.6	0.4183 ± 0.2381	0.747 ± 0.425
2.3%	4.25905 ± 0.0134	0.0743 ± 0.0011	13.987 ± 0.082	7.9179	3.1	10.9	0.1316 ± 0.0243	0.235 ± 0.043
2.6%	2.14051 ± 0.0063	0.0669 ± 0.0005	6.587 ± 0.070	8.7944	9.3	14.0	0.1992 ± 0.0209	0.356 ± 0.037
2.9%	1.52112 ± 0.0049	0.0627 ± 0.0008	4.488 ± 0.046	9.3829	13.1	18.2	0.1997 ± 0.0140	0.357 ± 0.025
3.2%	1.5415 ± 0.0031	0.0651 ± 0.0004	4.501 ± 0.024	9.0307	14.0	13.2	0.2165 ± 0.0075	0.387 ± 0.014
3.6%	1.6025 ± 0.0029	0.0789 ± 0.0004	4.756 ± 0.036	7.4533	12.7	12.7	0.2033 ± 0.0109	0.363 ± 0.019
4.1%	1.5665 ± 0.0034	0.1613 ± 0.0007	4.591 ± 0.034	3.6465	14.2	12.6	0.2224 ± 0.0103	0.397 ± 0.018
4.7%	1.6966 ± 0.0031	0.2413 ± 0.0018	5.047 ± 0.043	2.4376	13.2	10.0	0.2242 ± 0.0128	0.400 ± 0.023
	Plateau age *(Plateau: 4th to 9th step) :*		***0.382 ± 0.008***					
	Total gas age *:*		***0.289 ± 0.042***					
	Normal isochron age *(of plateau steps) :*		***0.417 ± 0.084***		*Initial $^{40}Ar/^{36}Ar$:*		*291.2 ± 9.9*	MSWD: 0.97
	Inverse isochron age *(of plateau steps) :*		***0.418 ± 0.077***		*Initial $^{40}Ar/^{36}Ar$:*		*291.2 ± 10*	MSWD: 0.97

Attachment 10: $^{40}Ar/^{39}Ar$ analytical results of Paka volcanics

Laser Output*	$^{40}Ar/^{39}Ar$	$^{37}Ar/^{39}Ar$	$^{36}Ar/^{39}Ar$ (x10^{-3})	K/Ca	$^{40}Ar^{*}$ (%)	$^{39}Ar_{K}$ (%)	$^{40}Ar^{*}/^{39}Ar_{K}$	Age(±1s) (Ma)
Sample ID: PK-19 (Upper Trachytes)								
J= 0.000989		*Laboratory ID: C14074*			*Neutron Irradiation ID: PO-2*			
1.6%	292.096 ± 2.9981	0.1477 ± 0.0129	1008.694 ± 15.075	3.9827	-2.0	2.6	-5.9625 ± -3.4296	10.670 ± -6.156
2.0%	110.035 ± 0.4467	0.0518 ± 0.0024	378.138 ± 2.049	11.3549	-1.5	4.1	-1.7010 ± -0.4819	-3.038 ± -0.861
2.3%	34.0251 ± 0.0983	0.0326 ± 0.0013	117.785 ± 0.595	18.0697	-2.3	7.0	-0.7779 ± -0.1540	-1.388 ± -0.275
2.5%	19.8279 ± 0.0339	0.0276 ± 0.0014	67.027 ± 0.761	21.2878	0.1	8.4	0.0236 ± 0.2231	0.042 ± 0.398
2.7%	14.4652 ± 0.0357	0.0273 ± 0.0003	47.890 ± 0.251	21.5524	2.2	10.5	0.3158 ± 0.0693	0.563 ± 0.124
2.9%	12.2095 ± 0.0237	0.0284 ± 0.0006	40.528 ± 0.175	20.6794	1.9	10.5	0.2357 ± 0.0494	0.420 ± 0.088
3.1%	10.2150 ± 0.0262	0.0294 ± 0.0005	33.239 ± 0.155	20.0286	3.9	10.9	0.3953 ± 0.0431	0.705 ± 0.077
3.4%	9.5894 ± 0.0154	0.0432 ± 0.0004	31.152 ± 0.128	13.6195	4.0	13.1	0.3874 ± 0.0372	0.691 ± 0.066
3.7%	9.1550 ± 0.0124	0.0839 ± 0.0004	29.822 ± 0.170	7.0092	3.8	14.4	0.3491 ± 0.0490	0.623 ± 0.088
4.0%	12.7261 ± 0.0193	0.1019 ± 0.0009	41.512 ± 0.214	5.7740	3.7	7.9	0.4672 ± 0.0613	0.833 ± 0.109
4.5%	11.2619 ± 0.0134	0.1846 ± 0.0011	36.705 ± 0.236	3.1865	3.8	6.2	0.4300 ± 0.0692	0.767 ± 0.123
5.0%	10.6842 ± 0.0323	0.2178 ± 0.0017	34.764 ± 0.327	2.7004	4.0	4.3	0.4284 ± 0.0958	0.764 ± 0.171
	Plateau age *(Plateau: 5th to 12th step) :*		***0.415 ± 0.028***					
	Total gas age :		***-0.175 ± 0.168***					
	Normal isochron age *(of plateau steps) :*		***0.524 ± 0.226***		*Initial $^{40}Ar/^{36}Ar$:*		*293.7 ± 3.6*	MSWD: 0.26
	Inverse isochron age *(of plateau steps) :*		***0.524 ± 0.222***		*Initial $^{40}Ar/^{36}Ar$:*		*293.7 ± 3.6*	MSWD: 0.26

Laser Output*	$^{40}Ar/^{39}Ar$	$^{37}Ar/^{39}Ar$	$^{36}Ar/^{39}Ar$ (x10^{-3})	K/Ca	$^{40}Ar^{*}$ (%)	$^{39}Ar_{K}$ (%)	$^{40}Ar^{*}/^{39}Ar_{K}$	Age(±1s) (Ma)
Sample ID: PK-20 (Lower Basalts)								
J= 0.000989		*Laboratory ID: C14075*			*Neutron Irradiation ID: PO-2*			
1.6%	54.806 ± 0.3132	1.7099 ± 0.0243	190.067 ± 2.039	0.3436	-2.2	3.8	-1.2268 ± -0.5453	-2.190 ± -0.974
2.0%	8.34703 ± 0.0571	1.9712 ± 0.0299	29.783 ± 0.510	0.2980	-3.6	10.3	-0.3004 ± -0.1454	-0.536 ± -0.260
2.4%	3.0040 ± 0.0128	1.6907 ± 0.0080	10.131 ± 0.252	0.3475	4.7	17.2	0.1425 ± 0.0743	0.254 ± 0.133
2.7%	2.0404 ± 0.0113	1.5858 ± 0.0144	6.267 ± 0.264	0.3705	15.3	15.3	0.3127 ± 0.0779	0.558 ± 0.139
3.1%	1.8521 ± 0.0103	1.5481 ± 0.0094	5.769 ± 0.233	0.3796	14.5	14.3	0.2684 ± 0.0691	0.479 ± 0.123
3.6%	1.5629 ± 0.0068	1.5435 ± 0.0142	4.582 ± 0.208	0.3807	21.1	14.8	0.3297 ± 0.0616	0.588 ± 0.110
4.1%	1.6531 ± 0.0090	2.5926 ± 0.0162	5.241 ± 0.223	0.2265	18.6	15.3	0.3074 ± 0.0663	0.548 ± 0.118
4.6%	1.7272 ± 0.0121	3.3044 ± 0.0416	6.353 ± 0.567	0.1776	6.2	9.1	0.1080 ± 0.1678	0.193 ± 0.299
	Plateau age *(Plateau: 4th to 7th step) :*		***0.545 ± 0.061***					
	Total gas age :		***0.248 ± 0.068***					
	Normal isochron age *(of all steps) :*		***0.572 ± 0.062***		*Initial $^{40}Ar/^{36}Ar$:*		*283.9 ± 2.6*	MSWD: 1.26
	Inverse isochron age *(of all steps) :*		***0.582 ± 0.058***		*Initial $^{40}Ar/^{36}Ar$:*		*284.1 ± 2.6*	MSWD: 1.24

Attachment 10: $^{40}Ar/^{39}Ar$ analytical results of Paka volcanics

Laser Output*	$^{40}Ar/^{39}Ar$	$^{37}Ar/^{39}Ar$	$^{36}Ar/^{39}Ar$ ($x10^{-3}$)	K/Ca	$^{40}Ar^*$ (%)	$^{39}Ar_k$ (%)	$^{40}Ar^*/^{39}Ar_k$	Age(±1s) (Ma)
Sample ID: PK-21 (Lower Trachytes)								
J=	*0.000981*	*Laboratory ID: C14076*		*Neutron Irradiation ID: PO-2*				
1.6%	107.503 ± 0.6679	0.2662 ± 0.0075	372.748 ± 3.612	2.2090	-2.4	0.6	-2.6238 ± -0.9491	-4.650 ± -1.684
2.0%	8.80088 ± 0.0598	0.0451 ± 0.0008	29.634 ± 0.343	13.0551	0.5	4.4	0.0474 ± 0.1009	0.084 ± 0.178
2.3%	3.6020 ± 0.0129	0.0312 ± 0.0009	12.011 ± 0.143	18.8820	1.5	9.3	0.0553 ± 0.0420	0.098 ± 0.074
2.6%	2.4446 ± 0.0041	0.0243 ± 0.0006	7.684 ± 0.058	24.2027	7.2	14.6	0.1757 ± 0.0172	0.311 ± 0.030
2.9%	2.2346 ± 0.0076	0.0241 ± 0.0003	6.959 ± 0.066	24.4005	8.1	13.9	0.1800 ± 0.0195	0.318 ± 0.035
3.3%	2.0159 ± 0.0059	0.0320 ± 0.0004	6.177 ± 0.054	18.3946	9.6	18.2	0.1930 ± 0.0155	0.341 ± 0.027
3.7%	2.0743 ± 0.0041	0.0652 ± 0.0011	6.438 ± 0.043	9.0189	8.5	18.2	0.1768 ± 0.0130	0.313 ± 0.023
4.1%	2.9656 ± 0.0057	0.1329 ± 0.0019	9.498 ± 0.097	4.4272	5.7	10.5	0.1693 ± 0.0287	0.300 ± 0.051
4.7%	3.6716 ± 0.0120	0.1644 ± 0.0019	11.682 ± 0.163	3.5786	6.3	6.1	0.2325 ± 0.0476	0.411 ± 0.084
5.3%	4.0685 ± 0.0094	0.1783 ± 0.0020	13.252 ± 0.171	3.2995	4.1	4.2	0.1665 ± 0.0501	0.295 ± 0.089
	Plateau age *(Plateau: 4th to 10th step) :*		***0.321 ± 0.013***					
	Total gas age :		***0.261 ± 0.019***					
	Normal isochron age *(of plateau steps) :*		***0.322 ± 0.066***		*Initial $^{40}Ar/^{36}Ar$:*		*295.4 ± 5.1*	MSWD: 0.66
	Inverse isochron age *(of plateau steps) :*		***0.321 ± 0.063***		*Initial $^{40}Ar/^{36}Ar$:*		*295.5 ± 5.1*	MSWD: 0.67

Laser Output*	$^{40}Ar/^{39}Ar$	$^{37}Ar/^{39}Ar$	$^{36}Ar/^{39}Ar$ ($x10^{-3}$)	K/Ca	$^{40}Ar^*$ (%)	$^{39}Ar_k$ (%)	$^{40}Ar^*/^{39}Ar_k$	Age(±1s) (Ma)
Sample ID: PK-22 (Mugearites)								
J=	*0.000995*	*Laboratory ID: C14077*		*Neutron Irradiation ID: PO-2*				
1.6%	8.25587 ± 0.2155	0.2703 ± 0.0088	28.786 ± 0.906	2.1762	-2.8	3.4	-0.2292 ± -0.2636	-0.412 ± -0.473
2.0%	2.302 ± 0.0334	0.2637 ± 0.0056	6.960 ± 0.232	2.2300	11.5	6.1	0.2659 ± 0.0690	0.477 ± 0.124
2.3%	0.67526 ± 0.0107	0.2161 ± 0.0039	1.523 ± 0.069	2.7213	35.9	11.3	0.2421 ± 0.0215	0.435 ± 0.039
2.6%	0.50017 ± 0.0030	0.1920 ± 0.0020	0.872 ± 0.051	3.0633	51.5	17.0	0.2575 ± 0.0153	0.462 ± 0.027
2.9%	0.48976 ± 0.0041	0.1845 ± 0.0028	0.806 ± 0.049	3.1877	54.3	14.6	0.2660 ± 0.0149	0.477 ± 0.027
3.3%	0.5321 ± 0.0033	0.1962 ± 0.0017	1.051 ± 0.072	2.9973	44.5	13.9	0.2370 ± 0.0215	0.425 ± 0.039
3.7%	0.5354 ± 0.0036	0.2281 ± 0.0022	0.916 ± 0.076	2.5789	52.7	12.9	0.2825 ± 0.0225	0.507 ± 0.040
4.1%	0.5442 ± 0.0031	0.2970 ± 0.0032	0.939 ± 0.090	1.9799	53.3	10.8	0.2899 ± 0.0267	0.520 ± 0.048
4.7%	0.5465 ± 0.0038	0.4278 ± 0.0035	1.036 ± 0.067	1.3746	50.1	10.0	0.2738 ± 0.0200	0.491 ± 0.036
	Plateau age *(Plateau: 2nd to 9th step) :*		***0.471 ± 0.013***					
	Total gas age :		***0.443 ± 0.021***					
	Normal isochron age *(of plateau steps) :*		***0.470 ± 0.024***		*Initial $^{40}Ar/^{36}Ar$:*		*293.8 ± 11*	MSWD: 0.87
	Inverse isochron age *(of plateau steps) :*		***0.475 ± 0.023***		*Initial $^{40}Ar/^{36}Ar$:*		*293.7 ± 11*	MSWD: 0.88

Attachment 10: $^{40}Ar/^{39}Ar$ analytical results of Paka volcanics

Laser Output*	$^{40}Ar/^{39}Ar$	$^{37}Ar/^{39}Ar$	$^{36}Ar/^{39}Ar$ (x10^{-3})	K/Ca	$^{40}Ar^*$ (%)	$^{39}Ar_K$ (%)	$^{40}Ar^*/^{39}Ar_K$	Age(±1s) (Ma)
Sample ID: PK-23 (Upper Trachytes)								
J= 0.000996		*Laboratory ID: C14078*			*Neutron Irradiation ID: PO-2*			
1.6%	55.3176 ± 0.2685	0.2387 ± 0.0038	189.012 ± 1.460	2.4642	-0.9	1.8	-0.5170 ± -0.4154	-0.929 ± -0.747
2.0%	24.7548 ± 0.2164	0.0874 ± 0.0027	86.551 ± 1.029	6.7317	-3.3	3.9	-0.8142 ± -0.2999	-1.464 ± -0.539
2.3%	6.0266 ± 0.0366	0.0248 ± 0.0008	20.381 ± 0.182	23.6942	0.1	6.5	0.0059 ± 0.0537	0.011 ± 0.096
2.6%	2.0422 ± 0.0173	0.0168 ± 0.0006	6.386 ± 0.127	34.9695	7.7	9.2	0.1566 ± 0.0377	0.281 ± 0.068
2.9%	1.0710 ± 0.0083	0.0117 ± 0.0005	2.801 ± 0.061	50.2851	22.8	11.2	0.2441 ± 0.0184	0.438 ± 0.033
3.2%	0.6769 ± 0.0032	0.0122 ± 0.0006	1.514 ± 0.051	48.1642	34.0	10.3	0.2304 ± 0.0154	0.414 ± 0.028
3.6%	0.6900 ± 0.0031	0.0170 ± 0.0002	1.573 ± 0.062	34.6936	32.8	11.9	0.2265 ± 0.0183	0.407 ± 0.033
4.0%	0.8442 ± 0.0040	0.0374 ± 0.0007	2.182 ± 0.093	15.7209	24.0	10.6	0.2023 ± 0.0275	0.363 ± 0.050
4.6%	1.2261 ± 0.0038	0.0816 ± 0.0014	3.405 ± 0.061	7.2057	18.5	11.1	0.2262 ± 0.0181	0.406 ± 0.033
5.2%	1.5568 ± 0.0061	0.1152 ± 0.0013	4.489 ± 0.046	5.1042	15.4	12.3	0.2393 ± 0.0137	0.430 ± 0.025
5.8%	1.6192 ± 0.0059	0.1216 ± 0.0011	4.547 ± 0.064	4.8385	17.6	11.2	0.2852 ± 0.0191	0.512 ± 0.034
	Plateau age *(Plateau: 5th to 11th step) :*		***0.428 ± 0.012***					
	Total gas age :		***0.287 ± 0.028***					
	Normal isochron age *(of plateau steps) :*		***0.373 ± 0.033***		*Initial $^{40}Ar/^{39}Ar$:*		*305.3 ± 5.6*	MSWD: 1.05
	Inverse isochron age *(of plateau steps) :*		***0.374 ± 0.032***		*Initial $^{40}Ar/^{36}Ar$:*		*305.4 ± 5.6*	MSWD: 1.06

Laser Output*	$^{40}Ar/^{39}Ar$	$^{37}Ar/^{39}Ar$	$^{36}Ar/^{39}Ar$ (x10^{-3})	K/Ca	$^{40}Ar^*$ (%)	$^{39}Ar_K$ (%)	$^{40}Ar^*/^{39}Ar_K$	Age(±1s) (Ma)
Sample ID: PK-24 (Mugearites)								
J= 0.000995		*Laboratory ID: C14079*			*Neutron Irradiation ID: PO-2*			
1.6%	45.5237 ± 0.3539	0.2966 ± 0.0085	159.568 ± 1.335	1.9828	-3.5	1.2	-1.6058 ± -0.3496	-2.885 ± -0.629
2.0%	19.4216 ± 0.2388	0.2291 ± 0.0064	65.484 ± 1.349	2.5671	0.5	3.5	0.0889 ± 0.3954	0.160 ± 0.710
2.3%	5.69422 ± 0.0466	0.1856 ± 0.0043	19.408 ± 0.291	3.1690	-0.5	7.0	-0.0263 ± -0.0853	-0.047 ± -0.153
2.6%	2.85526 ± 0.0064	0.1631 ± 0.0025	9.418 ± 0.210	3.6065	3.0	10.6	0.0851 ± 0.0618	0.153 ± 0.111
2.9%	1.9017 ± 0.0196	0.1569 ± 0.0028	5.866 ± 0.117	3.7487	9.5	12.7	0.1806 ± 0.0352	0.324 ± 0.063
3.2%	1.7189 ± 0.0049	0.1651 ± 0.0032	5.252 ± 0.115	3.5623	10.5	13.5	0.1797 ± 0.0339	0.323 ± 0.061
3.5%	1.3002 ± 0.0061	0.1636 ± 0.0019	3.728 ± 0.076	3.5942	16.3	12.7	0.2113 ± 0.0224	0.379 ± 0.040
3.9%	1.1202 ± 0.0047	0.1639 ± 0.0014	3.111 ± 0.063	3.5883	19.1	21.0	0.2137 ± 0.0186	0.384 ± 0.033
4.3%	0.7586 ± 0.0050	0.1759 ± 0.0012	1.777 ± 0.040	3.3443	32.6	17.8	0.2473 ± 0.0122	0.444 ± 0.022
	Plateau age *(Plateau: 5th to 9th step) :*		***0.406 ± 0.016***					
	Total gas age :		***0.275 ± 0.034***					
	Normal isochron age *(of all steps) :*		***0.464 ± 0.018***		*Initial $^{40}Ar/^{36}Ar$:*		*283.3 ± 1.8*	MSWD: 0.86
	Inverse isochron age *(of all steps) :*		***0.464 ± 0.018***		*Initial $^{40}Ar/^{36}Ar$:*		*283.4 ± 1.8*	MSWD: 0.87

Attachment 10: $^{40}Ar/^{39}Ar$ analytical results of Paka volcanics

Laser Output*	$^{40}Ar/^{39}Ar$	$^{37}Ar/^{39}Ar$	$^{36}Ar/^{39}Ar$ (x10^{-3})	K/Ca	$^{40}Ar^{*}$ (%)	$^{39}Ar_{K}$ (%)	$^{40}Ar^{*}/^{39}Ar_{K}$	Age(±1s) (Ma)
Sample ID: PK-25 (Upper Trachytes)								
J= *0.000994*		*Laboratory ID: C14080*			*Neutron Irradiation ID: PO-2*			
1.6%	238.89 ± 1.9449	0.1147 ± 0.0100	832.855 ± 8.317	5.1300	-3.0	1.0	-7.2104 ± -1.7578	12.977 ± -3.175
2.0%	28.0945 ± 0.0913	0.0728 ± 0.0012	97.286 ± 0.479	8.0771	-2.3	3.9	-0.6478 ± -0.1286	-1.162 ± -0.231
2.3%	6.33304 ± 0.0241	0.0512 ± 0.0009	21.790 ± 0.127	11.4908	-1.6	8.2	-0.1019 ± -0.0370	-0.183 ± -0.066
2.6%	3.37639 ± 0.0083	0.0432 ± 0.0011	11.392 ± 0.051	13.6203	0.4	12.1	0.0135 ± 0.0147	0.024 ± 0.026
2.9%	2.31541 ± 0.0060	0.0380 ± 0.0004	7.853 ± 0.051	15.4685	-0.1	12.3	-0.0022 ± -0.0146	-0.004 ± -0.026
3.2%	1.80165 ± 0.0057	0.0387 ± 0.0005	6.150 ± 0.080	15.1811	-0.7	12.8	-0.0127 ± -0.0236	-0.023 ± -0.042
3.5%	1.5062 ± 0.0036	0.0371 ± 0.0003	5.158 ± 0.063	15.8544	-1.0	12.2	-0.0150 ± -0.0186	-0.027 ± -0.033
3.9%	1.2683 ± 0.0039	0.0514 ± 0.0007	4.157 ± 0.037	11.4402	3.5	13.0	0.0440 ± 0.0113	0.079 ± 0.020
4.4%	1.1793 ± 0.0033	0.0941 ± 0.0011	3.902 ± 0.060	6.2537	2.9	13.0	0.0337 ± 0.0179	0.061 ± 0.032
5.0%	1.0294 ± 0.0046	0.1303 ± 0.0013	3.422 ± 0.043	4.5155	2.8	11.4	0.0284 ± 0.0127	0.051 ± 0.023
	Plateau age *(Plateau: 4th to 10th step) :*		***0.035 ± 0.010***					
	Total gas age :		***-0.171 ± 0.035***					
	Normal isochron age *(of plateau steps) :*		***0.070 ± 0.024***		*Initial $^{40}Ar/^{36}Ar$:*		*292.0 ± 2*	MSWD: 1.47
	Inverse isochron age *(of plateau steps) :*		***0.072 ± 0.016***		*Initial $^{40}Ar/^{36}Ar$:*		*292.0 ± 2*	MSWD: 1.46

Laser Output*	$^{40}Ar/^{39}Ar$	$^{37}Ar/^{39}Ar$	$^{36}Ar/^{39}Ar$ (x10^{-3})	K/Ca	$^{40}Ar^{*}$ (%)	$^{39}Ar_{K}$ (%)	$^{40}Ar^{*}/^{39}Ar_{K}$	Age(±1s) (Ma)
Sample ID: PK-26 (Upper Basalts)								
J= *0.000987*		*Laboratory ID: C14081*			*Neutron Irradiation ID: PO-2*			
1.6%	18.6693 ± 0.0602	0.0969 ± 0.0013	65.706 ± 0.404	6.0713	-4.0	5.3	-0.7394 ± -0.1138	-1.317 ± -0.203
2.0%	8.3330 ± 0.0797	0.1041 ± 0.0022	27.931 ± 0.580	5.6519	1.1	5.1	0.0876 ± 0.1703	0.156 ± 0.303
2.3%	1.4731 ± 0.0176	0.0694 ± 0.0012	4.592 ± 0.095	8.4768	8.2	9.7	0.1214 ± 0.0284	0.216 ± 0.051
2.6%	0.4122 ± 0.0035	0.0585 ± 0.0010	1.145 ± 0.033	10.0562	19.0	13.8	0.0783 ± 0.0100	0.139 ± 0.018
2.9%	0.2980 ± 0.0025	0.0501 ± 0.0006	0.749 ± 0.025	11.7342	27.0	11.5	0.0805 ± 0.0078	0.143 ± 0.014
3.3%	0.2739 ± 0.0027	0.0447 ± 0.0006	0.645 ± 0.027	13.1643	31.6	16.3	0.0867 ± 0.0084	0.154 ± 0.015
3.7%	0.2775 ± 0.0024	0.0532 ± 0.0008	0.666 ± 0.030	11.0554	30.6	15.4	0.0849 ± 0.0090	0.151 ± 0.016
3.9%	0.3141 ± 0.0026	0.0945 ± 0.0009	0.785 ± 0.025	6.2276	28.5	10.6	0.0896 ± 0.0078	0.160 ± 0.014
4.4%	0.3242 ± 0.0024	0.1192 ± 0.0008	0.851 ± 0.031	4.9339	25.3	12.2	0.0821 ± 0.0095	0.146 ± 0.017
	Plateau age *(Plateau: 4th to 9th step) :*		***0.150 ± 0.006***					
	Total gas age :		***0.078 ± 0.020***					
	Normal isochron age *(of plateau steps) :*		***0.168 ± 0.032***		*Initial $^{40}Ar/^{36}Ar$:*		*281.7 ± 22.7*	MSWD: 0.46
	Inverse isochron age *(of plateau steps) :*		***0.169 ± 0.031***		*Initial $^{40}Ar/^{36}Ar$:*		*281.6 ± 22.8*	MSWD: 0.46

Attachment 10: $^{40}Ar/^{39}Ar$ analytical results of Paka volcanics

Laser Output*	$^{40}Ar/^{39}Ar$	$^{37}Ar/^{39}Ar$	$^{36}Ar/^{39}Ar$ (x10^{-3})	K/Ca	$^{40}Ar^*$ (%)	$^{39}Ar_k$ (%)	$^{40}Ar^*/^{39}Ar_k$	Age(±1s) (Ma)
Sample ID: PK-27 (Upper Trachytes)								
J= 0.000984		*Laboratory ID: C14082*		*Neutron Irradiation ID: PO-2*				
1.6%	139.898 ± 1.1673	0.0905 ± 0.0027	487.797 ± 5.774	6.5012	-3.0	1.5	-4.2388 ± -1.2584	-7.541 ± -2.243
2.0%	62.5511 ± 0.2685	0.0495 ± 0.0034	214.184 ± 1.819	11.8725	-1.2	3.5	-0.7366 ± -0.4909	-1.308 ± -0.872
2.3%	25.0168 ± 0.1019	0.0374 ± 0.0029	85.058 ± 0.654	15.7314	-0.5	5.6	-0.1150 ± -0.1850	-0.204 ± -0.328
2.6%	10.2593 ± 0.0224	0.0305 ± 0.0006	34.237 ± 0.137	19.2929	1.4	8.6	0.1446 ± 0.0375	0.257 ± 0.067
2.9%	5.8343 ± 0.0192	0.0299 ± 0.0005	19.530 ± 0.135	19.7030	1.1	10.6	0.0654 ± 0.0392	0.116 ± 0.070
3.2%	3.2398 ± 0.0104	0.0342 ± 0.0005	10.777 ± 0.119	17.1975	1.8	10.5	0.0579 ± 0.0347	0.103 ± 0.062
3.6%	2.1889 ± 0.0064	0.0456 ± 0.0007	7.345 ± 0.068	12.9123	1.0	11.8	0.0221 ± 0.0199	0.039 ± 0.035
4.0%	2.0415 ± 0.0065	0.0674 ± 0.0007	6.851 ± 0.057	8.7252	1.1	13.3	0.0222 ± 0.0166	0.039 ± 0.029
4.4%	1.7990 ± 0.0035	0.0642 ± 0.0005	5.926 ± 0.047	9.1681	2.9	16.6	0.0529 ± 0.0141	0.094 ± 0.025
4.4%	1.3378 ± 0.0033	0.0833 ± 0.0008	4.407 ± 0.046	7.0589	3.1	18.2	0.0420 ± 0.0136	0.075 ± 0.024
	Plateau age *(Plateau: 5th to 10th step)* **:**		***0.071 ± 0.013***					
	Total gas age **:**		***-0.084 ± 0.050***					
	Normal isochron age *(of plateau steps)* **:**		***0.057 ± 0.033***		*Initial $^{40}Ar/^{36}Ar$:*		*296.6 ± 2.6*	MSWD: 0.91
	Inverse isochron age *(of plateau steps)* **:**		***0.058 ± 0.023***		*Initial $^{40}Ar/^{36}Ar$:*		*296.6 ± 2.6*	MSWD: 0.91

Laser Output*	$^{40}Ar/^{39}Ar$	$^{37}Ar/^{39}Ar$	$^{36}Ar/^{39}Ar$ (x10^{-3})	K/Ca	$^{40}Ar^*$ (%)	$^{39}Ar_k$ (%)	$^{40}Ar^*/^{39}Ar_k$	Age(±1s) (Ma)
Sample ID: PK-28 (Upper Basalts)								
J= 0.000975		*Laboratory ID: C14083*		*Neutron Irradiation ID: PO-2*				
1.6%	183.325 ± 0.8179	0.3562 ± 0.0119	614.616 ± 4.262	1.6510	0.9	7.8	1.7344 ± 1.1750	3.048 ± 2.063
1.8%	147.782 ± 0.5076	0.5988 ± 0.0063	499.603 ± 1.730	0.9819	0.1	6.8	0.1963 ± 0.4439	0.345 ± 0.781
2.0%	101.231 ± 0.4678	0.9167 ± 0.0108	339.788 ± 2.256	0.6413	0.9	7.8	0.8962 ± 0.5652	1.576 ± 0.993
2.2%	74.3173 ± 0.3607	1.1397 ± 0.0109	251.105 ± 1.541	0.5157	0.3	7.6	0.2050 ± 0.3430	0.361 ± 0.603
2.4%	59.7054 ± 0.1793	1.1147 ± 0.0105	203.628 ± 0.857	0.5273	-0.6	8.0	-0.3800 ± -0.2400	-0.668 ± -0.422
2.5%	57.2787 ± 0.1088	1.1986 ± 0.0037	193.632 ± 0.802	0.4904	0.3	7.3	0.1542 ± 0.2259	0.271 ± 0.397
2.6%	50.8157 ± 0.1014	1.2422 ± 0.0026	174.394 ± 0.401	0.4731	-1.2	6.9	-0.6214 ± -0.1053	-1.093 ± -0.185
2.7%	44.3560 ± 0.0948	1.3109 ± 0.0058	150.367 ± 0.640	0.4483	0.1	7.2	0.0251 ± 0.1779	0.044 ± 0.313
2.8%	49.7673 ± 0.2409	1.3500 ± 0.0094	169.156 ± 0.937	0.4353	-0.2	5.0	-0.1128 ± -0.1556	-0.198 ± -0.274
2.9%	41.4804 ± 0.0743	1.3794 ± 0.0047	140.975 ± 0.367	0.4260	-0.2	6.2	-0.0700 ± -0.0984	-0.123 ± -0.173
3.0%	53.0179 ± 0.1302	1.4213 ± 0.0066	180.750 ± 1.194	0.4134	-0.5	3.5	-0.2829 ± -0.3325	-0.498 ± -0.585
3.2%	38.6566 ± 0.0837	1.6113 ± 0.0060	131.640 ± 0.475	0.3647	-0.3	5.7	-0.1173 ± -0.1235	-0.206 ± -0.217
3.5%	31.9388 ± 0.0442	2.0944 ± 0.0067	107.380 ± 0.368	0.2805	1.2	7.4	0.3721 ± 0.1028	0.654 ± 0.181
3.8%	22.8182 ± 0.0382	2.8589 ± 0.0092	78.730 ± 0.191	0.2054	-1.0	12.7	-0.2238 ± -0.0461	-0.394 ± -0.081
	Plateau age *(Plateau: **no plateau**)* **:**		±					
	Total gas age **:**		***0.258 ± 0.202***					
	Normal isochron age *(of all steps)* **:**		***-0.387 ± 0.137***		*Initial $^{40}Ar/^{36}Ar$:*		*296.1 ± 0.6*	MSWD: 2.22
	Inverse isochron age *(of all steps)* **:**		***-0.386 ± 0.047***		*Initial $^{40}Ar/^{36}Ar$:*		*296.1 ± 0.6*	MSWD: 2.23

Attachment 10: $^{40}Ar/^{39}Ar$ analytical results of Paka volcanics

Laser Output*	$^{40}Ar/^{39}Ar$	$^{37}Ar/^{39}Ar$	$^{36}Ar/^{39}Ar$ (x10^{-3})	K/Ca	$^{40}Ar^*$ (%)	$^{39}Ar_k$ (%)	$^{40}Ar^*/^{39}Ar_k$	Age(±1s) (Ma)
Sample ID: PK-29 (Upper Trachytes)								
J= *0.000976*		*Laboratory ID: C14084*			*Neutron Irradiation ID: PO-2*			
1.6%	274.238 ± 1.7166	0.0938 ± 0.0039	947.192 ± 5.796	6.2683	-2.1	1.0	-5.6503 ± -0.4600	-9.977 ± -0.815
2.0%	14.6981 ± 0.0298	0.0300 ± 0.0006	49.616 ± 0.144	19.5843	0.3	5.9	0.0388 ± 0.0422	0.068 ± 0.074
2.3%	2.9160 ± 0.0050	0.0247 ± 0.0003	9.629 ± 0.068	23.8553	2.5	10.5	0.0726 ± 0.0201	0.128 ± 0.035
2.6%	1.3328 ± 0.0029	0.0225 ± 0.0002	4.325 ± 0.036	26.1197	4.3	17.1	0.0566 ± 0.0109	0.100 ± 0.019
2.9%	0.7745 ± 0.0026	0.0211 ± 0.0001	2.650 ± 0.020	27.8630	-0.9	17.8	-0.0068 ± -0.0062	-0.012 ± -0.011
3.2%	0.6553 ± 0.0027	0.0207 ± 0.0003	2.153 ± 0.040	28.4535	3.1	14.0	0.0206 ± 0.0121	0.036 ± 0.021
3.6%	0.7555 ± 0.0025	0.0337 ± 0.0004	2.443 ± 0.013	17.4301	4.8	11.7	0.0363 ± 0.0044	0.064 ± 0.008
4.1%	1.0236 ± 0.0026	0.0682 ± 0.0006	3.390 ± 0.033	8.6187	2.6	11.1	0.0271 ± 0.0098	0.048 ± 0.017
4.8%	1.4765 ± 0.0028	0.1855 ± 0.0016	4.874 ± 0.040	3.1712	3.4	6.6	0.0507 ± 0.0120	0.089 ± 0.021
5.6%	2.0547 ± 0.0046	0.4261 ± 0.0025	6.746 ± 0.130	1.3801	4.6	4.3	0.0945 ± 0.0384	0.166 ± 0.068
	Plateau age *(Plateau: 5th to 8th step)* **:**		***0.039 ± 0.006***					
	Total gas age **:**		***-0.035 ± 0.012***					
	Normal isochron age *(of plateau steps)* **:**		***0.046 ± 0.048***		*Initial $^{40}Ar/^{36}Ar$:*		*293.5 ± 10.6*	MSWD: 4.09
	Inverse isochron age *(of plateau steps)* **:**		***0.050 ± 0.008***		*Initial $^{40}Ar/^{36}Ar$:*		*293.1 ± 10.6*	MSWD: 4.02

Laser Output*	$^{40}Ar/^{39}Ar$	$^{37}Ar/^{39}Ar$	$^{36}Ar/^{39}Ar$ (x10^{-3})	K/Ca	$^{40}Ar^*$ (%)	$^{39}Ar_k$ (%)	$^{40}Ar^*/^{39}Ar_k$	Age(±1s) (Ma)
Sample ID: PK-30 (Upper Trachytes)								
J= *0.000974*		*Laboratory ID: C14085*			*Neutron Irradiation ID: PO-2*			
1.6%	125.934 ± 0.3802	0.1611 ± 0.0041	428.551 ± 2.009	3.6508	-0.5	1.6	-0.6901 ± -0.5275	-1.213 ± -0.928
2.0%	29.1484 ± 0.0787	0.1059 ± 0.0013	99.564 ± 0.477	5.5532	-0.9	5.1	-0.2646 ± -0.1361	-0.465 ± -0.239
2.3%	10.393 ± 0.0142	0.0955 ± 0.0006	35.439 ± 0.071	6.1613	-0.7	10.4	-0.0718 ± -0.0188	-0.126 ± -0.033
2.6%	6.13918 ± 0.0110	0.0813 ± 0.0007	20.535 ± 0.066	7.2352	1.3	11.5	0.0775 ± 0.0190	0.136 ± 0.033
2.9%	4.10233 ± 0.0059	0.0775 ± 0.0004	13.691 ± 0.069	7.5895	1.5	14.4	0.0628 ± 0.0204	0.110 ± 0.036
3.2%	3.0149 ± 0.0028	0.0741 ± 0.0006	10.018 ± 0.034	7.9389	2.0	15.5	0.0602 ± 0.0101	0.106 ± 0.018
3.6%	2.3749 ± 0.0029	0.0698 ± 0.0005	7.807 ± 0.029	8.4327	3.1	16.1	0.0733 ± 0.0088	0.129 ± 0.016
4.1%	2.1245 ± 0.0041	0.0740 ± 0.0006	6.883 ± 0.047	7.9489	4.5	14.8	0.0964 ± 0.0141	0.169 ± 0.025
4.8%	2.1098 ± 0.0046	0.0975 ± 0.0006	6.945 ± 0.047	6.0297	3.1	10.7	0.0653 ± 0.0139	0.115 ± 0.024
	Plateau age *(Plateau: 4th to 9th step)* **:**		***0.126 ± 0.009***					
	Total gas age **:**		***0.050 ± 0.021***					
	Normal isochron age *(of plateau steps)* **:**		***0.133 ± 0.025***		*Initial $^{40}Ar/^{36}Ar$:*		*295.0 ± 1.4*	MSWD: 1.09
	Inverse isochron age *(of plateau steps)* **:**		***0.134 ± 0.023***		*Initial $^{40}Ar/^{36}Ar$:*		*295.0 ± 1.4*	MSWD: 1.09

Attachment 10: $^{40}Ar/^{39}Ar$ analytical results of Paka volcanics

Laser Output*	$^{40}Ar/^{39}Ar$	$^{37}Ar/^{39}Ar$	$^{36}Ar/^{39}Ar$ ($x10^{-3}$)	K/Ca	$^{40}Ar^*$ (%)	$^{39}Ar_K$ (%)	$^{40}Ar^*/^{39}Ar_K$	Age(±1s) (Ma)
Sample ID: M1 (Upper Basalts)								
J=	*0.000967*	*Laboratory ID: C14086*		*Neutron Irradiation ID: PO-2*				
1.6%	71.9089 ± 0.3296	0.6103 ± 0.0085	241.498 ± 1.352	0.9634	0.8	4.4	0.5941 ± 0.2874	1.036 ± 0.501
2.0%	81.5883 ± 0.2496	2.0170 ± 0.0105	275.416 ± 1.159	0.2912	0.4	5.2	0.3607 ± 0.3144	0.629 ± 0.548
2.3%	40.1723 ± 0.0971	2.2735 ± 0.0118	135.445 ± 0.783	0.2583	0.8	7.1	0.3263 ± 0.2124	0.569 ± 0.370
2.6%	25.7444 ± 0.0716	2.1991 ± 0.0131	87.455 ± 0.684	0.2671	0.3	10.0	0.0733 ± 0.1897	0.128 ± 0.331
2.9%	21.8069 ± 0.0441	2.1038 ± 0.0078	73.648 ± 0.453	0.2792	1.0	10.5	0.2086 ± 0.1282	0.364 ± 0.224
3.2%	17.6333 ± 0.0200	2.0783 ± 0.0076	60.046 ± 0.312	0.2826	0.3	16.4	0.0521 ± 0.0909	0.091 ± 0.159
3.5%	21.2463 ± 0.0367	2.0102 ± 0.0117	71.929 ± 0.454	0.2922	0.7	11.4	0.1483 ± 0.1319	0.259 ± 0.230
3.9%	21.6305 ± 0.0446	2.1202 ± 0.0081	73.769 ± 0.482	0.2770	0.0	10.9	-0.0026 ± -0.1356	-0.005 ± -0.237
4.5%	18.3445 ± 0.0193	2.7239 ± 0.0059	61.879 ± 0.508	0.2155	1.5	15.2	0.2724 ± 0.1502	0.475 ± 0.262
5.0%	25.3897 ± 0.0556	3.1971 ± 0.0099	86.032 ± 0.491	0.1836	0.9	9.0	0.2173 ± 0.1371	0.379 ± 0.239
	Plateau age *(Plateau: 4th to 8th step) :*		***0.160 ± 0.097***					
	Total gas age :		***0.320 ± 0.090***					
	Normal isochron age *(of plateau steps) :*		***-0.145 ± 0.820***		*Initial $^{40}Ar/^{36}Ar$:*		*298.0 ± 6.8*	MSWD: 0.72
	Inverse isochron age *(of plateau steps) :*		***-0.149 ± 0.119***		*Initial $^{40}Ar/^{36}Ar$:*		*298.1 ± 6.8*	MSWD: 0.72

Laser Output*	$^{40}Ar/^{39}Ar$	$^{37}Ar/^{39}Ar$	$^{36}Ar/^{39}Ar$ ($x10^{-3}$)	K/Ca	$^{40}Ar^*$ (%)	$^{39}Ar_K$ (%)	$^{40}Ar^*/^{39}Ar_K$	Age(±1s) (Ma)
Sample ID: M2 (Upper Basalts)								
J=	*0.000962*	*Laboratory ID: C14087*		*Neutron Irradiation ID: PO-2*				
1.6%	72.5416 ± 0.3057	0.4707 ± 0.0031	242.270 ± 1.239	1.2493	1.4	2.2	0.9880 ± 0.3060	1.714 ± 0.531
2.0%	19.8636 ± 0.0521	0.3945 ± 0.0020	68.944 ± 0.289	1.4908	-2.4	7.5	-0.4787 ± -0.0809	-0.831 ± -0.141
2.3%	8.5357 ± 0.0292	0.4139 ± 0.0016	29.107 ± 0.123	1.4209	-0.4	18.4	-0.0331 ± -0.0362	-0.057 ± -0.063
2.6%	6.5853 ± 0.0145	0.4367 ± 0.0021	22.212 ± 0.107	1.3467	0.8	16.6	0.0559 ± 0.0315	0.097 ± 0.055
2.9%	4.7898 ± 0.0064	0.4468 ± 0.0017	15.796 ± 0.101	1.3162	3.3	18.8	0.1570 ± 0.0296	0.272 ± 0.051
3.2%	4.6137 ± 0.0063	0.4355 ± 0.0008	15.330 ± 0.122	1.3503	2.5	10.6	0.1177 ± 0.0361	0.204 ± 0.063
3.5%	4.2671 ± 0.0066	0.4324 ± 0.0018	14.209 ± 0.090	1.3601	2.4	8.8	0.1022 ± 0.0262	0.177 ± 0.045
3.9%	4.5620 ± 0.0060	0.7376 ± 0.0021	14.964 ± 0.108	0.7971	4.3	9.1	0.1978 ± 0.0320	0.343 ± 0.055
4.5%	3.9886 ± 0.0064	1.1902 ± 0.0027	13.312 ± 0.105	0.4938	3.7	7.8	0.1480 ± 0.0311	0.257 ± 0.054
	Plateau age *(Plateau: 5th to 9th step) :*		***0.247 ± 0.024***					
	Total gas age :		***0.121 ± 0.026***					
	Normal isochron age *(of plateau steps) :*		***-0.055 ± 0.380***		*Initial $^{40}Ar/^{36}Ar$:*		*307.4 ± 15.4*	MSWD: 1.35
	Inverse isochron age *(of plateau steps) :*		***-0.053 ± 0.023***		*Initial $^{40}Ar/^{36}Ar$:*		*307.4 ± 15.4*	MSWD: 1.35

Attachment 11: Age dating results superimposed on the geological map (Dunkley et al. 1993)

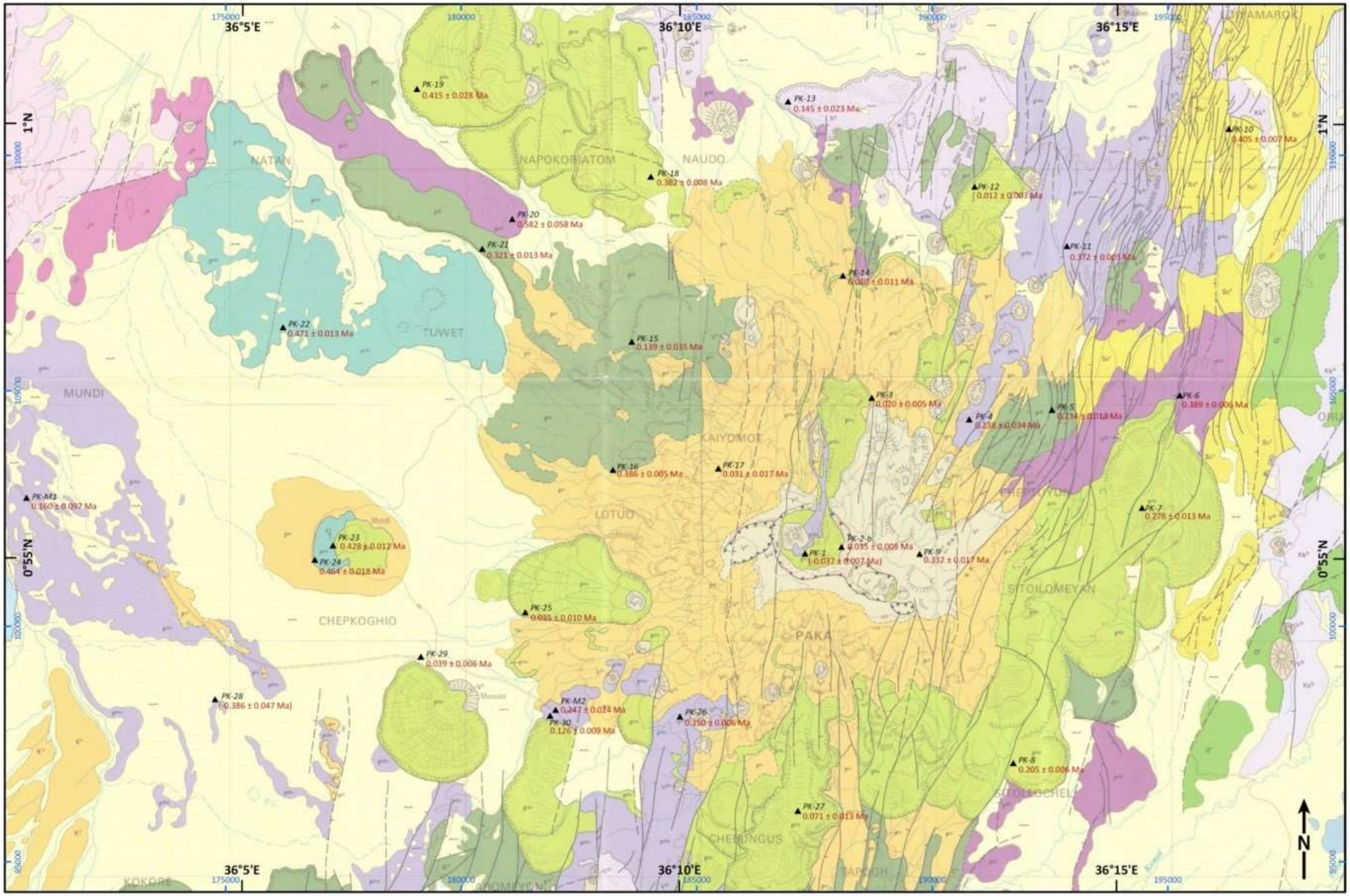

Attachment 12: Age dating results superimposed on the shaded relief map

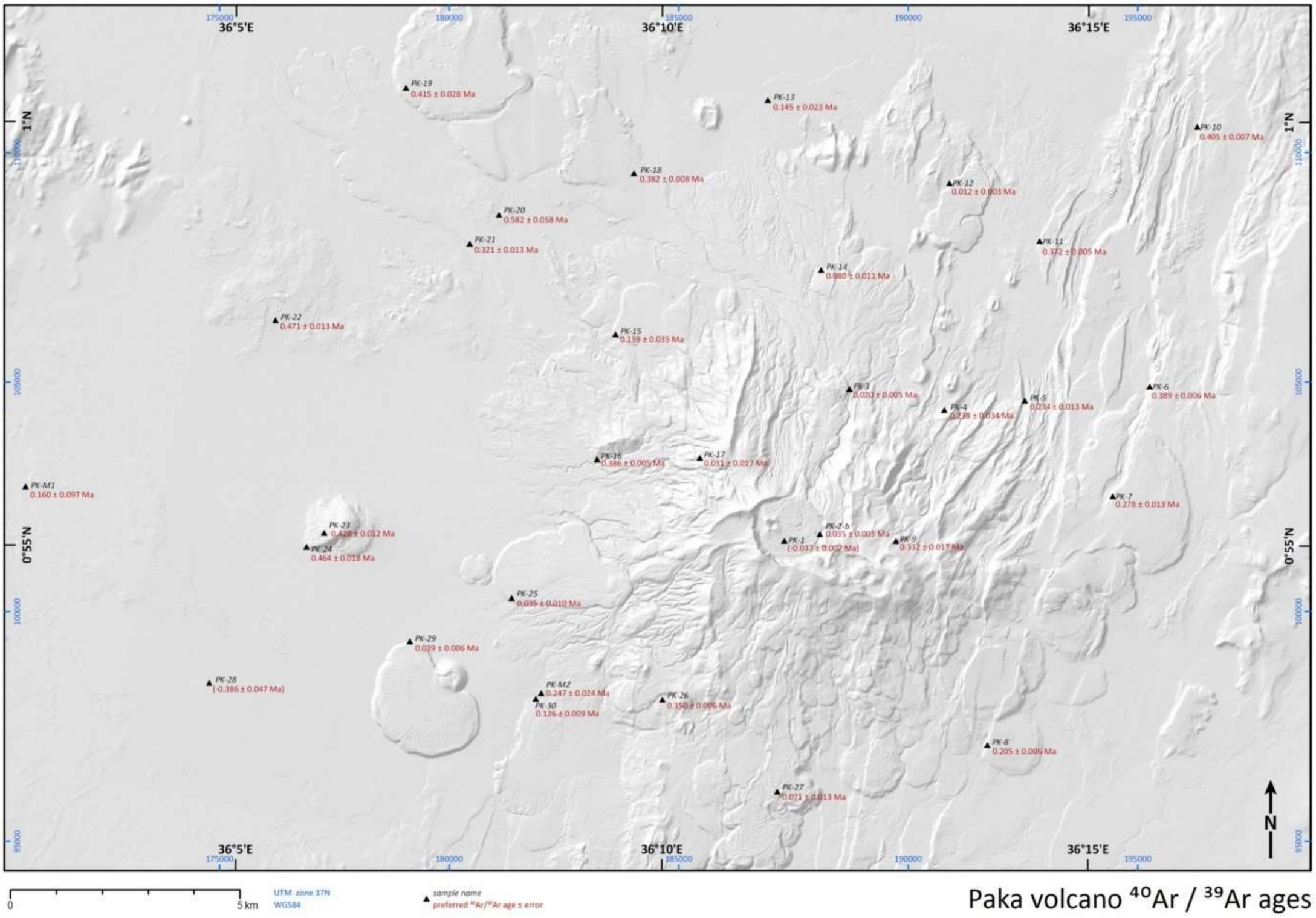

Paka volcano ^{40}Ar / ^{39}Ar ages